Spectral-Domain Phase-Sensitive Interferometry for Real-Time Probing of Electrodeposition Processes

by

YuJen Chiu

DISSERTATION

Submitted in Partial Fulfillment of the Materials Science and Engineering for the Degree of Doctor of Philosophy at The University of Texas at Arlington

August ,2018

Arlington, Texas

Supervising Committee:

Yaowu Hao, Supervising Professor

Ye Cao

Choong-Un Kim

Efstathios"Staths"I.Meletis

Digant Dave

Copyright by YuJen Chiu

2018

All Rights Reserved

Acknowledgments

The project was supported by many people. My sincere gratitude goes to my Professor, Dr. Yaowu Hao, who was really patient to guide and provide invaluable assistance.

Besides, the research could only be undertaken by the advanced facilities, expertise and continuous guidance provided by Dr. Digant Dave.

Special thanks to my group of members Chivarat Muangphat, Orathai Thumthan, Akshay Sunil Hande, Aseem Atul Athavale, Christopher Scott Pickering, and Shahab Ranjbarbahadori. We share laughs and wisdom opinions with each other, especially in the Laboratory. Also, thanks to my friends who encourage me.

In the end, my sincere thanks to my parents, who provided me with unconditional support and love and constantly encouraged me to fulfil my dream.

Aug 10, 2018

Abstract

SPECTRAL-DOMAIN PHASE-SENSITIVE INTERFEROMETRY FOR REAL-TIME PROBING ELECTRODEPOSITION PROCESSES

YuJen Chiu

The University of Texas at Arlington, 2018

Supervising Professor: Yaowu Hao

Electrodeposition is a simple, versatile and scalable method for depositing thin metal films on conductive substrates, and it has long been used in large-scale industrial processes for metal film coating. In the last two decades, electrodeposition has entered into the manufacturing processes of electronic devices. Electrodeposition of Cu has become the standard process for the backend processes for almost all microelectronic devices. Electrodeposition of Cu and magnetic materials are used in the fabrication of write/read head in computer hard disk drive. More recently, a unique electrodeposition process, underpotential deposition (UPD), has been utilized for atomic layer deposition to generate films layer by layer. Aiming to achieve better control of the microstructures of deposited films, investigating the mechanism of nucleation and growth of metallic phases in the electrodeposition process has drawn significant attention. Most of these studies have employed electrochemical transient measurements. However, due to the stochastic nature at the early stages of electrodeposition, the early stages of metal phase formation models

for electrodeposition obtained using current transient responses do not accurately reflect atomic behaviors on the surface of the substrate. More powerful nanoscale characterization tools, including In-situ transmission electron microscopy (TEM), scanning tunneling microscopy (STM), and atomic force microscopy (AFM) have been utilized for investigating the electrodeposition process. However, these in-situ methods usually require particular electrodeposition cells, and more problematically, they all inevitably interfere with the electrochemical process.

In this project, we have been developing a new optical method, Spectral Domain Phase Sensitive Interferometry (SDPSI), for in situ monitoring electrochemical processes. Unlike other in situ techniques, PSI does not require individual electrochemical cell. Therefore, it has the potential to be implemented in practical electrochemical processes. More importantly, PSI does not interfere with electrochemical processes since only near-infrared light (wavelength ~800 nm) interact with electrolyte and substrate. This interferometric detection method is based on the phase–sensitive detection of spectral interference fringes. In this technique, by measuring the phase on an interference signal, sub-nanometer changes in optical path length can be measured.

We used SDPSI to study the cyclic voltammetry (CV) of UPD of Cu on Au surface. UPD is the electrochemical deposition process of a sub-monolayer or monolayer of metal on different substrates using a potential more positive than the equilibrium potential. It occurs when the adsorbate adatoms are more strongly bound to the different substrate than to a substrate of their kind. We demonstrated that SDPSI could detect the monolayer film formation in real time, allowing us to “see” the atomic processes at the substrate surface during CV measurements. We proved that SDPSI could be used as a real-time monitor with a sub-monolayer resolution for electrodeposition.

Also, we used SDPSI to study the atomic processes in the pre-deposition and initial deposition stage of general electrodeposition processes. We found that SDPSI can detect accumulation on the substrate surface before the deposition takes place, and accurately predict the initial deposition potential. Also, it has been found that such initial deposition potential has a dependence on the substrate thickness for ultra-thin film working electrodes.

We clearly demonstrated that SDSPI is a reliable new tool for real-time probing electrodeposition processes. It can be used as a thickness monitor for electrodeposition, a long-awaited scientific breakthrough.

Contents

1.Introduction 1

2.Background information 4

2.1Electrodeposition 4

2.1.1 Introduction 4

2.1.2 ELECTROCHEMISTRY FUNDAMENTALS 8

2.1.3 Atomic Processes and Parameters in Electrodeposition..... 22

2.1.4 Applications of Electrodeposition 30

2.2 Cyclic voltammetry..... 37

2.3 Underpotential deposition..... 41

2.3.1 Introduction 41

2.3.2 Experimental Studies of UPD 42

2.3.3 Theoretical analysis of UPD shifts 45

2.3.4 Atomic Layer Electrodeposition 51

3. In-situ monitoring Cu monolayer formation using Phase-sensitive interferometry..... 53

3.1 Phase Sensitive Interferometry..... 53

3.1.1 Working principle of using PSI to measure the thickness..... 56

3.1.2 Working principle of Spectral Domain Low Coherence Interferometer (SD-LCI) 61

3.1.3 Spectral Domain-Phase Sensitive Interferometer 64

3.2 Copper Underpotential Deposition on Gold Electrodes 68

3.2.1 Sulfuric acid media 69

3.2.2 Influence of Anions 74

3.2.3 Cu UPD on different single-crystalline Au electrodes 79

3.2.4 Cu UPD on polycrystalline Au surface 82

3.3 Copper UPD Experiment processing 83

3.3.1 Equipment set up and experimental procedure 83

3.3. UPD CV on Different Substrates 2 84

3.3.3 Real-time Probing CV of Cu UPD 86

3.3.4 Optical properties of monolayer Cu UPD deposited on Au surface 92

4. Atomic processes in the pre-deposition and early deposition stage of general electrodeposition processes 94

4.1 Background information 94

4.1.1 Copper water chemistry 94

4.1.2 Nucleation modeling 95

4.2 Effect of Cu ion concentration on the early stage of electrodeposition 97

4.3 Effect of Applied Potential 101

5. Conclusions and Future study 107

Future study 107

Reference 110

Appendix 115

A.Raw data of phase result including fitting 115

B.Optical properties Cu and Au 117

Figure 1 Electrolytic cell for electrodeposition of metal, M, from an aqueous solution of metal salt, ... 5

Figure 2 Principle of electroplating 7

Figure 3 water molecules structure 9

Figure 4 orientation of water molecules with respect to positive and negative ions 10

Figure 5 Ion-water interaction 11

Figure 6 Two phases in contact: (a) at t=0, moment of contact; (b) at equilibrium 11

Figure 7 Formation of metal-solution interphase 13

Figure 8 The potential difference across the electrochemical cell, ... 14

Figure 9 Hydrogen electrode 16

Figure 10 Saturated calomel electrode 18

Figure 11 Silver-silver chloride electrode 19

Figure 12Reference electrodes 20

Figure 13 Process steps for forming Al interconnects using an RIE process 31

Figure 14 Process steps for forming Cu interconnects using a Damascene process 32

Figure 15 Computer hard disk drive write head 34

Figure 16 Thin-film write head fabrication process 35

Figure 17 Typical excitation signal for cyclic voltammetry- a triangular waveform with switching potential at 0.8 and -0.2 V versus SCE.[33] 39

Figure 18 Thermochemical Cycle is denoting different energetic contributions participating in the monolayer formation of a metal on a different substrate [41] 47

Figure 19 Schematic representation of processes constituting adsorption of M upon S. IHP and OHP indicates respectively, the inner and outer Helmholtz plane. The metal ions, Mn+ are surrounded by the solvent molecules 'w'.[41] 49

Figure 20 Calculated SI data for a single reflective surface. (a) Input light source spectrum. (b) Output spectral interferogram.(c) Spectral interferogram with the input spectrum removed. (d)Fourier transform of the spectral interferogram.[62] 58

Figure 21 the fringe pattern of sample and sample +1nm 60

Figure 22 the subtraction fringe pattern of sample and sample +1nm 60

Figure 23 Low coherence two-path interferometric setup. Light from the source is split in two using beamsplitter (BS) which after reflecting back from reference and sample path are recombined to produce interference fringes detected by the spectrometer. 62

Figure 24 Low coherence single-path interferometric configuration (common mode interferometry). Light from the source is transmitted through a beamsplitter (BS), which gets reflected back from top and bottom surface of the sample and are recombined to produce interference fringes detached by the spectrometer. 63

Figure 25 Optical setup of the spectral domain phase sensitive interferometer. 90:10 coupler splits combined power of 800 nm and 635 nm Laser in 90:10 ratio. 90% is input to a 50:50 coupler which after reflecting back from the sensor surface is detected by the spectrometer. Computer stores acquired interference spectrums 65

Figure 26 Setup of a fiber-based spectral domain phase sensitive interferometer 66

Figure 27 Photograph of the SD-PSI sample path configuration showing various components integrated together using a cage system. 67

Figure 28 The optical configuration of the formation of Copper Monolayer 68

Figure 29 Cyclic voltammogram for a Au(111) electrode in 0.05 M H_2SO_4 + 1 mM $CuSO_4$. Scan rate: 1 mV/s. Copyright 1991 Elsevier Sequoia SA.[38] 70

Figure 30 X-ray absorption spectra around the Cu KR edge for CU UPD on Au (111) at +0.13 V vs. Ag/AgCl. Copyright 1988 American Chemical Society.[38] 71

Figure 31 STM image of the structure for Cu UPD on Au(111) at +0.15 V vs. SCE showing two different phase boundaries. Copyright 1991 Elsevier Sequoia SA.[38] 73

Figure 32 Interfacial structure of the Cu UPD on Au(111) after the first UPD peak: (a) top view; (b) side view. Copyright 1995 The American Physical Society.[38] 74

Figure 33 Voltammetric profiles of Cu UPD on Au(111): (a) 0.05 M H_2SO_4 + 1 mM $CuSO_4$ + 0.1 mM KCl; (b) 0.05 MH_2SO_4 + 1 mM $CuSO_4$ + 0.1 mM KBr; (c) 0.05 M H_2SO_4 + 1 mM $CuSO_4$ + 0.1 mM KI. The broken curve on (a) is for 0.05 M H_2SO_4 + 1 mM $CuSO_4$, given for comparison. Scan rate: 5 mV/s. © 1994 Elsevier Science SA.[38] 75

Figure 34 Series of three STM images of Cu UPD on Au (111) in 0.1 M $HClO_4$ + 0.01 M Cu $(ClO_4)_2$ solution containing trace amounts of Cl^- ions recorded over the same area at time intervals of 25 s. Upon a change of the potential from +0.3 to +0.13 V vs. SCE at the beginning of image (a) the transformation of the one structure into the other structure via an island growth of the phase is

observed. Copyright 1995 Elsevier Science BV.[38] 77

Figure 35 Model for the bilayer structure formed by the copper and chloride ions at the Au (111) surface: (A) copper adsorbed in registry with the Au (111) substrate; (B) copper adsorbed in registry with the top layer of chloride ions. Reproduced. Copyright 1995 Elsevier Science Ltd.[38] 77

Figure 36 Cyclic voltammogram for a Au (100) electrode in 0.01 M H_2SO_4 + 1 mM $CuSO_4$ without (dashed line) and with the addition of 0.1 mM HCl. Scan rate: 2 mV/s. Copyright 1995 The American Physical Society.[38] 78

Figure 37 Underpotential CV in the presence (a) and absence (b) of Cu^{2+} (1mM) in H_2SO_4 (0.1 M) at bare gold. Sweep rate: 100mV/s.[63] 82

Figure 38 Setup for electrochemical study for interferometry 84

Figure 39 Different Substrate for Copper UPD process. 86

Figure 40 Experimental cyclic voltammetry current densities for a gold-coated electrode in 1mM CuSO4 + 0.1mM H2SO4 at 1, 2 , 5, and 10 mV/s, respectively 87

Figure 41 Underpotential CV in the Cu^{2+}(1mM) in H_2SO_4 (0.1M) at bare gold electrodes. Sweep rate:5mVs^{-1} and 2mVs^{-1} 89

Figure 42 Different unit in the Cu2+(1mM) in H2SO4 (0.1M) at bare gold electrodes. Sweep rate:5mVs-1 and 2mVs^{-1} 90

Figure 43 the optical configuration of the formation of Cu monolayer. 91

Figure 44 Phase result corresponding Current at CV proceeding experiment. 91

Figure 45 Equilibrium diagrams for CuSO4/water system: (a) $E_{Cu/Cu2+}$/ pH diagram, (b) distribution pH diagram. Conditions: 0.01 M Cu^{2+},0.01M S^{6+}, room temperature.[64] 95

Figure 46 Current density versus time as copper concentration increasing. 99

Figure 47 Phase and scattering result for 1M $CuSO_4$ deposition on the Au surface. 99

Figure 48 Phase and scattering result for 0.1M $CuSO_4$ deposition. 100

Figure 49 Phase and scattering result for 0.05M $CuSO_4$ deposition. 100

Figure 50 Phase and scattering result for 0.01M $CuSO_4$ deposition. 101

Figure 51 potential varied from +0.1V to minus -0.1V at 100mM $CuSO_4$. 101

Figure 52 Current density and potential versus time from +0.1V to minus -0.1V at 100mM $CuSO_4$. 102

Figure 53 Phase result corresponding Current and potential versus time for potential applied -0.1V.. 103

Figure 54 Phase result corresponding Current and potential versus time for potential applied 0V. 104

Figure 55 Phase result corresponding Current and potential versus time for potential applied -0.1V.. 104

Figure 56. Phase result corresponding Current and potential versus time for potential applied -0.2V.. 104

Figure 57 SEM and EDX image for 0.1V pulse experiment at 100mM CuSO4. 105

Figure 58 SEM and EDX image for 0V pulse experiment at 100mM CuSO4 105

Figure 59 SEM and EDX image for-0.1V pulse experiment at 100mM $CuSO_4$. 106

Figure 60 SEM and EDX image for -0.2V pulse experiment at 100mM $CuSO_4$. 106

Figure 61 One step at a time. Electrochemical atomic layer deposition of ultrathin Pt films deposited one monolayer at a time by merely pulsing the electrode potential between +0.4 and –0.8 V. A capping layer of hydrogen is produced at –0.8 V that blocks the deposition of more than one monolayer of Pt. When the potential is stepped to +0.4 V, the hydrogen layer is desorbed, and the cycle can begin again. The self-limiting processing method is fast because it is performed in a single plating bath, so it is not necessary to exchange reactants. The ultrathin Pt films could lower the costs of the Pt catalyst in fuel cells and provide a platform to study how the catalytic, electronic, and magnetic properties of ultrathin films evolve with film thickness.[6] 108

Figure 62 New cell set up for the top light source. 109

Figure 63 Optical result for Copper UPD CV experiment proceeding at the 2mvs^{-1}and Fitting figure. 115

Figure 64 Optical result for Copper UPD CV experiment proceeding at 2mvs^{-1} and Fitting figure. 116

Figure 65 Optical result for Copper UPD CV experiment proceeding at 5mvs^{-1} and Fitting figure. 116

Figure 66 Optical result for Copper UPD CV experiment proceeding at 5mvs^{-1} and Fitting figure. 117

Figure 67 Example of the intersection in the n-k plane of normal-incidence R and T contours with the p-polarized T contour for 60' incident angle. The width of the contours, which represents the estimated experimental error, is exaggerated by a factor of 5 for the normal incidence contours.[64] 121

Figure 68 Dielectric constants for copper as a function of photon energy. The width of the curves is representative of the instrumenta1 error.[64] 123

Figure 69 Dielectric constants for gold as a function of photon energy. The width of the curves is representative of the instrumental error.[64] 124

Figure 70 Negative of the real part of the dielectric constants for copper, silver, and gold vs. the square of the wavelength. The zeros in $-\epsilon_1$ *for silver and gold are offset by 25 and 50„respectively.[64]* 128

Figure 71 Imaginary part of the dielectric constants for copper, silver, and gold, divided by wavelength vs. the square of the wavelength.[64] 129

1.Introduction

Electrodeposition offers the most versatile and scalable means for metal film growth. It is a bottom-up processing method, where a solid is assembled from ionic or molecular precursors in solution, and solution additives and pH can be used to control the growth. Hence, the size, shape, crystallographic orientation, and even chirality of deposited films can be tuned. Compared with physical vapor deposition (CVD/PVD) in a vacuum chamber, electrodeposition is inexpensive, and can have much higher deposition rates. In addition, unlike most PVD processes, electrodeposition is not a line-of-sight process, so conformal films can be grown on complex shapes. [1-7]

Electrodeposition has long been used in large-scale industrial processes for metal film coating. About two decades ago, electrodeposition of Cu became a unique process for manufacturing most microelectronic devices. In recent years, mostly due to the successful utilization of the electrodeposition process for atomic layer deposition, electrodeposition process has again become an active research field. The electrochemical scientific international community has devoted attention on few fundamental aspects of electrodeposition of metals, including the mechanism and kinetics linked to the initial stages formation of the first metallic nuclei. The aim of these studies was investigating the significant occurrence of surface phenomena, for instance, ordered adsorption, nucleation and growth, short-range phase transformations, cluster formation, and so on. [8, 9]

The study of the mechanism of nucleation and growth of metallic phases in electrodeposition

process has mostly employed electrochemical transient measurements, with which various models have been developed linking the time-dependent current to microscopic physical parameters such as nucleation rate and nuclei density. However, the early stages of electrodeposition are of stochastic nature coupled with fast mass transport phenomena and highly dynamic topographic change. [10-17]These make it notoriously difficult to probe into discrete events at this stage in real-time. The accuracy of classical nucleation models for electrodeposition obtained using current transient responses, particularly in the early stages of metal phase formation, has been challenged as more powerful nanoscale characterization tools, including In-situ transmission electron microscopy (TEM), scanning tunneling microscopy (STM), and atomic force microscopy (AFM) have been utilized for investigating the electrodeposition process. These tools provide direct images of the formed morphologies and structures of deposited metal atoms. However, these in-situ methods usually require special electrodeposition cells, and more problematically, they all inevitably interfere with the electrochemical process. [2, 18-32]

In this project, we have been developing a new optical method, Spectral Domain Phase Sensitive Interferometry (SDPSI), for in situ monitoring electrochemical processes. Unlike other in situ techniques, PSI does not require special electrochemical cell. It has the potential to be implemented in practical electrochemical processes. More importantly, PSI does not interfere with electrochemical processes, since only near-infrared light (wavelength ~800nm) interact with electrolyte and substrate.

This interferometric detection method is based on the phase–sensitive detection of spectral interference fringes. In this technique, by measuring the phase on an interference signal, sub-

wavelength changes in optical path length (OPL) can be measured. In any interferometric setup phase information is readily available, but environmental noise usually wholly corrupts such phase information rendering it useless for any measurements. The setup we used utilizes a simple spectral interferometric technique, common path interferometry, to cancel common mode noise. Using this setup, measuring OPL changes in the picometer range has been achieved.

2.Background information

2.1Electrodeposition

2.1.1 Introduction

Electrochemical deposition of metals and alloys involves the reduction of metal ions from aqueous, organic, and fused-salt electrolytes. Here, we treat deposition from aqueous solutions only.

The reduction of metal ions M^{z+} in aqueous solution is represented by

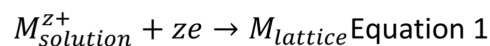

$$M_{solution}^{z+} + ze \rightarrow M_{lattice} \quad \text{Equation 1}$$

This can be accomplished by means of two different processes: (1) an electrodeposition process in which *z* electrons are provided by an external power supply, and (2) an electroless (autocatalytic) deposition process in which a reducing agent in the solution is the electron source (no external power supply is involved). These two processes, electrodeposition, and electroless deposition constitute the electrochemical deposition.

In either case, our interest is in a metal electrode in contact with an aqueous ionic solution. Deposition reaction presented by is a reaction of charged particles at the interface between a solid metal electrode and a liquid solution. The two types of charged particles, a metal ion, and

an electron, can cross the interface.

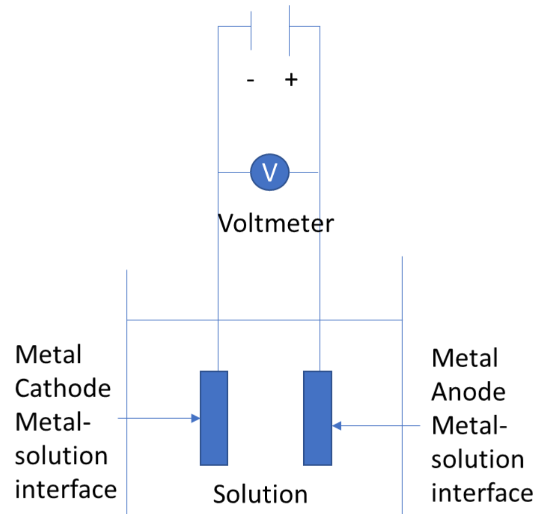

Figure 1 Electrolytic cell for electrodeposition of metal, M, from an aqueous solution of metal salt,

In practice, the core part of the electroplating process is the electrolytic cell (electroplating unit). In the electrolytic cell (electroplating unit) current is passed through a bath containing an electrolyte, the anode, and the cathode. In industrial production, pretreatment and post-treatment steps are usually needed as well.

The workpiece to be plated is the cathode (negative terminal). The anode, however, can be one of the two types: sacrificial anode (dissolvable anode) and permanent anode (inert anode).The sacrificial anodes are made of the metal that is to be deposited. The permanent anodes can only complete the electrical circuit, but cannot provide a source of new metal to replace what has been removed from the solution by deposition at the cathode. Platinum and carbon are usually

used as inert anodes. The workpiece to be plated is the cathode (negative terminal).

The anode, however, can be one of the two types: sacrificial anode (dissolvable anode) and permanent anode (inert anode.) The electrolyte is the electrical conductor in which current is carried by ions rather than by free electrons (as in the metal).

Electrolyte completes an electric circuit between two electrodes. Upon application of electric current, the positive ions in the electrolyte will move toward the cathode and the negatively charged ions toward the anode. This migration of ions through the electrolyte constitutes the electric current in that part of the circuit. The migration of electrons into the anode through the wiring and a power generator and then back to the cathode constitutes the current in the external circuit. The metallic ions of the salt in the electrolyte carry a positive charge and are thus attracted to the cathode. When they reach the negatively charged workpiece, it provides electrons to reduce those positively charged ions to metallic form, and then the metal atoms will be deposited onto the surface of the negatively charged workpiece.

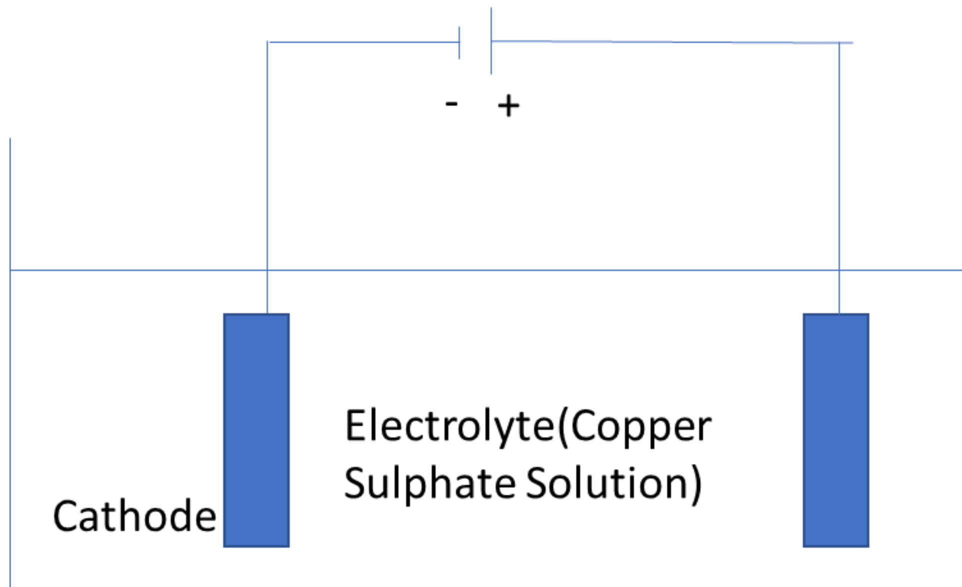

Figure 2 Principle of electroplating

Figure 2 illustrates a typical plating unit for plating copper from a solution of the metal salt copper sulfate ($CuSO_4$). The cathode, which is the workpiece to be plated, is charged negatively. Some of the electrons from the cathode bar transfer to the positively charged copper ions (Cu^{2+}), setting them free as atoms of copper metal. These copper atoms take their place on the cathode surface, and copper plates it. Concurrently, the same number of sulfate ions SO_4^{2-} is discharged on the copper anodes, thereby completing the electrical circuit. In so doing, they form a new quantity of copper sulfate that dissolves in the solution and restores it to its original composition. This procedure is typical of conventional electroplating processes with sacrificial anodes; the current deposits a given amount of metal on the cathode and the anode dissolves to the same extent (of the same electrical charge), maintaining the solution more or less uniformly.

2.1.2 ELECTROCHEMISTRY FUNDAMENTALS

Understanding the electrochemical principles of electrodeposition is essential to the development of electroplating technologies. Some basic concepts are presented below.

2.1.2.1 Ion-water interaction

It can be seen that the essential components of an electrodeposition cell are two metal electrodes (M_1 and M_2), water containing dissolved ions, and two metal-solution interfaces: M_1-solution and M_2-solution.

Successful use of electrodeposition in the production of electrodeposits of desired properties depends on understanding each component.

Oxygen and hydrogen atoms in H_20 are held together by a covalent bond. The nuclei of oxygen and two hydrogens in the water molecule form an isosceles triangle. The O-H bond length is 0.95718 A, and the H-O-H angle is 104.523º.

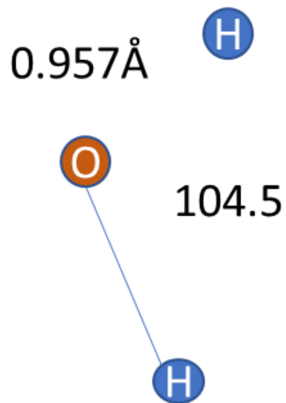

Figure 3 water molecules structure

In water molecules, the O-H bond, the oxygen atom has a higher affinity for electrons, and the result is a separation of charge in the bond. The bonding electron pair spends more time near the oxygen than near the hydrogen. Thus, the O-H bond is polarized; that is, the hydrogen carries a small partial positive charge, δ^{+}, and oxygen carries a small partial negative charge, δ^{-}. This gives rise to a bond dipole moment.

One method to form ions in aqueous solution is introducing ions into solutions by the dissolution of an ionic crystal. Ionic crystals are composed of separate positive and negative ions. The overall dissolution process of an ionic crystal MA can be represented by the reaction:

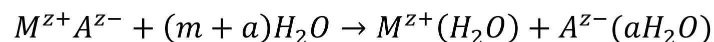

$$M^{z+}A^{z-} + (m + a)H_2O \rightarrow M^{z+}(H_2O) + A^{z-}(aH_2O)$$

The ion-water interaction: ion-dipole forces are the principal forces in the ion-water interaction. The result of these forces is the orientation of water molecules in the immediate vicinity of an

ion. One end of the water dipole is attached electrostatically to the oppositely charged ion.

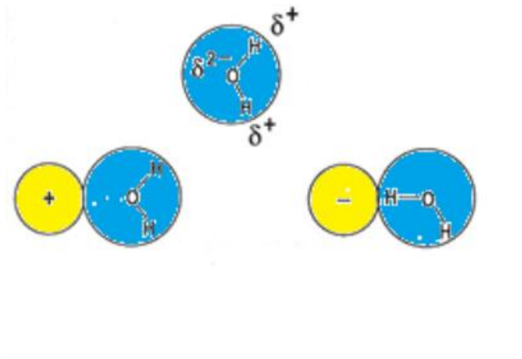

Figure 4 orientation of water molecules with respect to positive and negative ions

The result of this orienting force is that a certain number of water molecules in the immediate vicinity of the ion are preferentially oriented, forming a primary hydration shell of oriented water molecules. These water molecules do not move independently in the solution. Instead, the ion and its primary water sheath form a single entity whose parts move together in the thermal motion and under the influence of an applied electric field. Next to the first water of hydration is the shell of secondary water of hydration. In this region, water molecules are under the influence of the orienting forces of the ion and the hydrogen-bond forces of bulk water molecules. Thus, water molecules in the shell of secondary water of hydration are partially oriented (Figure 5 ion-water interaction). Beyond the secondary water of hydration is the bulk water.

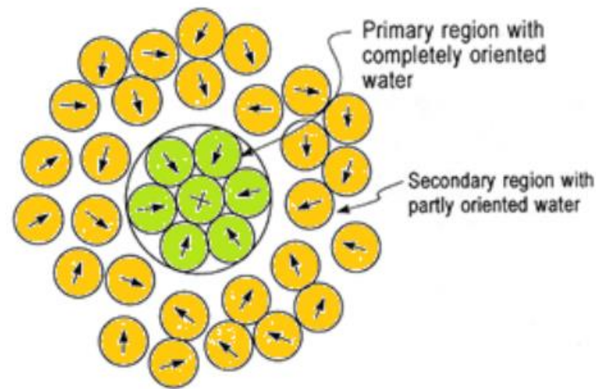

Figure 5 Ion-water interaction

2.1.2.2 Metal-solution interphase

The metal-solution interface is the locus of the electrodeposition process and thus the most critical component of an electrodeposition cell.

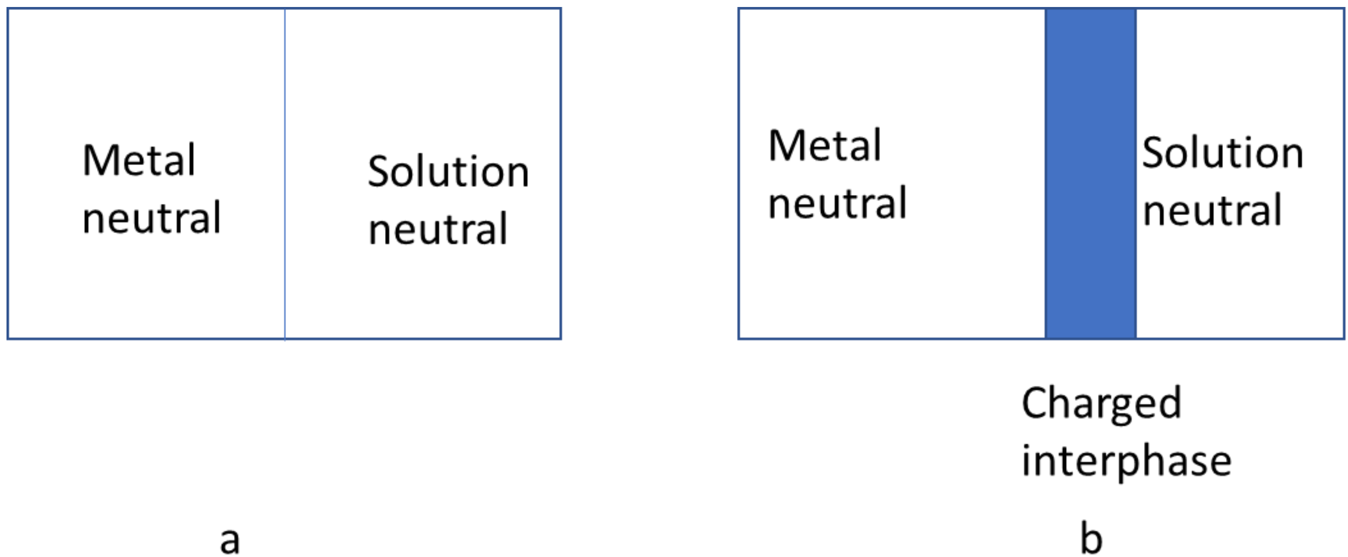

Figure 6 Two phases in contact: (a) at t=0, moment of contact; (b) at equilibrium

Let us consider a case where a metal *M* is immersed in the aqueous solution of its salt, *MA*. Bother phases, metal and the ionic solution, contain M^+ ions. At the metal-solution interface, there will be an exchange of metal ions M^+ between the two phases, some M^+ ions from the crystal lattice enter the solution, and some ions from the solution enter the crystal lattice. For some materials, conditions are such that more M^+ ions leave than enter the crystal lattice. And for some materials, conditions are just the opposite. In the former case, there is an excess of electrons on the metal and the metal acquires negative charge, which is represented as q_M^- (charge on the metal per unit area). Due to this negative charge of the metal side, positively charged M^+ ions from solution will be attracted in the vicinity of the metal interface. The interphase consists of two equal and opposite layers of charges, one on the metal (q_M^-) and the other in solution (q_S^+). This pair of charged layers, called the double layer, is equivalent to a parallel-plate capacitor. There is a potential (electric field) built in the double layer, and this electric field will be against the further movement of the ions and electrons. So equilibrium is established.

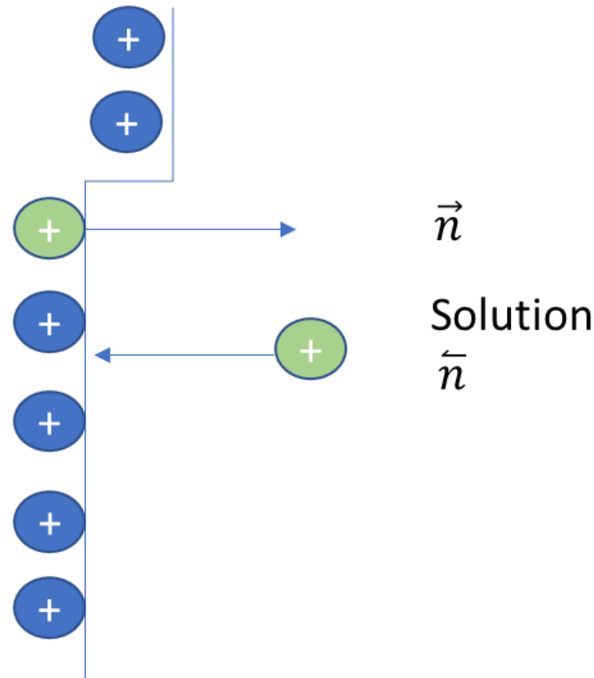

Figure 7 Formation of metal-solution interphase

2.1.2.3 Equilibrium electrode potential

Let us consider the general electrochemical cell as shown in Figure 8. We can measure the total potential difference across the electrochemical cell, denoted E, which is called the electromotive force (EMF) of the cell. The potential difference E here is made up of four contributions since there are four phase boundaries in this cell: two metal-solution interphases and two metal-metal interfaces. The cell can be represented schematically as Pt/M'/S/M/Pt. the total potential will be:

$$\mathrm{E} = \Delta\emptyset(\mathrm{Pt}, \mathrm{M}) + \Delta\emptyset(\mathrm{M}, \mathrm{S}) + \Delta\emptyset(\mathrm{S}, \mathrm{M}') + \Delta\emptyset(\mathrm{M}', \mathrm{Pt})$$

Since $\Delta\phi(S, M') = -\Delta\phi(M', S)$ and $\Delta\phi(M', Pt) = -\Delta\phi(Pt, M')$, the preceding equation can be written as the difference between two electrode potentials:

$$\mathrm{E} = \{\Delta\emptyset(Pt, M) + \Delta\emptyset(M, S)\} - \{\Delta\emptyset(M', S) + \Delta\emptyset(Pt, M')\}$$

Or

$$\mathrm{E} = E_r - E_l$$

Where the right-hand electrode potential is

$$E_r = \Delta\emptyset(Pt, M) + \Delta\emptyset(M, S)$$

And the left-hand electrode potential is

$$E_l = \Delta\emptyset(M', S) + \Delta\emptyset(Pt, M')$$

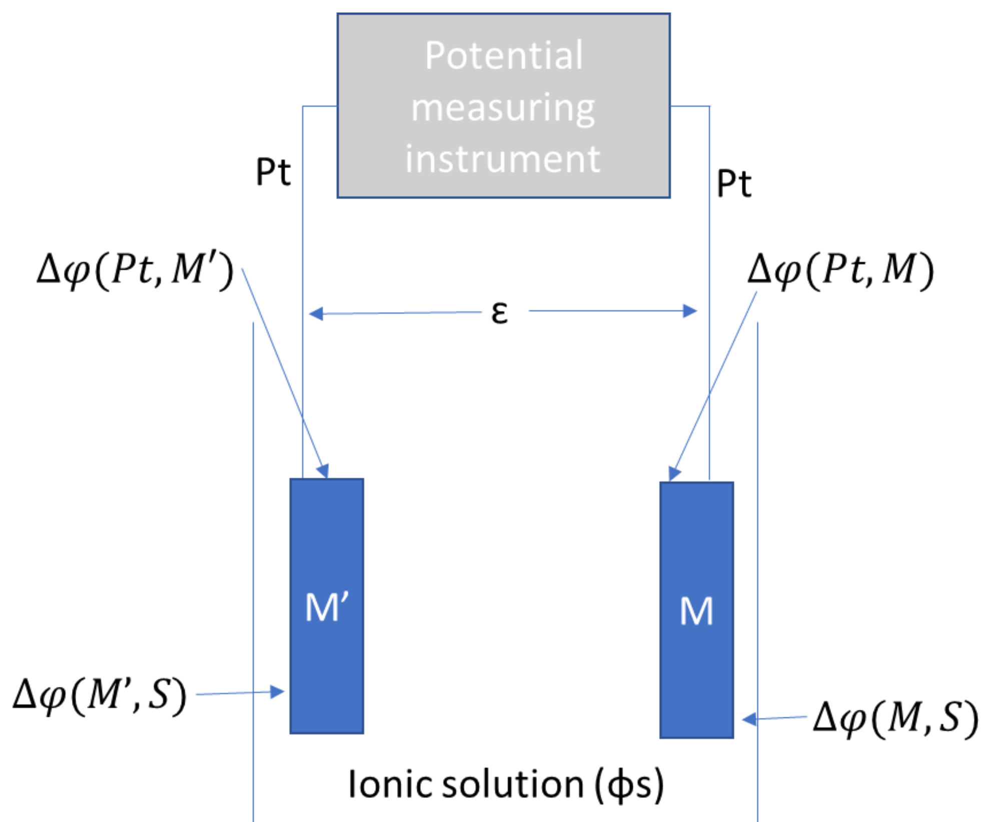

Figure 8 The potential difference across the electrochemical cell,

If E_l is taken as a reference electrode and set arbitrarily to $E_l=0$, then $E = E_r$. The term $\Delta\phi(Pt, M)$ appears in all measurements, which is the potential difference that appears when two dissimilar conductors come into contact.

Three issues have to be resolved to measure this equilibrium electrode potential: (1) the selection of a reference electrode; (2) the coupling of the reference electrode with the electrode whose potential is being measured, in this case, M/M^{z+}; and (3) the experimental method for the voltage measurement.

A reference electrode, connected to an electrode at equilibrium such as the M/M^{z+} electrode, make up an electrochemical cell with an individual cell voltage. If a voltage measuring instrument (voltmeter) with an internal resistance R (the input impedance) is used to measure the potential difference between these two electrodes, the instrument draws current according to Ohm's law, I = V/R. For example, if the cell voltage V is 0.5 V and the internal resistance of the voltmeter is 1000 Ohm, then I = V/R = 0.5 $X10^{-3}$ A. Many electrodes will change their potential during measurement as a result of this high current. However, if the cell voltage V is 0.5V and the internal resistance of the voltmeter is 1 X 10^{10} Ohm, then I = V/R = 5 x 10^{-11} A. This very low current will not change the potential of a reference electrode. Thus, a voltage-measuring instrument should have high internal resistance.

2.1.2.4 Reference electrode

The primary requirement in the selection of a reference electrode is that it should not change its potential during the measurement procedure. The ideal standard electrode is always at the equilibrium potential. It resists changes in potential; the potential across interface changes under

extreme conditions only, a significant change of input potential.

Now, we discuss four types of reference electrodes: hydrogen, calomel, silver-silver chloride, and mercury-mercurous sulfate electrodes.

Hydrogen Electrode:

The hydrogen electrode is made of platinum wire in contact the hydrogen gas and solution containing hydrogen ions (Figure 9). Since hydrogen gas and hydrogen ions are present at the electrode-solution interface, this electrode can be represented as Pt | H^+| H2, and the electrode reaction is $2H^+ + 2e \leftrightarrow H_2$

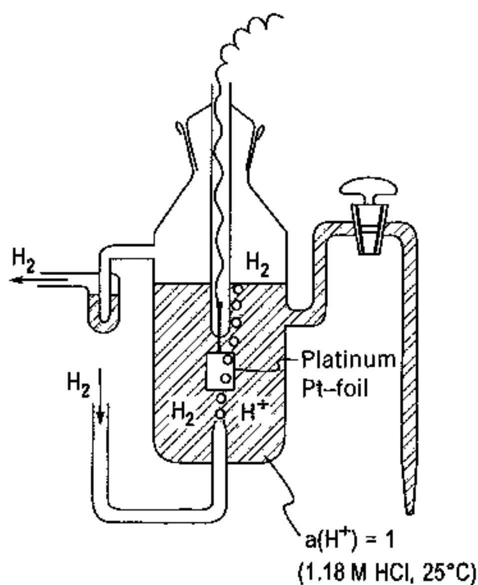

Figure 9 Hydrogen electrode

Platinum in the hydrogen electrode acts as a source or sink of electrons but does not take part in the reaction. It provides electrical contact between H_2 and the solution containing H^+ ions and

serves as a catalyst for the electrode reaction. The equilibrium between hydrogen gas and H^+ ions in this reaction is established slowly when a bright Pt (or Pd) is used. Equilibrium in the hydrogen electrode reaction is established faster if the active area of the Pt electrode is large. A large surface area is produced by electrolytic deposition of a finely divided layer of platinum ("platinum black"; platinized platinum).

For a partial hydrogen pressure of 1 atm and a concentration of 1.18 M HCl at 25ºC HCl (the source of H^+ ions), we obtain $E = E_0$ = the standard hydrogen electrode potential. By convention, the standard hydrogen electrode potential $E^0(H^+/H_2)$ is taken as zero at all temperatures.

Metal/ Insoluble Salt / Ion Electrodes

Electrode potentials are usually reported relative to the normal hydrogen electrode [NHE], but they are actually measured with respect to a secondary reference electrode. Frequently used secondary reference electrodes are calomel, silver-silver chloride, and mercury- mercurous sulfate electrodes. These secondary reference electrodes consist of a metal M covered by a layer of its sparingly soluble salt MA immersed in a solution having the same anion (A^{z-}) as the sparingly soluble MA. The generalized reference electrode of this type may be represented as M | MA | A^{z-} and may be considered to be composed of two interfaces: one between the metal electrode M and the metal ions M^{z+} in the salt MA: $M^{z+} + z \leftrightarrow M$, and the other between A^{z-} anions in the solution and the A^{z-} anions in the salt MA:

$$\mathrm{MA} \leftrightarrow M^{z+} + A^{z-}$$

The overall electrode reaction is thus:

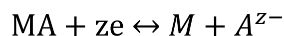

$$\mathrm{MA} + \mathrm{ze} \leftrightarrow M + A^{z-}$$

Calomel Electrode

The calomel electrode consists of mercury covered with mercurous chloride (calomel) in contact with a solution of KCl: Hg | Hg_2Cl_2| Cl^-

The overall electrode reaction in the calomel electrode is:

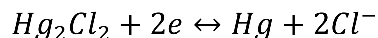

$$Hg_2Cl_2 + 2e \leftrightarrow Hg + 2Cl^-$$

The most frequency used calomel electrode is the saturated calomel electrode (SCE), in which the concentration of KCl is at saturation (about 3.5 M) (Figure 10). The potential of the SCE, at 25ºC, is 0.242 V versus NHE. SCE has a significant temperature coefficient, however, making it less frequently used in some applications: $E = 0.242 - 7.6 \times 10^{-4}(T - 25)$, where T is the temperature in Celsius.

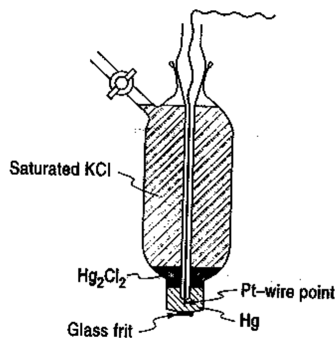

Figure 10 Saturated calomel electrode

Silver-Silver Chloride Electrode

This reference electrode consists of a pure silver wire in a solution of KCl saturated with solid silver chloride. The electrode reaction is $AgCl + e \leftrightarrow Ag + Cl^-$. If saturated KCl solution is used the potential of this electrode at 25ºC is 0.497 V versus NHE or -0.045 V versus SCE.

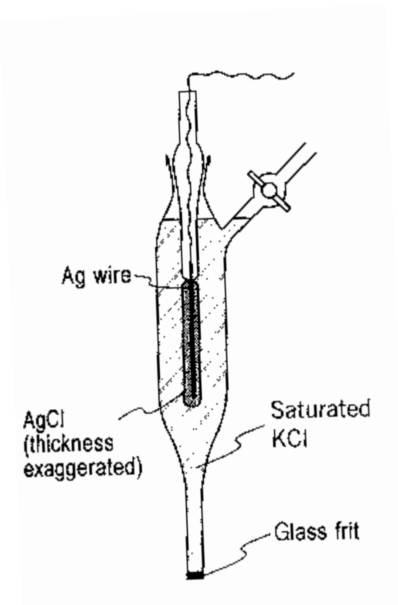

Figure 11 Silver-silver chloride electrode

Mercury-Mercurous Sulfate Electrode

In this reference electrode, the metal is mercury, the sparingly soluble compound is mercurous sulfate (Hg_2SO_4), and the source of SO_4^{2-} anions is sulfuric acid or potassium sulfate. The electrode is made in the same way as a calomel electrode, and it is represented as $Hg \mid Hg_2SO_4 \mid SO_4^{2-}$

When saturated potassium sulfate solution is used, the potential is 0.64 V versus NHE, and 0.40 V versus SCE.

The relationships between the reference electrodes discussed above are shown in Figure 12.

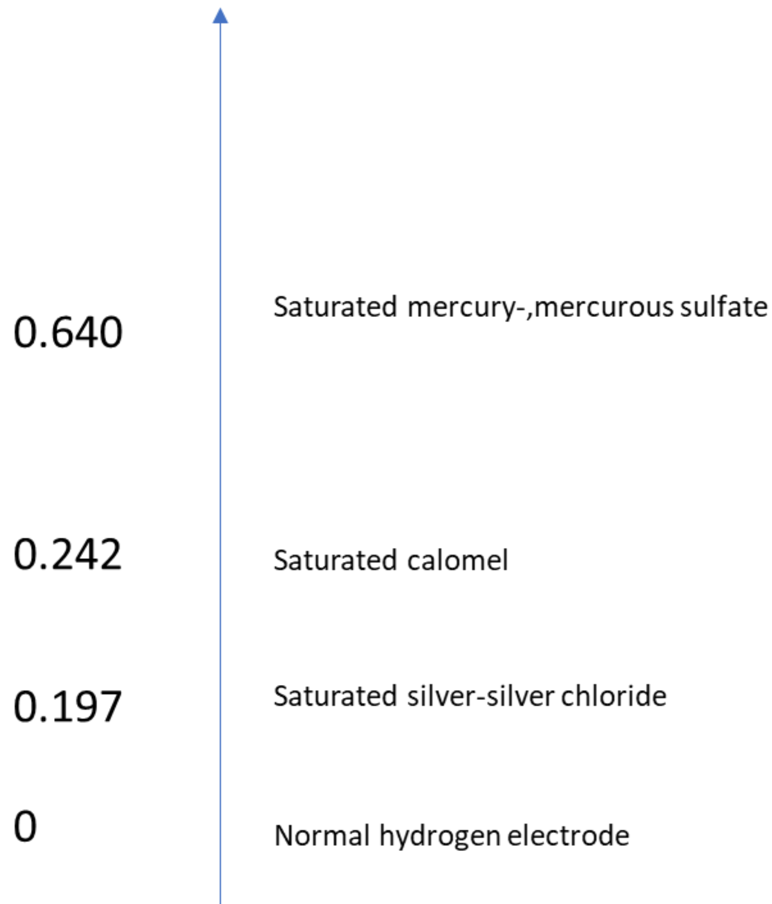

Figure 12Reference electrodes

We have seen that one can determine the relative electrode potential by measuring cell voltage. To form a series of relative electrode potentials, one has to select a reference electrode and standard conditions of components of an electrode/electrolyte interphase.

2.1.2.5 Concentration Dependence of Metal / Metal-ion Potential.

A metal/metal-ion electrode consists of a metal immersed in a solution containing ions of the metal. The electrode potential of this electrode depends on the concentration (more precisely, the activity) of the metal ions M^{z+} in solution.

In the general case of a metal/metal-ion electrode, a metal M is in equilibrium with its ions in the

solution: $M^{z+} + ze \leftrightarrow M$

Reaction from left to right consumes electrons and is called reduction. Reaction from right to left liberates electrons and is called oxidation. The potential of this electrode is defined:

$$E = E^0 + \frac{RT}{ZF}\ln[M^{z+}]$$

Where R is the gas constant, T is the absolute temperature, z the number of electrons involved in the reaction, F the Faraday number (96500 C). The bracket, in general, signifies the concentration of the species inside the brackets. This is called the Nernst equation

2.1.2.6 STANDARD ELECTRODE POTENTIALS

We have seen that one can determine the relative electrode potential by measuring cell voltage. To form a series of relative electrode potentials, one has to select a reference electrode and standard conditions of components of an electrode/ electrolyte interphase. Using a standard hydrogen electrode as a standard electrode, the standard electrode potential of other electrode is obtained by measuring the cell potential.

Table 1 The standard potential reduction

Metal/Metal-Ion Couple	Electrode Reaction	Standard Value (V)
Au/Au^{+}	$Au^{+} + e \rightleftharpoons Au$	1.692
Au/Au^{3+}	$Au^{3+} + 3e \rightleftharpoons Au$	1.498
Pd/Pd^{2+}	$Pd^{2+} + 2 \rightleftharpoons Pd$	0.951
Cu/Cu^{+}	$Cu^{+} + e \rightleftharpoons Cu$	0.521
Cu/Cu^{2+}	$Cu^{2+} + 2e \rightleftharpoons Cu$	0.3419
Fe/Fe^{3+}	$Fe^{3+} + 3e \rightleftharpoons Fe$	−0.037
Pb/Pb^{2+}	$Pb^{2+} + 2e \rightleftharpoons Pb$	−0.1262
Ni/Ni^{2+}	$Ni^{2+} + 2e \rightleftharpoons Ni$	−0.257
Co/Co^{2+}	$Co^{2+} + 2e \rightleftharpoons Co$	−0.28
Fe/Fe^{2+}	$Fe^{2+} + 2e \rightleftharpoons Fe$	−0.447
Zn/Zn^{2+}	$Zn^{2+} + 2e \rightleftharpoons Zn$	−0.7618
Al/Al^{3+}	$Al^{3+} + 3e \rightleftharpoons Al$	−1.662
Na/Na^{+}	$Na^{+} + e \rightleftharpoons Na$	−2.71

2.1.3 Atomic Processes and Parameters in Electrodeposition

When a direct electric current passes through an electrolyte, chemical reactions take place at the contacts between the circuit and the solution. This process is called electrolysis. Electrolysis takes place in an electrolytic cell. Electroplating is one specific type of electrolysis. Besides electroplating, electrolysis has also been widely used for the preparation of halogens and notably chlorine, and refining of metals, such as copper and zinc.

Oxidation/Reduction

On a broader sense, all electron-transfer reactions are considered oxidation equal to reduction. The substance gaining electrons (oxidizing agent, or oxidant) oxidizes the substance that is losing electrons (reducing agent, or reductant). In the process, the oxidizing agent is itself reduced by the reducing agent. Consequently, the reduction process is sometimes called electronation, and the oxidation process is called ‘‘de-electronation.’’ Because a cathode is attached to the negative pole of the electric source, it supplies electrons to the electrolyte. On the contrary, an anode is connected to the positive pole of the electric source; therefore, it accepts electrons from the electrolyte. Various reactions take place at the electrodes during electrolysis. In general, reduction takes place at the cathode, and oxidation takes place at the anode.

Anode and Cathode Reactions

Electrodeposition involves the reduction of metal ions from electrolytes. At the cathode, electrons are supplied to cations, which migrate to the anode. In its purest form, the reaction in an aqueous medium at the cathode follows the equation:

$$M^{n+} + ne^- \rightarrow M$$

With a similar anode reaction. At the anode, electrons are supplied to the anions, which migrate to the anode. The anode material can be either a sacrificial anode or an inert anode. For the sacrificial anode, the anode reaction is:

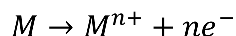

$$M \rightarrow M^{n+} + ne^-$$

2.1.3.1 Faraday's Laws of Electrolysis

In 1833, the English scientist, Michael Faraday, developed Faraday's laws of electrolysis. Faraday's first law of electrolysis and Faraday's second law of electrolysis state that the amount of material deposited on an electrode is proportional to the amount of electricity used. A number of different substances liberated by a given quantity of electricity are proportional to their electrochemical equivalent (or chemical equivalent weight). In the SI system, the unit amount of charge and the unit are coulombs(C); one coulomb is equivalent to one ampere flowing for one second. The electrochemical equivalent of an element is its atomic weight divided by the valence change involved in the reaction.

Depending on the specific response, one element may have different equivalent weights, although it has only one atomic weight. In detail, to reduce one mole of a given metal from a metal ion with the valence charge of n+, n moles of electrons are required. That is, the total cathodic charge used in the deposition, Q(C), is the product of the number of gram moles of the metal deposited, m, the number of electrons taking part in the reduction, n, Avogadro's number,

Na (the number of atoms in a mole), and the electrical charge per electron, Qe(C). Thus, the following equation gives the charge required to reduce m moles of metal:

$$Q = mnN_aQ_e$$

The product of the last two terms is the Faraday constant, F. Therefore, the number of moles of the metal reduced by charge Q can be obtained as:

$$m = \frac{Q}{nF}$$

The Faraday constant represents the amount of electric charge carried by 1 mol, or the Avogadro's number of electrons. The Faraday constant can be derived by dividing Avogadro's number, or the number of electrons per mole, by the number of electrons per coulomb. Therefore,

$$F = \frac{6.02 \times 10^{23}}{6.24 \times 10^{18}} = 9.65 \times 10^{4} C/mol$$

On the other hand, the total charge used in the deposition can be obtained as the product of the current, I(amp), and the time of deposition, t (sec), if the deposition current is held constant. Alternatively, if the current varies during the deposition,

$$\mathrm{Q} = \int Idt$$

The weight of the deposit, W(g), thus can be obtained by multiplying the number of moles of metal reduced with the atomic weight, Mw, of the deposited metal:

$$\mathrm{W} = \frac{M_w}{nF} \int \mathrm{Idt}$$

Ideally, the deposition thickness, d (cm), can be solved by:

$$d = \frac{W}{\rho A} = \frac{M_w}{\rho A n F} \int \mathrm{Idt}$$

Where r is the density of the metal (g/cm^3), and A is the area of deposition (cm^2).

Faraday's laws give a theoretical prediction of electrodeposition in an ideal situation. In a real application, many factors influence the coating quantity and quality.

Current efficiency

It is stated in Faraday's laws that the amount of chemical charge at an electrode is precisely proportional to the total amount of electricity passing. However, if several reactions take place simultaneously at the electrode, side reactions may consume the product. Therefore, inefficiencies may arise from the side reactions other than the intended reaction occurring at the electrodes. Current efficiency is a fraction, usually expressed as a percentage, of the current passing through an electrolytic cell (or an electrode) that accomplishes the desired chemical reaction. Or,

$$\text{Current efficiency} = 100 \times W_{ACT}/Q_{theo}$$

where W_{Act} is the weight of metal deposited or dissolved, and W_{Theo} is the weight to be expected from Faraday's laws if there is no side reaction. Note that the cathode efficiency is the current efficiency applied to the cathode reaction, and the anode efficiency is the current efficiency applied to the anode reaction.

Current density

Current density is defined as current in amperes per unit area of the electrode. It is a critical

variable in electroplating operations. It affects the character of the deposit and its distribution.

Current distribution

The local current density on an electrode is a function of the position on the electrode surface. The present distribution over an electrode surface is complicated. Current will tend to concentrate at edges and points, and unless the resistance of the solution is small, it will flow to the workpieces near the opposite electrode more readily than to the more distant workpieces. It is desired to operate processes with uniform current distribution. That is, the current density is the same at all points on the electrode surface.

2.1.3.2 The voltage-current relationship: Ohm's law

In electroplating, sufficient voltage should be provided by the power source. The voltage-current relationship follows Ohm's law. The concepts of electrode potentials, equilibrium electrode potential, overpotential, and overvoltage are of fundamental importance.

The current is driven by a potential difference, or voltage through the conducting medium, either electrolytic or metallic. The voltage necessary to force a given current through a conductor is given by Ohm's law:

$$\mathrm{E} = \mathrm{IR}$$

E is the voltage (V) and R the resistance of the conductor (Ω).

The electrode potential is the electrical potential difference between an electrode and a reference electrode. The absolute potential of an electrode is not directly measurable. Therefore, the electrode potential must always be referred to an arbitrary zero point that is defined by the potential of the reference electrode.

Open circuit potential

When a metal is immersed in a solution containing ions of that metal, equilibrium is set up between the tendency of the metal to enter solution as ions and the opposing tendency of the ions to lose their charge and deposit on or in the metal.

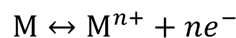

$$\mathrm{M} \leftrightarrow \mathrm{M}^{n+} + ne^{-}$$

Depending on the conditions of the system, this can occur in either direction. At equilibrium, the driving forces for metal ions being discharged and metal atoms being ionized are equal. The potential difference between the metal and the solution phases under these conditions is the equilibrium potential difference. The equilibrium electrode potential is the electrical potential of an electrode measured against a reference electrode when there is no current flowing through the electrode. It is also called open circuit potential (OCP).

The equilibrium potential between a metal and a solution of its ions is given by the Nernst equation as follows:

$$\mathrm{E} = E^{0} + \frac{RT}{nF} lna$$

Where E^0 is the standard electrode potential, which is a constant characteristic of the material of

the electrode; R the gas constant; T the absolute temperature (K); F the Faraday constant; n the valence change; an Activation Energy of the metal ion. In approximation, the concentration of the metal ion can be used instead of the activity.

If numerical values are substituted for R and F, and T is at room temperature (298 K), and base 10 logarithms are used instead of nature logarithm, the Nernst equation can be expressed as:

$$\mathrm{E} = E^0 + \frac{0.059}{n} loga$$

The standard potential of an electrode E^0 is the potential of an electrode in contact with a solution of its ions of unit activity. The standard potentials are always expressed against the standard hydrogen electrode, the potential of which is zero by definition. The standard potentials are a function of temperature; they are usually tabulated for room temperature. Standard electrode potential is also called normal electrode potential.

Overpotential and overvoltage

The equilibrium is dynamic with metal ions being discharged and metal atoms being ionized, but these two effects cancel each other, and there is no net change in the system. For the realization of metal deposition at the cathode and metal dissolution at the anode, the system must be moved away from the equilibrium condition. An external potential must be provided for the useful electrode reactions to take place at a sufficient rate; this obvious potential may have several causes. Besides, overpotential is the difference in the electrode potential of an electrode between its equilibrium potential and its operating potential when a current is flowing. The overpotential

represents the extra energy needed to force the electrode reaction to proceed at a required rate (or its equivalent current density). Consequently, the operating potential of an anode is always more positive than its equilibrium potential, while the operating potential of a cathode is always more negative than its equilibrium potential.

The overpotential increases with increasing current density. The value of the overpotential also depends on the fixed speed of the electrode reaction. A slow response (with small exchange current density) will require a larger overpotential for a given current density than a fast response (by a meaningful exchange current density). Overpotential is also referred to as polarization of the electrode.An electrode reaction always occurs in more than one simple step, and there is an overpotential associated with each step. Even for the simplest case, the overpotential is the sum of the concentration overpotential and the activation overpotential.

Overvoltage is the difference between the cell voltage (with a current flowing) and the open-circuit voltage (OCV). The overvoltage represents the extra energy needed to force the cell reaction to proceed at a required rate. Consequently, the cell voltage of an electrolytic cell is always more than its OCV, while the cell voltage of a galvanic cell (e.g., a rechargeable battery during discharging) is always less than OCV. Occasionally, it is also referred to as polarization of the cell. The overvoltage is the sum of the overpotentials of the two electrodes of the cell and the ohmic loss of the cell. Unfortunately, the terms overvoltage and overpotential are sometimes used interchangeably.

2.1.4 Applications of Electrodeposition

The electrodeposition of metals requires only that the electrode potential be more negative than the equilibrium potential, and a single parameter, the applied potential, controls the departure from electrochemical equilibrium and, therefore, the deposition rate. The difference between the applied potential and the equilibrium potential is called the overpotential. Because the electrode must be poised at a potential for deposition to occur, the substrate must be a conductor or semiconductor.

Electrodeposition can produce a dense, uniform, and adherent coating, usually of metal or alloys, upon a surface by the act of electric current. The coating produced is typically for decorative, protective purposes, or enhancing specific properties of the surface. The surface can be conductors, such as metal, or non-conductors, such as plastics. Electroplating products are widely used in many industries, such as automobile, ship, airspace, machinery, electronics, jewelry, defense, and toy industries.

2.14.1 Applications in Semiconductor Technology

Some of the most active areas in modem applications of electrochemical deposition are semiconductor technology and magnetic recording. One significant recent advance in the silicon-based semiconductor industry is the development of copper interconnects on chips. This new technology replaces aluminum or aluminum alloy (e.g., Al-Cu) conductors produced by vacuum-based deposition techniques with copper conductors manufactured by electrodeposition.

Since 1999, copper has been replacing aluminum, due to its low-bulk electrical resistivity and superior electromigration resistance. The electrical resistivities of pure Al and Cu are 2.9 and 1.7

μΩ cm, respectively, and that for Al alloys is 3 to 4 μΩ cm. Activation energies for electromigration, using identical structures and experimental conditions, are 0.81 (±0.03) and 1.1 (±0.I) eV for Al (0.5wt % Cu) and Cu, respectively. Lower electrical resistivity results in higher-speed devices. Higher electromigration resistance (higher activation energy for electromigration) results in higher reliability and thus a lower interconnect failure rate.

The change from Al to Cu interconnects required a change in the fabrication process. The metal Reactive Ion Etching (RIE) process is used in the fabrication of Al interconnects on chips. In the RIE process, chemically active ions such as F or Cl bombard the Al surface and form volatile aluminum fluorides or chlorides, which are then pumped away in the vacuum system.

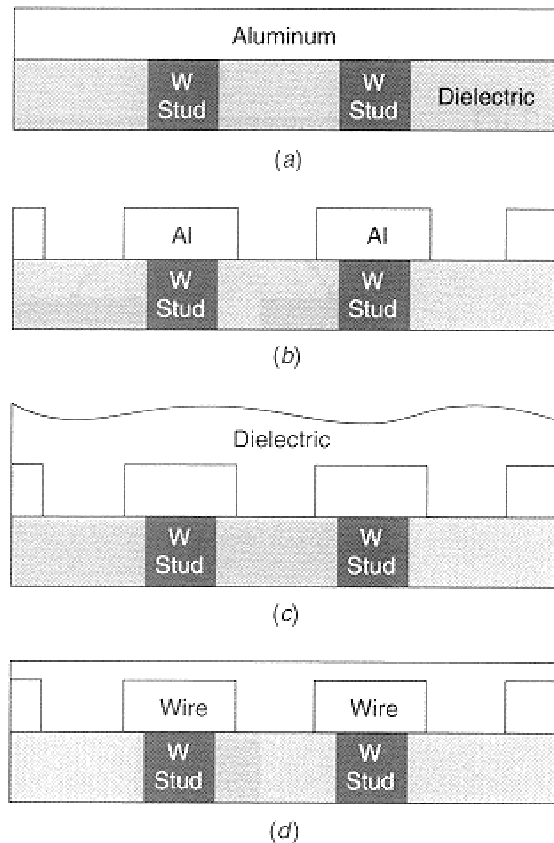

Figure 13 Process steps for forming Al interconnects using an RIE process

This process is shown in Process steps for forming Al interconnects using RIE process four steps in Figure 13. The first step in the metal-RIE process is sputter deposition of a blanket thin film of Al (or Al alloys, e.g., Al-Cu, Al-Si) over the planarized dielectric (e.g., silicon dioxide). In the next step, the unwanted metal is etched away by reactive ion etching through a photoresist mask. The features produced in this way are separated electrically isolated metal Al conductor lines. After etching, a dielectric is deposited so that it fills the gaps between the lines as well above them. In the last step, the dielectric is planarized by chemical-mechanical polishing (CMP) technique.

At present, multilevel Cu interconnections on the chip are fabricated using a different preprocess involving electrochemical deposition of Cu, since it is difficult to pattern Cu by RIE. That is so because the vapor pressure of halides is very low at room temperature.

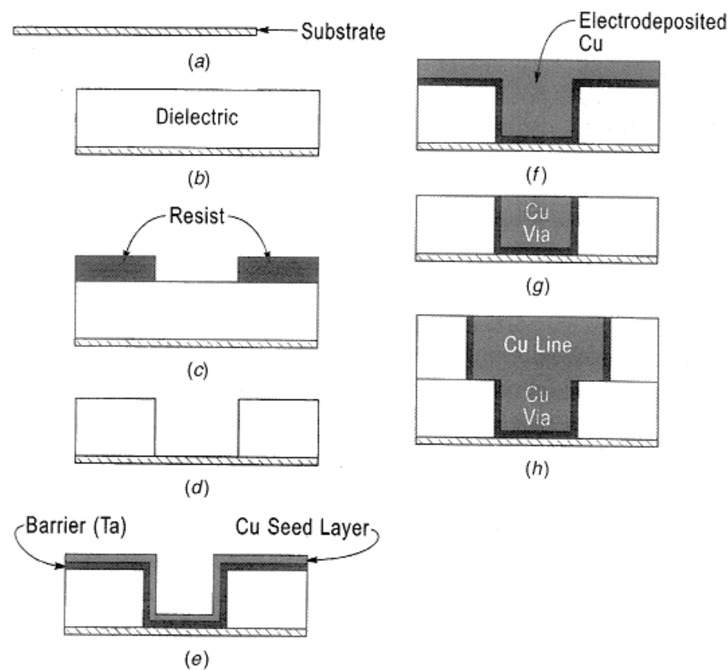

Figure 14 Process steps for forming Cu interconnects using a Damascene process

In this process, blanket Cu deposition is followed by chemical-mechanical polishing of the Cu. This approach is known as a damascene process (a process used in Damascus for centuries to form inlaid metal features on jewelry). Figure 14 illustrates the fabrication process sequence for the single damascene process. The process starts with the deposition of a dielectric layer on a Si wafer, patterning it using photolithography and a dielectric-RIE process. After patterning the dielectric, barrier metal and a Cu seed layer are deposited using a PVD or CVD technique. Finally, Cu is electrodeposited into the recesses, trenches (lines), and holes (vias). The excess of Cu deposited on the upper surface is removed by CMP.

Copper introduces new problems in the fabrication of interconnects on chips, the most important of which is the diffusion of Cu into Si, SiO2, and other dielectrics, and the reaction of Cu with Si, forming silicides. Diffusion of Cu through Si results in the poisoning of devices (transistors), and diffusion through Si02 leads to degradation of dielectrics. Thus, diffusion barrier layers are an integral part of the fabrication of copper interconnects. Barrier films isolate (encapsulate) Cu interconnects from the adjacent dielectric material. The diffusion barriers most studied are Ta, Ti, and TiN.

Since barrier metals have relatively high electrical resistivity (Ta, 12.4 μΩ cm; Ti, 80 μΩ cm), it is necessary to cover the barrier layer with a conductive metal layer. This conductive metal layer is a Cu seed layer that is deposited using PVD or CVD techniques. When the electrodeposition of the Cu on a barrier/ Cu seed layer bilayer is finished, vias and trenches are filled with Cu, and excess Cu is removed using CMP. The exposed Cu in lines needs capping with a barrier material to prevent diffusion.

2.1.4.2 Applications in computer hard disk drive

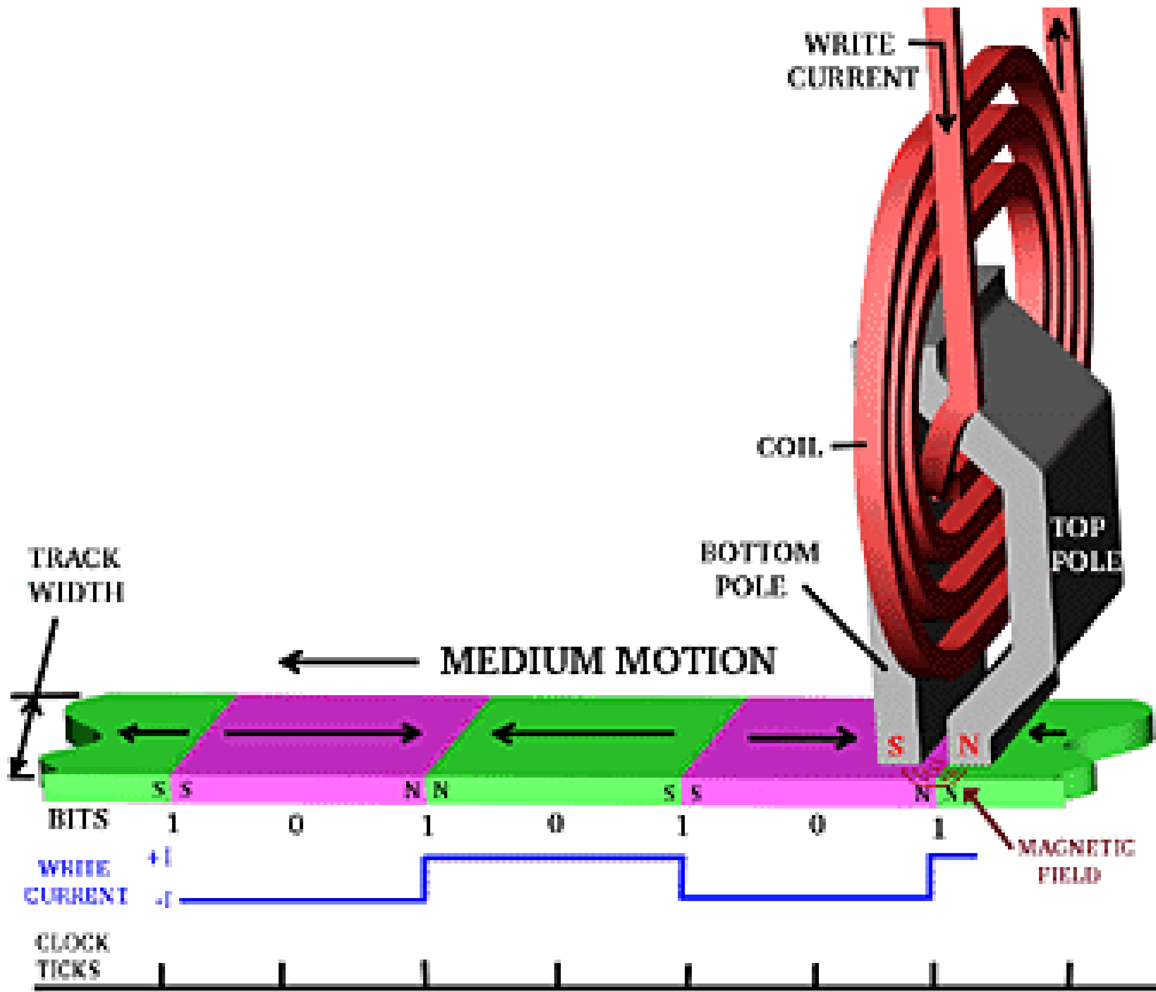

Figure 15 Computer hard disk drive write head

Inside the computer hard disk drive, the data writing uses thin-film inductive heads, which are manufactured using thin-film processes similar those of semiconductor IC technology. The thin-film head production process is somewhat unusual, as it involves both very thin and very thick films. Here, a detailed summary of the fabrication process of thin-film inductive heads with a single-layer spiral coil is presented.

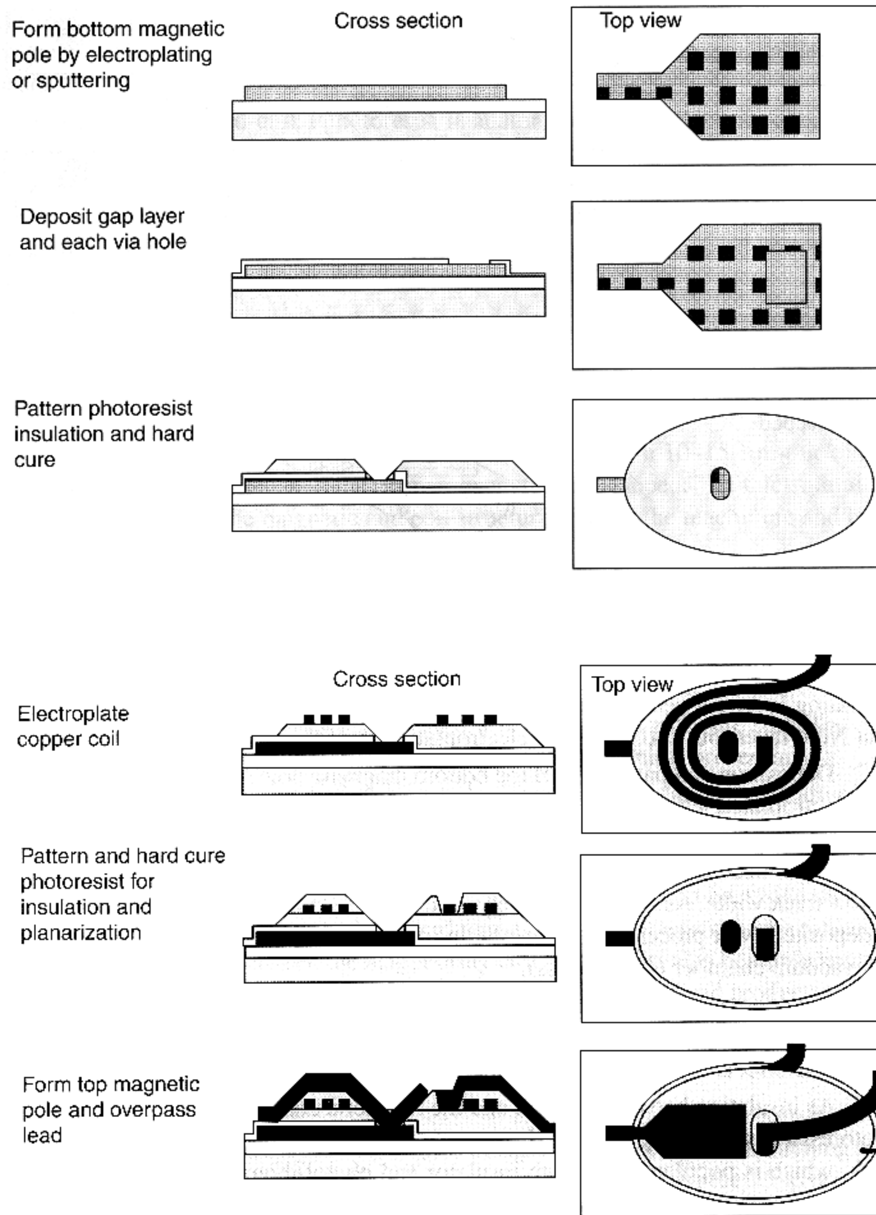

Figure 16 Thin-film write head fabrication process

1. The substrate, made of aluminum titanium carbide, will become the aerodynamic slider body of the floating head. The first step in the fabrication is the sputtering of thick alumina (~15 µm) on the polished substrate. This layer acts as an insulating layer between the substrate and the

bottom magnetic layer. A thin undercoat NiFe layer (50 to I00 nm) for electroplating is deposited, often by sputtering.

2. Deposition and patterning of the bottom magnetic pole follow. The pole is usually electroplated with a through-photoresist window frame mask to a thickness level of 2 to 4 µm. Note that whereas the magnetic pole is made into a pancake shape to increase the head efficiency, it is the narrow pole tip's dimension that determines the narrow track width. The widely used Co-based alloy magnetic poles are electrodeposited (wet process). Nanocrystalline FeN-based alloys are sputter-deposited in a vacuum chamber (dry process).

3. Next comes the sputter deposition of the alumina gap layer, made about 0.1 to 0.5 µm thick. The gap layer thickness dramatically affects the linear resolution and side read/write effects of the recording heads.

4. As insulation between the coil and the magnetic core, a hard-cured (to 200ºC) photoresist insulator is patterned. It is a polymer or polyimide about 5 µm thick, which is famous for its high insulator and photolithographic properties. This provides electrical insulation as well as a planar surface for subsequent deposition of copper coils.

5. Spiral copper coils 3 µm thick, 3 to 4 µm wide, and 2 µm apart are electrodeposited in the region above the magnetic pole. A seed layer must be put down first either through sputtering or by any other suitable means. Next, the seed layer must be selectively etched. The coils have to be made full outside the magnetic poles to reduce overall coil resistance.

6. As in step 4, hard-cured photoresist insulator about 5µm thick is patterned to provide electrical insulation for the copper coils and planarized surface for top magnetic pole deposition. Leveling

of the coated surface is essential to preserve the soft magnetic properties of the top magnetic layer. Annealing above the softening temperature of the photoresist is useful for leveling. For a multilayered coil, steps 5 and 6 are repeated.

7. The top magnetic pole, 2 to 4 µm thick, and overpass lead, which provides electrical connection to the center tap of the coils are now deposited and patterned (as in step 2). The back regions of the magnetic poles are, as a rule, made thicker than the pole tips, to achieve high head efficiency and avoid magnetic saturation.

8. Copper studs, 20 to 40 µm thick are electrodeposited, a 10-15-µm-thick alumina overcoat is deposited, and the open copper studs are lapped. The thick alumina is required to protect the magnetic and coil structures during the machining and lapping processes and to prevent corrosion.

9. Soft gold bonding pads with a seed layer are electrodeposited as above. The gold pads are required to protect the underlying devices and to facilitate wire bonding.

2.2 Cyclic voltammetry

Cyclic voltammetry (CV) may be the most versatile electroanalytical technique for investigating electroactive species. In cyclic voltammetry, the potential of a tiny, stable working electrode is alternated with time, which begins from a potential where no electrode reaction occurs and switching to potentials where reduction or oxidation of a solute (the material being researched) occurs. The versatility operated by the ease of measurement has contributed to the extensive use of CV in various fields such as organic chemistry, inorganic chemistry, and biochemistry.

Nonetheless, CV is often the first experiment performed in an electrochemical study of a compound, biological material, or an electrode surface. The outcome of CV is capable of rapidly observing the redox behavior over a wide potential range. The diagram of voltammogram is analogous to a conventional spectrum in that it conveys information as a function of an energy scan. This simple experiment becomes popular not only in chemistry but in another field because it can provide the rough understanding of new material about redox reactions in a form which is easily acquired and interpreted.

Typically, CV consists of cycling the potential of an electrode, which is immersed in an unstirred solution and monitoring the resulting current. The potential is controlled versus a reference electrode such as a saturated calomel (SCE) or silver/silver chloride (Ag/AgCl). The potential which is applied across these two electrodes can be considered as an excitation signal. As shown in Figure 17, the potential starts negatively from +0.80 to -0.20 V versus SCE,and scan back reverse direction to the original point. A second cycle is represented by the dashed line. Single or multiple cycles can be adopted. Advanced instrumentation enables switching potentials and scan rates to experiment required. A cyclic voltammogram is obtained by measuring the current at the working electrode during the potential scan. The current can be considered as a response signal to the potential applied. The diagram is an exhibited of current (vertical axis) versus potential (horizontal axis). During the same time, the potential varies linearly with time; the horizontal axis can also be thought of as a time axis.

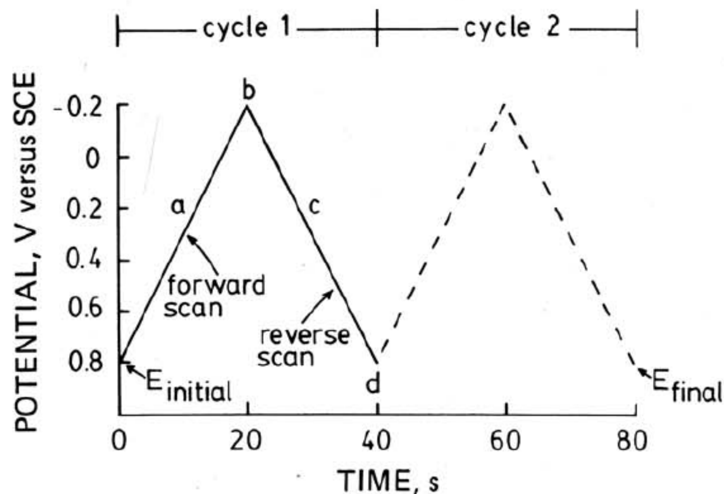

Figure 17 Typical excitation signal for cyclic voltammetry- a triangular waveform with switching potential at 0.8 and -0.2 V versus SCE.[33]

The current depends on two main steps in the overall process, the movement of electroactive material to the surface and the electron transfer reaction. The constant of electron transfer rate for a reduction process is a function of potential and can be described theoretically:

$$k_f = k^0 exp[\frac{-\alpha nF}{RT}(E - E^0)]$$

$K^0$is the standard heterogeneous electron-transfer rate constant. (The value is determined by a property of the reaction between the particular compound and the electrode surface taken.) n is the number of electrons transferred per molecule; F is the Faraday constant; R is the gas constant; T is the temperature in Kelvin, and E^0 is the formal reduction potential. The term α is known as the transfer coefficient. It arises because only a fraction of the energy that is put into the system (in the form of the applied potential) lowers the activation energy barrier. Its value increase from zero to unity depends on the shape of the free energy surfaces of the reactants and products. The exponential dependence of k_f on the applied potential causes the steep increase in

the current. However, the electrolysis of the reactant depletes its concentration near the surface. Since the experiment performed at a stationary electrode in an unstirred solution, diffusion is the primary method of driving the reactant to the surface. Relatively, the slow mode of mass transport cannot maintain a steady-state concentration profile in the region close to the electrode. Therefore, the depletion zone grows. Another word, the average distance that the reactant molecule must reach to the surface will increase. Consequently, the rate of mass transport decreases. Nonetheless, either the mass transport or a finite rate for the reverse electron transfer process is possible to prevent the current from increasing exponentially with potential. Eventually, the mass transport will be determined by the rate of mass transport and the current attains a maximum. Since the concentration gradient continues to decrease, the rate of mass transport keeps decrease causing the current to decay. Beyond the peak, the current is dependent on time and independent of the applied potential. In this diffusion-restricted region, the current is proportional to $t^{-1/2}$.

An advantage of the cyclic voltammetry experiment is the fact that a significant concentration of product (in this case, the reduced form) has been generated near the electrode on the forward scan. When the scan direction is reversed, the reduction return to the original status and the current for the reverse process is monitored.The applied potential similarly controls the electron transfer rate constant for the reverse (or oxidation) process.

$$k_r = k^0 \exp[\frac{(1-\alpha)nF}{RT}(E - E^0)]$$

2.3 Underpotential deposition

2.3.1 Introduction

What distinguishes electrodeposition from other deposition techniques is that it is also possible by underpotential deposition (UPD) to produce a highly ordered monolayer or submonolayer of metal at potentials positive of the equilibrium potential. The substrate can be single crystalline or polycrystalline. UPD occurs because the binding of the monolayer to the different substrate is stronger than the binding of the monolayer to a substrate of the same material. This phenomenon is a surface-limited reaction, because only a monolayer will be deposited, regardless of how long the UPD potential is held. Depending upon the extent of affinity with the different substrate, ions were reduced either partially or wholly to the corresponding metal at the sub-monolayer or monolayer levels.

The self-limiting action of metal UPD allows the electrochemical deposition to function as an atomic layer deposition (ALD) method. Electrochemical ALD has been used to grow compound semiconductors by sequentially depositing each element in a UPD cycle. For the atomic layer deposition of metals, a process called surface-limited redox replacement is used to produce ultrathin layers of metals such as Pt, Pd, and Ag, in which the atomic layer deposition is realized by galvanic replacement of underpotentially deposited metal monolayers of less noble metals such as Pb or Cu. The surface-limited redox replacement occurs spontaneously because the reduction potential of the less noble metal is more negative than that of the subsequent ALD layer. The two deposition steps in the surface-limited redox replacement of metals must be performed in separate solutions, so it is necessary to exchange electrolyte.

UPD provides a means of controlling the microscopic surface structure through the electrolyte composition and the applied potential. The fundamental understanding of UPD has technological importance. The observation of metallic sub-monolayers can modify the catalytic activity of a substrate significantly, and it is the first step in the liquid phase epitaxial growth of metal heterostructures.

2.3.2 Experimental Studies of UPD

Based on the amount of knowledge, UPD can be understood as a phenomenon of the first metal monolayer on the different substrate. Several studies suggested that the CV current peaks separate ordered and disorder adsorbate structures, pointing out the fact that the peaks themselves should link to phase transitions in the adsorbed layer. [34-37].

The most studied UPD process is the UPD of Cu on Au (111) in sulfate-containing electrolytes. In the past few years, this process has been investigated by electrochemical methods using cyclic voltammetry (CV), rotating ring-disk electrode measurements, chronocoulometry, chronoamperometry and quartz crystal microbalance (QCM)[38-42]. Though these electrochemical techniques are precious for the control and measure thermodynamic such parameters as potential, charge, and coverage, structural (and other) conclusions derived from measurements are implying the complicated nature and dependent on the model employed. Therefore, the advent of in-situ techniques eliminated much of the uncertainties involved and, as a result, came with a great deal of interest, especially when coupled to studies on single-crystal surfaces, and the techniques provided the opportunity of characterizing these systems under

active electrochemical control.

One of the applications was adopted by spectroscopic techniques such as FT-IR, Raman, and second harmonic generation (SHG).

The development of in situ basic techniques based on either X-ray based methods (such as grazing incidence X-ray scattering, surface extended X-ray absorption spectroscopy (SEXAFS,)and X-ray standing waves, among others) [43-45], X-ray absorption near edge structure (XANES)[43, 44, 46] or scanned probe microscopies (STM, AFM, and related methods)[47-52] further enhanced the ability to examine surfaces and surface structure at unprecedented levels of detail. But, all of these in situ primary techniques require specialized electrochemical cells and often have an interference with the electrochemical process.

Ex-situ techniques like Auger electron spectroscopy (AES), X-ray standing waves (XSW), Low-energy electron diffraction (LEED), Reflection high-energy electron diffraction (RHEED) and Auger electron spectroscopy (AES) can examine surfaces and surface structure[43, 53-55]. At unprecedented levels of detail, it has been employed to investigate the monolayer structures.

All of these studies have provided a detailed knowledge, although still not complete, of these systems, especially for Cu UPD on Au (111) or Au (100) electrodes in sulfuric acid media. UPD provides a means of controlling the microscopic surface structure through the electrolyte composition and the applied potential. The fundamental understanding of UPD has technological importance. The observation of metallic sub-monolayers can modify the catalytic activity of a substrate significantly, and it is the first step in the liquid phase epitaxial growth of metal heterostructures[56-60].

To more precisely predict the layer formed on the substrate, optical technique becomes the one common choice to tackle the problem. By applying the phase interferometer, the thickness can be measured simultaneously with the copper formation. As a result, such efforts have contributed to a considerable increase in the fundamental understanding of electrochemical progress. However, the influence of the substrate's structure on the mechanism and kinetics of the monolayer formation has been relatively less researched.

Early UPD studies were carried out mostly on polycrystalline electrode surfaces. This was due to the difficulty of preparing and maintaining single-crystal electrodes under well defined (and controlled) conditions of surface structure and cleanliness. Only a few studies on single crystal metal were performed, and they typically involved the use of ultrahigh vacuum systems and transfer protocols. Abundant of information appeared from these studies; however, due to their inherent ex-situ nature, some questions need to be answered, especially in cases involving weakly adsorbed species, as to the precise nature/identity of the surface under study. Later on, innovative instruments successfully overcome these problems of the preparation and cleaning of single-crystal surfaces, even of very reactive metals such as platinum,consequently numerous studies on single-crystal electrodes emerged.

Nowadays, the study and applications of UPD processes were triggering numerous disciplines including chemistry, physics, and materials science. The precise and delicate control of surface coverage and structure (especially when single-crystal substrates are employed) made these systems appealing for discussing issues related to interfacial reactivity including corrosion (and its inhibition), electrocatalysis, and others. Besides, these systems could also serve as a role for

studying and testing predictions from theoretical models of surface structure and growth.

In this project, we examine the underpotential deposition of metal mono- and multilayers on the gold electrode surface by an interferometry system. The intent is to provide a broad overview of the types of systems and try to derive some general observations.

2.3.3 Theoretical analysis of UPD shifts

The phenomenon of underpotential deposition (UPD) refers to the deposition of metals on different metal substrates at potentials that are more positive than that predicted by the Nernst equation for bulk deposition. It implies that the depositing adatoms are bound more strongly to the different metal electrode. Depending upon the extent of affinity with the different substrate, cations get reduced either partially or wholly to the corresponding metal at the sub-monolayer or monolayer levels.

The mechanism of UPD has been extensively investigated with various electrochemical and surface characterization techniques. Cyclic voltammetry is customarily employed to detect the UPD shift, which is the difference between the peak potentials of monolayer formation and bulk deposition. The formation of the first monolayer is inferred from the pronounced current peaks at the potential $E > Erev$ while the bulk deposition occurs at $E < Erev$ where $Erev$ denotes the Nernst equilibrium potential (for example, UPD of Cu on Au occurs at 0.46 V while bulk deposition occurs at 0.24 V, $Erev$ being 0.34 V vs. Standard Hydrogen Electrode).

Characterization techniques such as Fourier transform infrared reflection (FTIR), Surface-enhanced Raman spectroscopy (SERS), scanning tunneling microscopy (STM), atomic force microscopy (AFM), etc. provide information regarding the surface morphology. Also, low energy

electron diffraction (LEED), X-ray photoelectron spectroscopy (XPS), Auger electron spectroscopy (AES), etc. provide more insights into the structure, energetics, and composition of the various adlayers.

A rigorous theoretical analysis of the underpotential deposition of metals is inherently complex, given the fact that the components of the system, in general, include the (1) metallic substrate, (2) depositing metal ions, (3) solvent dipoles, and (4) adsorbed ionic species. Added to this multi-component system, is our ability to manipulate the system by an external potential (time-dependent or otherwise). The correlation between the experimentally observed UPD shift and the work function can vary by the substrate and the depositing metal. However, without being deterred by the complexity of the problem, several noteworthy analyses have been made by the pioneering work of the groups of Rikvold, Blum, Leiva, and Schmickler. In a way, these investigations are complementary to one another in so far as treatment is attempted with due mathematical, statistical mechanical and quantum mechanical sophistication.

Among several efforts to correlate the UPD shifts with the nature of the metallic substrate and depositing species, it can be described as equation

$$\Delta E = 0.5(\Phi_s - \Phi_m)$$

E_{UPD} denotes the experimentally observed UPD shift,and (Φ_S–Φ_M) is the difference in the work function between the substrate and depositing species. The equation is valid for most of the metal pairs, especially when polycrystalline substrates are employed. This apparently simple variation of the UPD shift is somewhat puzzling since one would anticipate a far more involved Depend on the interaction energies about solvent dipoles as well as ionic species.

Since the UPD shift denotes the difference in potential between the monolayer formation and bulk deposition, it is imperative to consider the two processes separately. The monolayer formation of M on S can be envisaged as follows (a) movement of the solvated ions from the bulk to the reaction zone, getting rid of their solvation sheath, and (b) electron transfer from the substrate to the metal ions leading to the subsequent bond formation with the substrate (S). The S–M bond formation involving the defective sites occurs after knocking off the adsorbed solvent dipoles from the appropriate sites of the substrate. We note here that since the electrode is solvated, the nature of orientation of solvent dipoles at electrode surfaces also needs to be included for a rigorous analysis.

Figure 18 depicts the constituent processes involved in the monolayer formation of M on S.

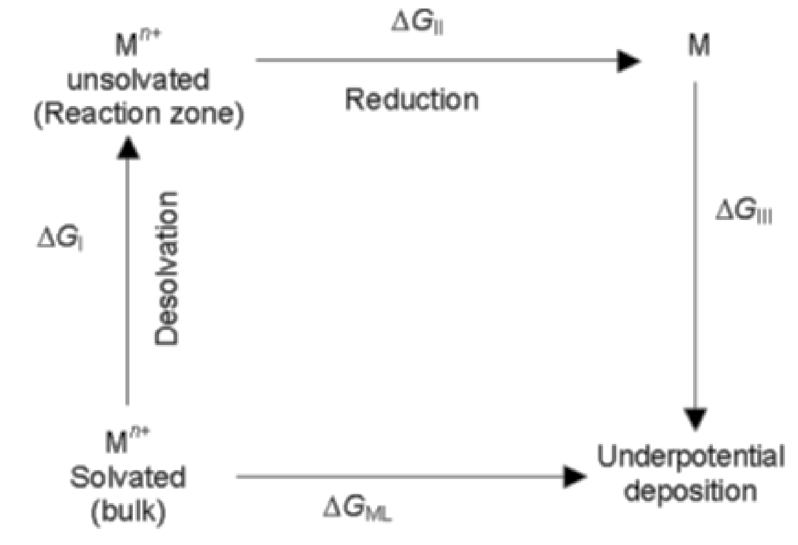

Figure 18 Thermochemical Cycle is denoting different energetic contributions participating in the monolayer formation of a metal on a different substrate [41]

Based on Figure 18, a thermochemical cycle can be constructed which leads to

$$\Delta G_{ML} = \Delta G_1 + n\Delta G_2 + \Delta G_3$$

ΔG_{ML} denotes the Gibbs free energy change in the monolayer formation.

ΔG_1 represents the work done in bringing the solvated metal ions M^{n+} from bulk to the reaction zone as

$$\Delta G_1 = \mathrm{W}_{M^{n+}}$$

While ΔG_2 comprises the free energy change involved in the electron transfer (ΔG_{et}^{S}) from the solvated electrode to the (de)solvated ions and ΔG_0 governed by the standard reduction potential E^0 of M^{n+}/M

$$\Delta G_2 = \Delta \mathrm{G}_{et}^{s} + \Delta G_0$$

ΔG_3 involves the desorption of solvent dipoles from the defective sites of the substrate and formation of the substrate–metal (S–M) bond leading to

$$\Delta G_3 = \theta(\Delta G_{desor} + \Delta G_{S-M}^{inter})$$

The subscript/superscript “et” and “inter” denote“electron transfer” and “interfacial region” respectively. ΔG_{desor} represents the Gibbs free energy change of desorption of solvent molecules from the substrate, $\Delta G_{S\text{-}M}^{inter}$ being the energy involved in the formation of S–M bond. Θ denotes the surface coverage of the underpotentially deposited metal adatoms on the substrate. Since adsorption is visualized as the replacement of solvent molecules by the depositing species, Θ is introduced in ΔG_{desor} as well as in $G_{S\text{-}M}^{inter}$.

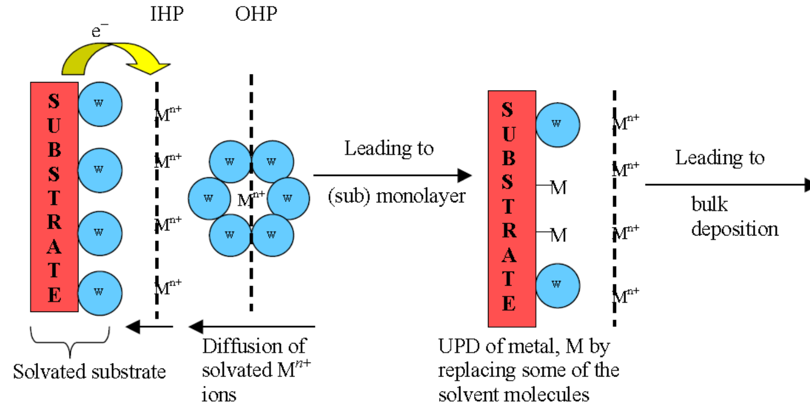

Figure 19 Schematic representation of processes constituting adsorption of M upon S. IHP and OHP indicates respectively, the inner and outer Helmholtz plane. The metal ions, Mn+ are surrounded by the solvent molecules 'w'.[41]

Substituting equation, ΔG_{ML} is obtained as

$$\Delta G_{ML} = W_{M^{n+}} + \Delta G_{et}^{s} + \Delta G^{0} + \theta(\Delta G_{desor} + \Delta G_{S-M}^{inter})$$

The terms W_M^{n+}, $\Delta G_{et}{}^{S}$ and ΔG_{desor}, involve the solvent characteristics. To compute these, the formulation of the work function of hydrated electrodes as well as the energetics involved in the binding of water molecules becomes the core. Recalling from the classification of metals into *sp* and *d*-blocks and introducing the dipole potential barrier, the surface potential of electrons in solution, etc., the potential of the monolayer adsorption follows as

$$E_{ML} = \frac{-\Delta G_{desolv}}{nFS_N} - \frac{\chi_{M^{n+}}}{n} + \frac{\Phi_s}{CN_s} + \mathrm{E}^0 - \frac{\theta \Delta G_{S-H_2O}}{nF} - \frac{\theta \Delta H_{S-M}}{nFCN_s}$$

Where ΔG_{desolv} is the bulk dehydration energy of the (depositing) metal ions, S_N being the hydration number, *n* denotes the number of electrons involved in charge transfer and $\mathcal{X}_M^{n+}$ indicates the surface potential of electrons in ma etal, CN_S and Φ_S represent the lattice coordination number and work function of the substrate respectively. The terms ΔG_{S-H2O} and ΔH_{S-M} denote respectively the Gibbs free energy change involved in the substrate–water bond

formation and enthalpy change of substrate– metal bond formation available in tabular compilations. By approximating $\chi_e{}^M$, 0.4 eV and taking other tabulated parameters such as work functions, lattice coordination numbers etc. E_{ML} can be estimated for a chosen system.

In an analogous manner, the potential for bulk deposition can be formulated *mutatis mutandis* yielding the UPD shift as

$$\Delta E_{UPD} = \theta\left\{\frac{\Phi_S}{CN_s} - \frac{\Phi_M}{CN_M}\right\} + (1-2\theta)\frac{\Delta G_{S-H_2o}}{Z_{ad}F} + (1-2\theta)\frac{\Delta H_{S-M}}{Z_{ad}FCN_s} + \frac{\theta\Delta G_{M-H_2o}}{Z_{ad}F} + \frac{\theta\Delta H_{M-M}}{Z_{ad}FCN_M}$$

Given the partial charge transfer between the depositing species and the metal, the charge on the adsorbate Z_{ad} arises instead of n – the number of electrons involved in the reduction process. A comparison with previous equation reveals the presence of the coordination number of the depositing metal (CN_M), its work function (Φ_M) as well as the energetics involved in M–H2O and M–M bond formation. In Table 2, the UPD shifts estimated from previous equation , for a small subset of forty systems that have been experimentally reported, are compared with the experimental data.

Table 2 Estimation of the UPD shift using

System	Work func. of the substrate[21] Φ_S (eV)	Work func. of the ads.[21] Φ_M (eV)	Charge on the ads.[19] z_{ad}	Surface coverage[2] θ	Coord. number of the substrate[86] CN_S	Coord. number of the ads.[86] CN_M	Calc. UPD shift ΔE_{UPD} (calc) (V)	Experi-mental UPD shift[2] ΔE_{UPD} (expt) (V)
Au/Cu^{2+}	4·80	4·55	2·00	0·18	5·56	5·56	0·18	0·22
Pt/Cu^{2+}	5·03	4·55	1·00	0·23	6·00	5·56	0·43	0·44
Ag/Tl^{+}	4·30	4·10	3·53	0·22	5·56	3·56	0·25	0·28
Ag/Cd^{2+}	4·30	4·12	2·95	0·17	5·56	4·56	0·16	0·16
Ag/Pb^{2+}	4·30	4·24	4·16	0·10	5·56	2·56	0·12	0·16
Cu/Tl^{+}	4·55	4·10	2·76	0·31	5·56	3·56	0·34	0·34
Au/Pb^{2+}	4·80	4·24	1·50	0·22	5·56	2·56	0·40	0·40

Abbreviations: func. – function; ads. – adsorbate; Coord. – coordination; Calc. – calculated

Although equation provides a preliminary methodology for evaluating the UPD shifts, it offers a framework by which further refinements can be accomplished. The correlation of the UPD shifts with work function differences inferred by Kolb[61] may essentially be ascribed to the interplay between the magnitudes of various competing factors appearing in equation. The fact that incorporation of work function differences alone is insufficient to interpret the UPD shift was pointed out more than two decades ago, and the influence of structural parameters in rationalizing the UPD shift has also been indicated. Moreover, this correlation has been explained by Leiva, regarding a thermodynamic derivation involving the adsorption energies of substrate and adsorbate.

2.3.4 Atomic Layer Electrodeposition

The self-limiting action of metal UPD allows electrodeposition to function as an atomic layer deposition (ALD) method. Electrochemical ALD has been used to grow compound semiconductors by sequentially depositing each element in a UPD cycle. For the atomic layer deposition of metals, a process called surface-limited redox replacement is used to produce ultrathin layers of metals such as Pt, Pd, and Ag, in which the atomic layer deposition is realized by galvanic replacement of underpotentially deposited metal monolayers of less noble metals such as Pb or Cu. The surface-limited redox replacement occurs spontaneously because the reduction potential of the less noble metal is more negative than that of the subsequent ALD layer. The two deposition steps in the surface-limited redox replacement of metals must be performed in separate solutions, so it is necessary to exchange electrolyte.

In 2012, against conventional wisdom that the best way to electrodeposit ultrathin metal films would be to apply either an underpotential or a very small overpotential, a paper in Science

reported that a monolayer of Pt is deposited at an overpotential of 1 V, a value at which the deposition rate of Pt should be tremendous. At this high overpotential, a monolayer of hydrogen is formed on the Pt surface, which completely blocks the deposition of additional Pt, thereby making the process self-limiting. To produce multilayers of Pt, a potential of +0.4 V is applied following the Pt and H deposition at -0.8V. At a potential of +0.4V, the hydrogen that is deposited can be desorbed. Therefore, pulsing the potential between –0.8 and +0.4 V in a single plating bath, Pt is deposited on the surface monolayer by monolayer. The deposition of a Pt monolayer is fast (complete in 1 s) and may also lead to less carryover of contaminants that occur when the reactants are exchanged in the surface-limited redox replacement method.

3. In-situ monitoring Cu monolayer formation using Phase-sensitive interferometry

As mentioned before, the Cyclic voltammetry has been widely used to investigate UPD processes, especially in the Au electrode. It has been proved that monolayer can grow up on the Au electrode surface. By using the Spectral Domain Phase Sensitive interferometry (SDPSI), it becomes possible to monitor the whole process during the experiment optically. Besides, appropriate set up of the interferometer can eliminate the noise from the working environment, improving the accuracy reading from proceeding experiment. Moreover, the sensitivity of SDSPI is good enough to distinguish the small thickness change while we measure the CV of UPD. Overall, interferometry is a powerful technique can assist us to detect extremely thin layer formation and avoid the environmental restriction compared to another in-situ study.

3.1 Phase Sensitive Interferometry

Interferometry is used in extensive application areas of astronomy, fiber optics, metrology, and biosensing. Interferometry is used for accurate measurements of distances, displacements, vibrations and surface topologies. Interferometric measurements have redefined the international standard of length in terms of speed of light. More recently, interferometer

designed to detect gravitational waves has achieved the measurements of a distance change 10,000 times smaller than an atomic nucleus (the smallest measurement ever attempted).

Interference signal or interferogram is formed when interference occurs between electromagnetic waves. In optical interferometry, the light from the source is split into two, which travel similar paths. Such split same frequency beams have precisely the same properties. Light travels through two optical paths, and interference occurs then they are recombined. Interference can either be constructive for which the waves reinforce each other (in phase) or destructive where waves cancel each other (out of phase). Any change experienced by one path changes the phase of the light signal which when recombined with light from the other unchanged path creates an interesting phenomenon of interference.

The optical interferometer can measure optical path changes with longitudinal resolutions better than the most sensitive surface-scanning microscopic techniques, such as atomic force microscope. The interferometer also measures the refractive index change. These measurements can also be considered as measuring the interferometric cross-correlation signal between an undistorted and a distorted light field.

Depending on the kind of source used, interferometry can be categorized into 2 types: Low-coherence Interferometry and Laser interferometry. Due to the long coherence length of Lasers, interference signal produced in Laser interferometry does not need precise path length matching. However, any stray reflections in Laser Interferometry can also generate an interference pattern, which can result in incorrect measurements.

Low-coherence optical interferometry methods, such as optical coherence-domain reflectometry

and spectral interferometry (SI) offering high resolution, subsurface depth profiling, and cross-sectional imaging with relatively simple optical arrangements and inexpensive light sources. These techniques are based on broadband or white-light interferometry, in which surface or depth profiling is obtained through the measurement of optical path length or phase differences between the sample and the reference arms of an interferometer.

In low coherence interferometry, low coherence source with coherence length in micrometers is taken. Low coherence length ensures that interference occurs only within coherence distance. The fringe visibility of the interference pattern is maximum when the optical path length between two beams is matched perfectly. When optical path length (OPL) is higher than the coherence length, fringe visibility decreases as the optical path length increases and disappears. Hence, depth resolution depends on the coherence length of the source; shorter coherence length gives a better spatial resolution.

Low coherence interferometry can be performed in the time domain or in the spectral domain. In time domain low coherence interferometry, the scanning mirror is used to achieve a depth probing, so recorded interferogram is a function of reflector position. Spectral domain interferometry produces interferogram as a function of wavelength, and the depth information is provided from coherence grating.

SI is used for frequency-domain implementation of low-coherence interferometry. The optical apparatus for SI is usually based on a Michelson interferometer. In a Michelson interferometer, the optical path length of the reference arm is modulated. Phase modulation of the interferometer's reference arm is required to allow interference from the reflective base at different depths in the sample. Phase-sensitive detection of the interferometer output provides

high dynamic range and depth-resolved measurement of light reflected or backscattered from the sample. Images are obtained when the light beam is scanned across the sample. High-speed image acquisition requires high-speed reference arm modulation, which cannot be done merely with the mechanical movement of a mirror. Other methods, such as piezoelectric fiber stretchers and rapid scanning phase-control delay lines, have successfully allowed video-rate OCT imaging. However, these methods can be thermally or mechanically unstable. For medical applications, in particular, it is desirable to minimize the number of moving parts in an instrument.

For SI, a stationary interferometer is used, and the spectrally dispersed output of the interferometer (the spectral interferogram) is recorded. The signal returning from the sample arm can be thought of as a superposition of monochromatic waves that interfere with similar components in the reference arm. This interference leads to fringes on the spectrum. Depth information is encoded in the fringe frequencies and is easily obtained by Fourier transform of the spectral interferogram.

Two-dimensional images can be obtained directly by use of line illumination and a camera,whereas three-dimensional images can be obtained when the light beam is scanned across the sample. With SI, signals generated from all available sample depths are recorded simultaneously.

3.1.1 Working principle of using PSI to measure the thickness

A brief summary is given here to illustrate the procedure for obtaining depth information from spectral interferogram. A spectrally broad, low-coherence beam is split into a fixed reference arm and a sample arm. Light reflected or scattered from the sample recombines and interferes with

the reference beam. The interferometer output is sent through a spectrograph to resolve the interference fringes.

Depth information is encoded in the frequency of the fringes. A simple Fourier transform extracts the depth information. With SI, all depth information is acquired simultaneously, eliminating the need for reference arm modulation. The spectrum of the interferometer output is given by

$$I_{SI}(\omega) = I_R(\omega) + I_S(\omega) + 2\sqrt{I_R(\omega)}\sqrt{I_S(\omega)} \times \cos[\emptyset_S(\omega) - \emptyset_R(\omega) - \omega\tau]$$

where $I_{SI}(\omega)$ is the interferometer output spectrum, ω expressed as intensity as a function of optical frequency . $I_R(\omega)$ is the spectrum of the light in the reference arm, and $I_S(\omega)$ is the spectrum of the light returning from the sample arm. Φ_R is the reference arm phase, Φ_S is the sample arm phase, and τ is a fixed optical delay between the two arms chosen by the experimenter.

Equation consists of three terms. The first two terms are the reference and sample arm spectra. The third term is the interference between the reference and the sample arms and contains the depth (phase) information. This is a simplified presentation.Not shown are autocorrelation terms, which arise from interference between surfaces within the sample. Autocorrelation terms can appear as artifacts and coherent noise in SI images, reducing the image clarity and dynamic range.

To facilitate extracting the depth-resolved signal from the SI output, we choose τ to yield fringes in the sum spectrum, i.e., so that the optical paths are nearly equal. This delay then remains fixed, and optical path differences are resulting from backscattering or reflection from various depths in the sample are encoded in the interference fringes. The spectral fringes have a period inversely proportional to the optical path difference between the two beams.

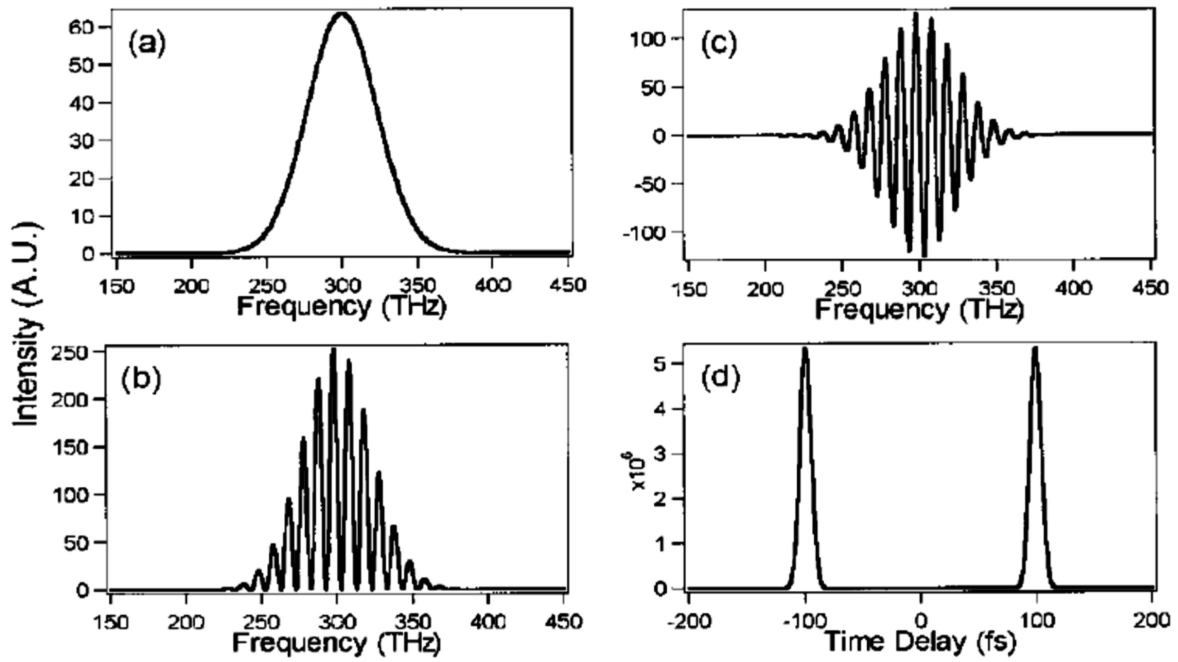

Figure 20 Calculated SI data for a single reflective surface. (a) Input light source spectrum. (b) Output spectral interferogram.(c) Spectral interferogram with the input spectrum removed. (d)Fourier transform of the spectral interferogram.[62]

Figure 20 shows the steps required to obtain the phase difference between the two arms. As an example, we will calculate the result for a single reflecting surface. Figure 20 (a) shows the model spectrum of a spectrally broad input beam. (b) shows the output spectrum, $I_{SI}(\omega)$. The fringe spacing is proportional to the optical delay between the two arms. The first step is to subtract the individual spectra, $I_R(\omega)$ and $I_S(\omega)$, to isolate the spectral interferogram S(ω),

$$S(\omega) = 2\sqrt{I_R(\omega)}\sqrt{I_S(\omega)} \times \cos[\emptyset_S(\omega) - \emptyset_R(\omega) - \omega\tau]$$

the result is shown in Figure. 20(c). By Fourier transforming S(ω), we obtain

$$F^{-1}[S(\omega)] = f(t-\tau) + f(-t+\tau)$$

where f (t) is the correlation product between the reference and the sample fields Figure. 20(d). In this example, reflection from a single depth in the sample results in a simple function of

intensity-versus-time delay. Note that mirror images off (t) occur at positive and negative delays. The time delay corresponds directly to distance.

$I_S(\omega)=I_R(\omega)$ when there is no significant absorption by the sample that changes the spectral profile of the light returning from the sample. In this case, subtraction of $I_S(\omega)$ and $I_R(\omega)$ before the Fourier transform is feasible. However, this is not necessary. If the individual spectra are left in the spectral interferogram, they will appear as a background feature centered around zero in the time domain.

The previous example is a simple case in which light is returned from only one depth in the sample. More complex sample structures will lead to multicomponent spectral interferograms. However, the mathematical treatment remains simple, requiring only Fourier transformation of the spectral interferogram to obtain signal intensity as a function of depth.

Here we put an example for explanation of Spectral domain principle which termed as a cosine function. Recalling the equation

$$I_{SI}(\omega) = I_R(\omega) + I_S(\omega) + 2\sqrt{I_R(\omega)}\sqrt{I_S(\omega)} \times \cos[\emptyset_S(\omega) - \emptyset_R(\omega) - \omega\tau]$$

If we put $I_S(\omega)$, and $I_R(\omega)$ equal to 1 the *equation* turns into

$$I_{SI}(\omega) = 2 + 2 \times \cos[\emptyset_S(\omega) - \emptyset_R(\omega) - \omega\tau]$$

After subtraction, the depth information encoded in the cosine function.

$$S(\omega) = 2 \times \cos[\emptyset_S(\omega) - \emptyset_R(\omega) - \omega\tau]$$

Here we provide a sample for 1 nm added on the top of 200 nm and plotted as a cosine function

with intensity corresponding wavelength.as shown in Figure 21 and 22.

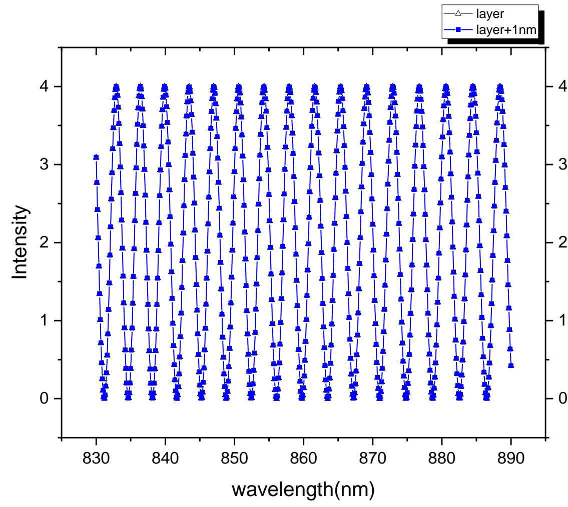

Figure 21 the fringe pattern of sample and sample +1nm

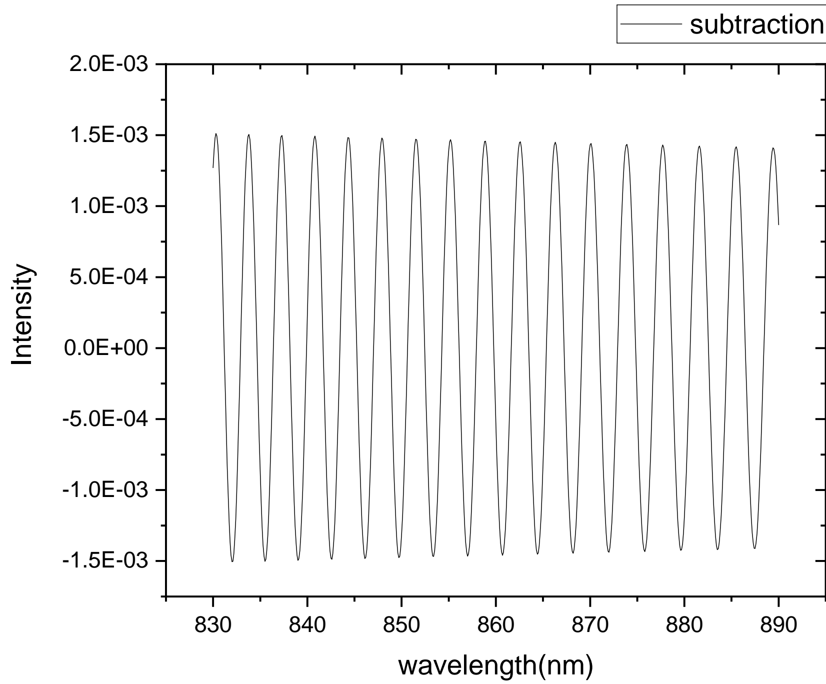

Figure 22 the subtraction fringe pattern of sample and sample +1nm

3.1.2 Working principle of Spectral Domain Low Coherence Interferometer (SD-LCI)

Spectral Domain Low Coherence Interferometer (SD-LCI) is a non-contact sensing modality. The interference signal obtained from low coherence light source is spatially and temporally localized which allows for measurement of small distances reflected from different layers of the sample. The SD-LCI analyses superposition of spectrums reflected from the sample and reference arms and hence uses spectrometer as the detection system to measure a total intensity as a function of wavelength.SD-LCI can be performed using either two path or common path geometry. In two-path geometry, two beams travel in physically separated paths and recombine after reflected off to produce an interferogram. In common path geometry, two beams travel along the same route and recombine after reflected off to produce an interferogram.

Figure 23 shows a simplified low coherence two paths interferometric setup. As shown in the Figure, light from the broadband source is split into two beams using a beam splitter. One beam travels toward the reference (mirror) and is reflected back. The other beam travels towards the sample and is reflected back. LCI measures the delayed echo time between the backscattered light from the sample and reference path. These two beams are superimposed and create an interference pattern, which is detected by the spectrometer. This interference pattern gives the information about the sample. SD-LCI cannot be used to measure a thin metal layer because of phase noise from the two-path interferometer is in hundreds of nanometers. For measuring a thin metal layer, a number below the picometer range of noise is needed for sensitive detection.

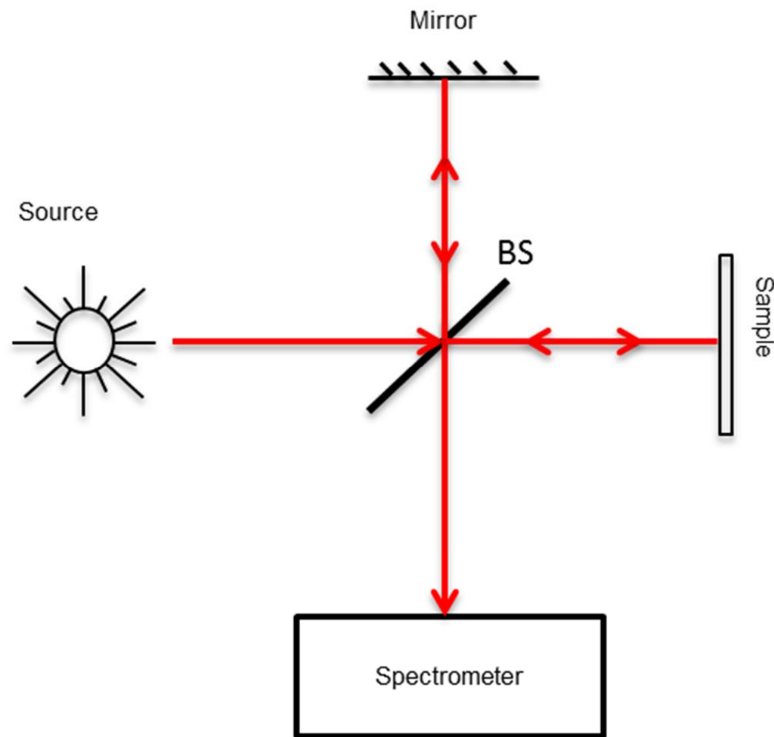

Figure 23 Low coherence two-path interferometric setup. Light from the source is split in two using beamsplitter (BS) which after reflecting back from reference and sample path are recombined to produce interference fringes detected by the spectrometer.

In order to perform sensitive phase measurements of sub-nanometer thickness change using low coherence single-path interferometry, only one path geometry is used which is shown in Figure 24. Both sample and reference beam travel along the same path. The reference signal is generated from the bottom of the sample (microscopy glass slide), and the sample signal is generated from the top of the sample. This geometry can help in the quantification of phase changes that occur when there is an optical path length change in the sample and hence helps in ultrasensitive detection.

As compared to two-path geometry, common path interferometry is resistant to environmental factors because the environmental factors affect both reference and sample beams equally. This

setup cancels noise and gives the higher stability and sensitivity system.

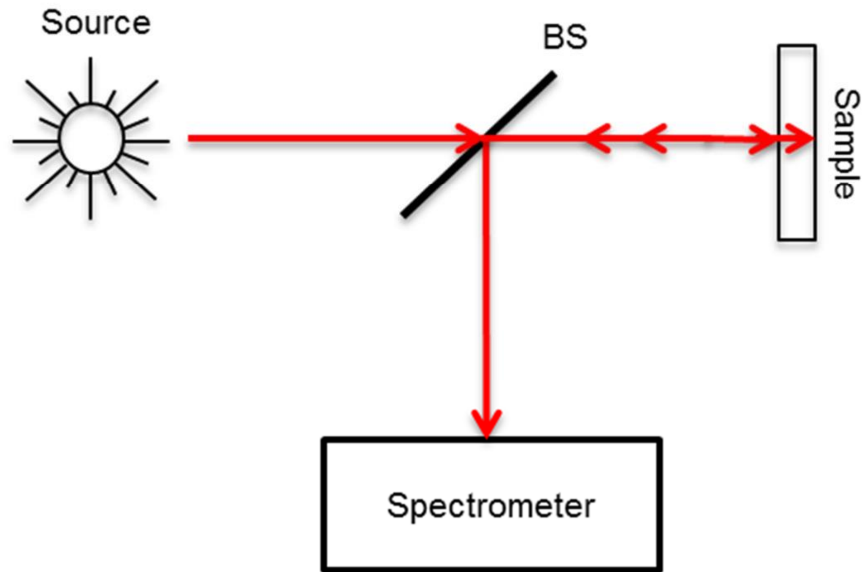

Figure 24 Low coherence single-path interferometric configuration (common mode interferometry). Light from the source is transmitted through a beamsplitter (BS), which gets reflected back from top and bottom surface of the sample and are recombined to produce interference fringes detached by the spectrometer.

This technique is a real-time measurement with sensitivity in picometer to nanometer range. This technique can be applied for detection of a metal layer and biomolecules with high sensitivity in the nanometer range. The signal detected by spectrometer has an interferometric component that contains information about amplitude and the phase of the sample. Extraction of phase information quantifies sub-wavelength variations occurring in the sample. The phase changes occur due to optical path length (OPL) changes in the sample. Optical path length is the product of distance (L) traveled by light in media of given refractive index (n) and is given by

$$OPL = n * L$$

3.1.3 Spectral Domain-Phase Sensitive Interferometer

Fiber optic configuration of spectral domain phase sensitive interferometry is implemented for the phase transformation process. Fiber optic configuration provides information about phase difference by electromagnetic interference, the flexibility of using them in different environmental conditions, which account for higher sensitivity.

The SD-PSI setup consists of superluminescent diode (SLD), 635 nm visible light source, 90:10 fiber coupler, 50:50 fiber coupler and home-built spectrometer. The bandwidth of the light source affects the smallest thickness of the transparent substrate that can be adopted and precision in thickness accuracy. The broadband SLD light source operates at 800 nm center wavelength with full-wave half-maximum (FWHW) and the coherence length of 20 nm and 14 μm respectively. Fiber coupled superluminescent diodes (SLD) are an excellent choice as broadband light sources for SD-PSI. These compact sources have a stable spectral and power output. Given the potential of damage to the SLD due to back-reflection from the optical setup, a fiber isolator should be inserted between the SLD source and the input port of the 2x2 SMF coupler. The isolator in the system is incorporated to protect SLD source from back reflections that can damage or create instability in the performance of SLD source. After isolator light is input in single axis fiber bench. This is used to attenuate the power on the sample when the signal goes in saturation.

The output port of fiber act as input to the 90:10 fiber coupler. To another input arm of the coupler, 635 nm red light source is connected to visualize the light focused on the sample. The arm with 90% of power is coupled with a 2x2 (50:50 split ratio) single mode fiber (SMF) splitter. The second coupler splits power equally in two sample paths. As shown in Figure 25, in the common path configuration only one port of the coupler is used for sensing. Any broadband light

source can be utilized as long as the spectrum of the light source is stable and sufficient light can be coupled into a single mode fiber. This single mode fiber maintains a signal-to-noise ratio that is necessary to detect a desired phase change in the spectral interference fringes. The port that is not used should be angle polished or angle cleaved to avoid any back reflection from the fiber-air interferometric signal and hence the sensitivity of the measured phase. The other port of the fiber coupler should be terminated with an FE/APC connector.

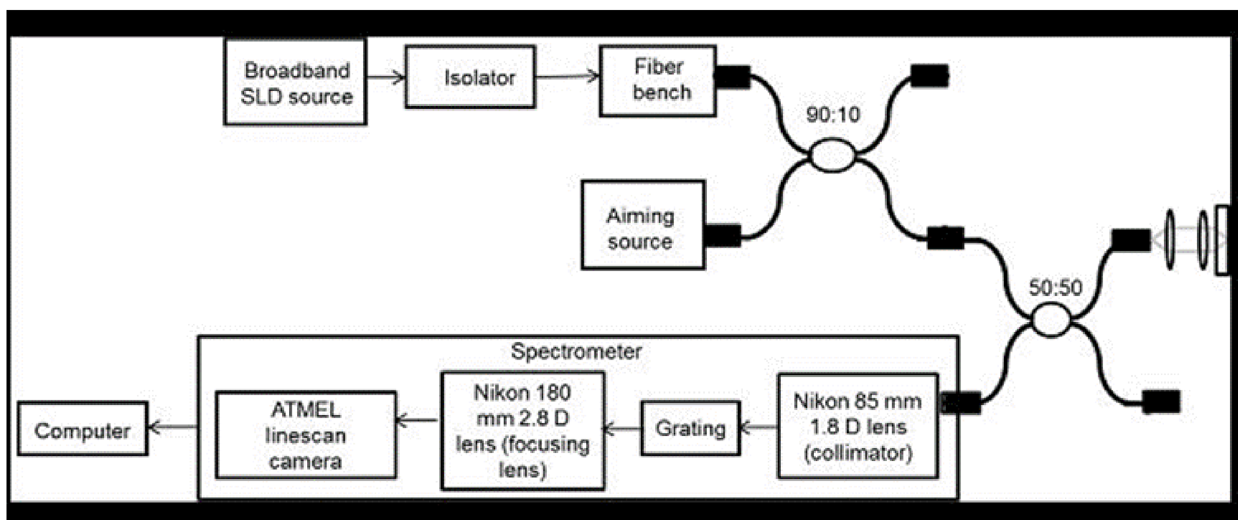

Figure 25 Optical setup of the spectral domain phase sensitive interferometer. 90:10 coupler splits combined power of 800 nm and 635 nm Laser in 90:10 ratio. 90% is input to a 50:50 coupler which after reflecting back from the sensor surface is detected by the spectrometer. Computer stores acquired interference spectrums

Light is first collimated and then focused onto the sample surface. The light is reflected back from reflective surfaces to the detector. The interference signal caused due to the light reflecting back from the reflective surfaces of the sample is coupled to a home-built spectrometer.

In the home-made spectrometer, light input to the spectrometer is first collimated and is then directed to diffraction grating (1200 lines/mm). A diffraction grating splits the light into its frequency components. The focusing lens is used to focus light on CCD camera. The spectrally

dispersed output of the spectrometer is captured by attached 12-bit line scan camera CCD records the amount of light that hits each pixel and converts to the voltage level. As the camera is 12 bit, each pixel in the camera can handle 4096 brightness units. The camera communicates with Ni 1428 camera link acquiring digital frames and stores them on system hard drive. The spectrometer can acquire 20 K spectra/sec with a resolution of 0.06 nm.

Such a robust and straightforward setup for the sample path optics would be to mount all the opto-mechanical components on a cage system, as shown in Figure 26 and Figure 27. Optical components are mounted on cage plates, and kinematic mirror mounts to enable the fine adjustment of collimated beam tip and tilt orientation with respect to the focusing lens.

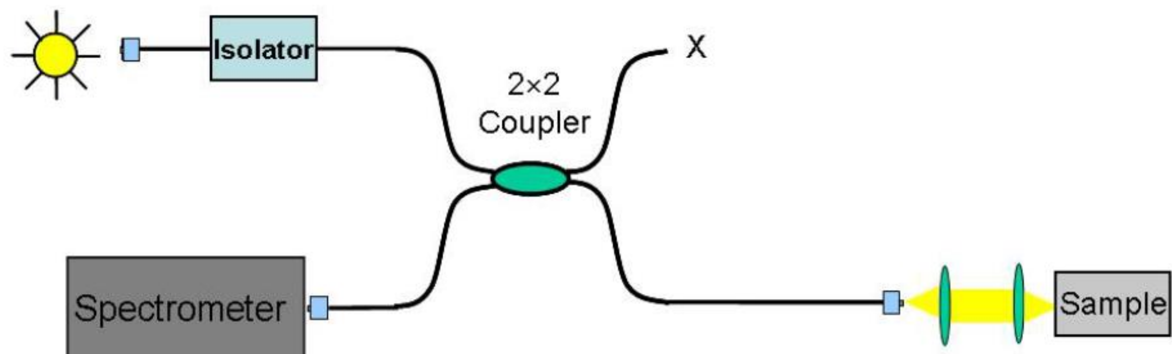

Figure 26 Setup of a fiber-based spectral domain phase sensitive interferometer

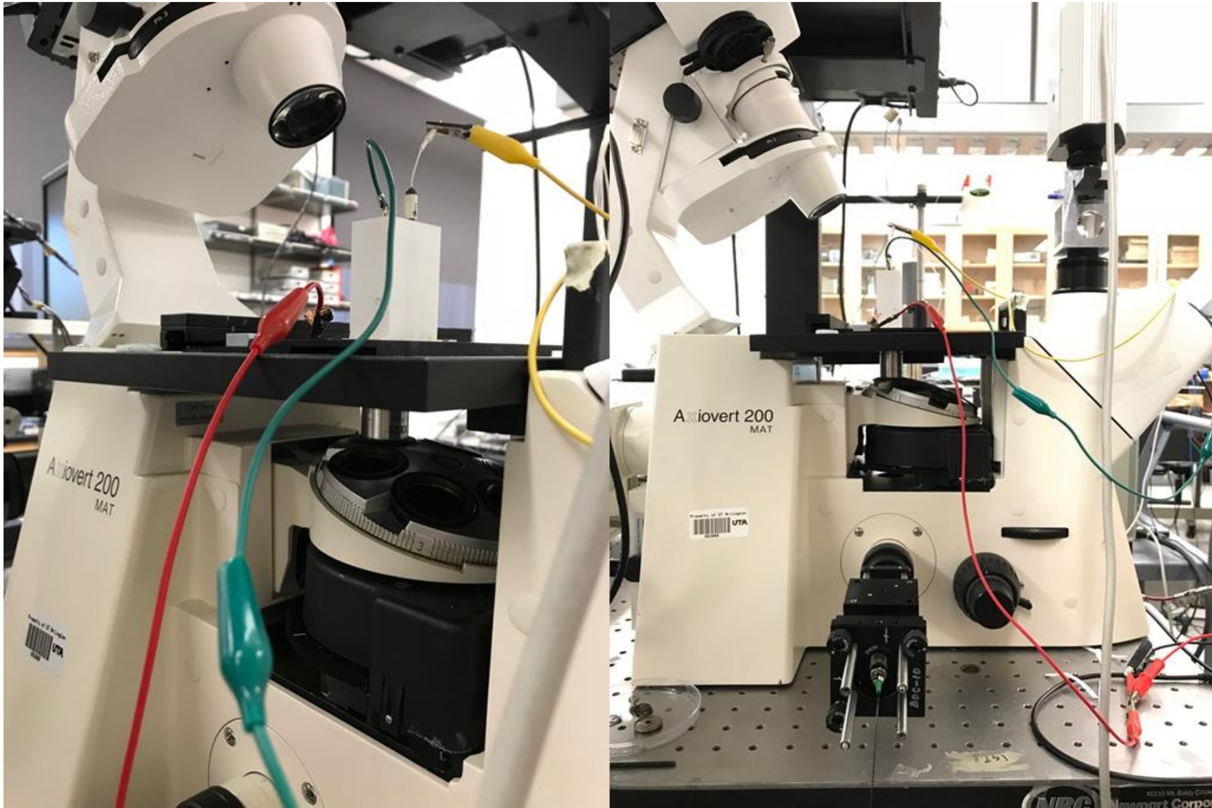

Figure 27 Photograph of the SD-PSI sample path configuration showing various components integrated together using a cage system.

Suitable sample geometry for SD-PSI measurement is any transparent substrate (glass or plastic) of suitable thickness. The thickness of the transparent substrate that can be used is only limited by the resolution of the spectrometer used in the setup. The spectral modulation frequency is proportional to the thickness of the substrate and the deposited layer. In the sample optical configuration shown in Figure 28, the light will reflect back onto the interferometer from the interface 1, interface 2, and interface 3. Spectral modulation of various frequencies will occur due to interference between light reflections of the ratio of the reflectivities of the two interfaces involved. Interference will also occur due to multiple reflections of light from the various interfaces by the modulation depth is far smaller than the primary interference signal, and the

modulation frequency will be a multiple of the primary modulation frequency. Each interference signal occurs at a fixed spatial frequency band that is proportional to the optical thickness of the interfaces involved and can be measured by Fourier transformation of the recorded spectral interference.

Figure 28 The optical configuration of the formation of Copper Monolayer

3.2 Copper Underpotential Deposition on Gold Electrodes

The UPD of Cu on Au(*h*,*k*,*l*) electrodes has been studied extensively over the past, using virtually all techniques available to surface electrochemists including pure electrochemical methods (voltammetry, chronocoulometry, chronoamperometry,ring-disk), in situ STM, AFM,X-ray techniques (surface scattering, SEXAFS/ XANES, and X-ray standing wave), EQCM and SHG, and ex-situ UHV techniques (LEED, AES, and RHEED). In addition to these investigations, theoretical models have been applied to Cu UPD on Au (111) electrodes, which, although initially were at

odds with experimental findings, were found to be consistent with them upon a reevaluation of experimental results, especially STM and AFM. All of these studies have provided a detailed knowledge, although still not complete, of these systems, especially for Cu UPD on Au (111) electrodes in sulfuric acid media. In fact, Cu UPD on Au (111) has been one of the most widely studied systems and is also a paramount example of the effects of anions and surface structure on UPD behavior as well as on surface electrochemistry.

3.2.1 Sulfuric acid media

The cyclic voltammogram of Cu UPD on Au (111) shows two well-defined and sharp pairs of peaks corresponding to two different adsorption/ desorption processes. The pair of peaks (deposition/stripping) at high underpotentials has a broad shoulder, whereas the deposition peak at low underpotentials splits in two on high-quality Au (111) single crystals. The peak currents for the deposition and stripping processes exhibit a marked sweep rate dependence, being proportional to the scan rate for values below 5 mV/s. However, at higher scan rates, the peak currents follow *half of the potential* dependence. This behavior is the result of very slow charge transfer dynamic processes with instantaneous nucleation and growth kinetics. The splitting of the second deposition peak is the result of two different nucleation processes, one taking place on surface defects and the other on well-ordered (111) terraces; thus, the dependence on the surface quality of the electrode is confirmed.

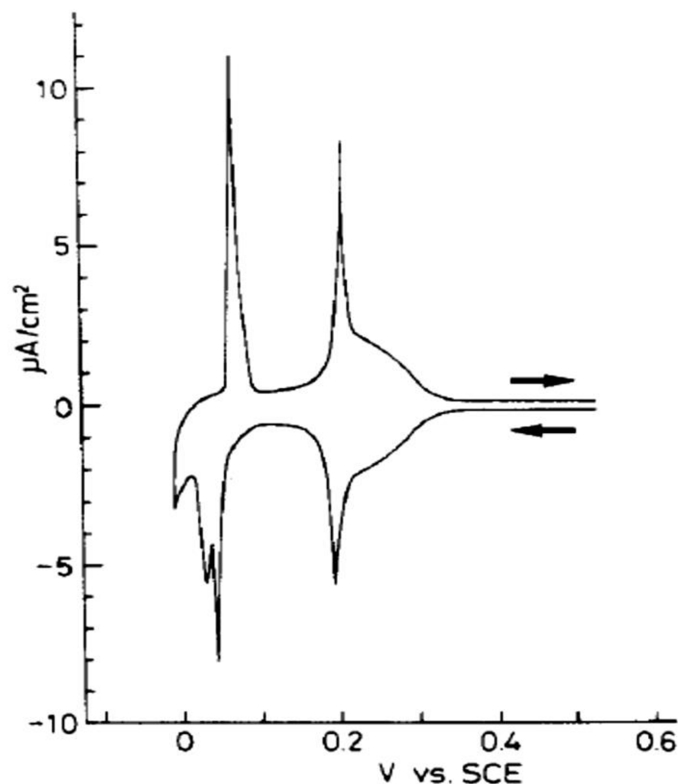

Figure 29 Cyclic voltammogram for a Au(111) electrode in 0.05 M H_2SO_4 + 1 mM $CuSO_4$. Scan rate: 1 mV/s. Copyright 1991 Elsevier Sequoia SA.[38]

Copper underpotential process on Au(111) have been reported for two different coulometric charge values : 460 and 350 C/cm^2. The difference between these values is likely the result of different measurement criteria since in arriving at the value of 350 a charge of zero was assigned for potential in the middle of the broad shoulder of the first peak. The addition of the charge that would correspond to the broad shoulder would give a charge value that is very close to 450. Theoretically, the value for the deposition of a fully discharged monolayer of copper would be 440. This indicates the out of the total charge for the copper UPD processes, about 2/3 corresponds to the first deposition peak.

Taking the electrochemical results as a point of view, a priori one would expect that two different copper ad-structures would exist, one after the first deposition peak with an intermediate copper coverage of 2/3 and one after the second deposition peak with a coverage close to 1. Kolb and co-workers have done the investigation of the Cu adlayers. The result of RHEED and LEED suggested two different structures that were interpreted as a honeycomb structure after the first deposition peak. Also, AES measurements pointed that (bi)sulfate adsorption on the Cu adlayers was stronger than that on the bare Au (111) electrode, in agreement with radiotracer and FTIR measurements on Cu UPD on poly oriented gold.

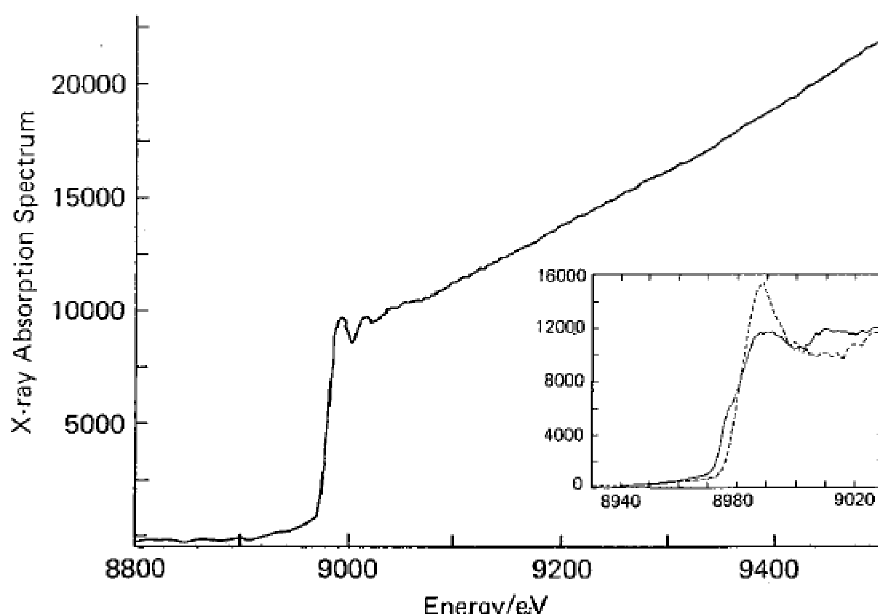

Figure 30 X-ray absorption spectra around the Cu KR edge for CU UPD on Au (111) at +0.13 V vs. Ag/AgCl. Copyright 1988 American Chemical Society.[38]

The first in-situ measurements on this system were done by SEXAFS. This structure was later observed by STM and AFM, SEXAFS measurements provided an accurate determination of the Cu-Cu distance in this structure. The distance is closed as the Au-Au distance in the (111) direction

(2.92 Å), implying that the Cu adlayer is commensurate with the Au (111) substrate. In this structure, Cu adatoms probably sit on 3-fold hollow sites, as derived from the polarization dependence of the SEXAFS or by estimating the number of gold nearest neighbors. SEXAFS spectra also indicate the existence of oxygen (likely arising) from bi-sulfate on top of the Cu adlayer. The amount of bi-sulfate co-adsorbed on the Cu adlayer has been measured with EQCM and chronocoulometry. Results from previous techniques indicate that the coverage of bi-sulfate is the same as the maximum obtained for a clean Au (111) electrode although the EQCM studies obtained values for clean Au(111) electrodes are significantly higher than those obtained with chronocoulometry, STM ,or radiotracer measurements. Chronocoulometric results also suggested that the Cu adlayer was discharged entirely, whereas XANES indicated that the oxidation state of copper was approximately 1. These two apparently contradictory results are probably a consequence of the formation of an Au-Cu polar bond (or a surface dipole) in which the Cu atom has a charge deficiency.

The determination of the structure after the first UPD peak was more difficult and was controversial. The first and AFM images showed a structure (Figure 31), in which the maxima were interpreted as Cu adatoms. On the basis of this structure, the total Cu coverage was 0.33. In some cases, this structure changed with time to form a different structure caused by the existence of chloride contamination from the reference electrode.

Theoretical calculations to predict the formation of a honeycomb structure close to that found in UHV. They found that the Cu adlayer, at intermediate coverage values, has a honeycomb structure in which potential at 0.67 and with (bi)sulfate anions occupying the centers of the honeycomb as shown in Figure 32 in agreement with the coverage values found with chronocoulometry and

EQCM. This result is implying the scanning probe techniques (STM, AFM) were not imaging the Cu adatoms but the (bi)sulfate anions that occupied the centers of the honeycomb and protruded well above the Cu plane. In the case for the Cu structure, XANES clearly suggested that the oxidation state of the Cu adatoms after the first UPD peak is approximately +1 probably as a consequence of a polar bond or surface dipoles close to the results obtained with ring-disk electrodes. For this structure, it has been proposed that the Cu adatoms occupy on top positions.

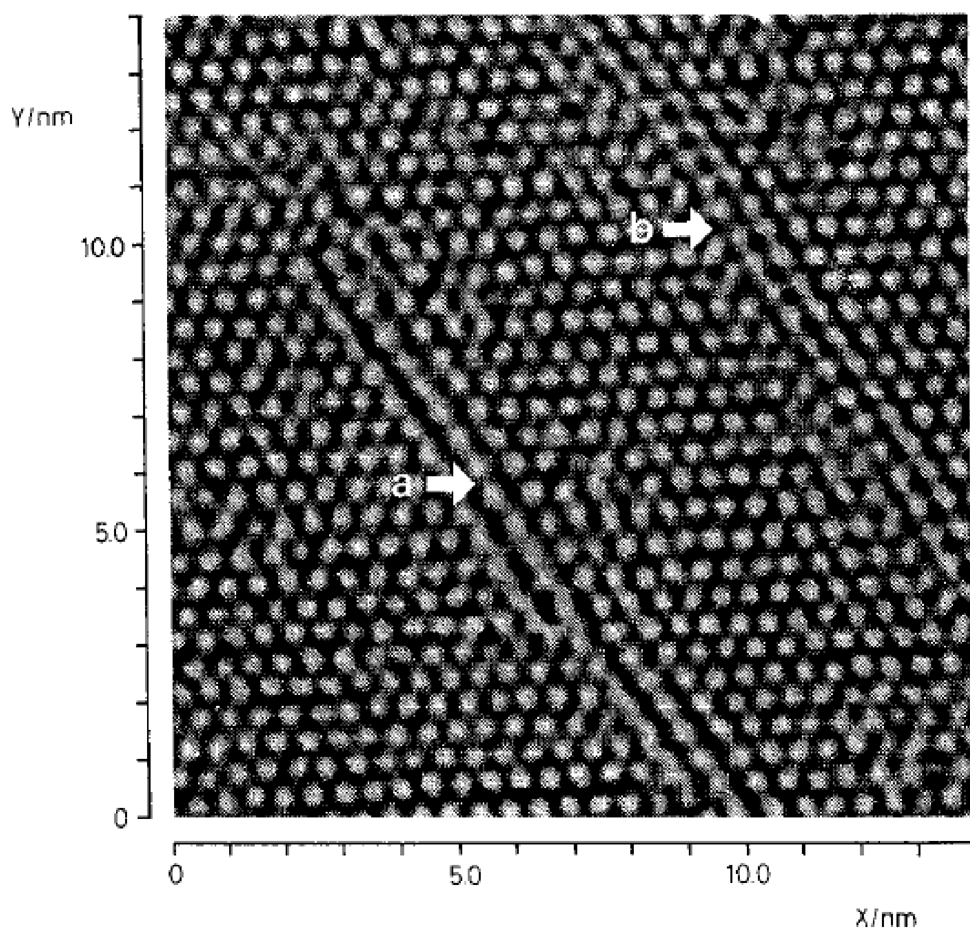

Figure 31 STM image of the structure for Cu UPD on Au(111) at +0.15 V vs. SCE showing two different phase boundaries. Copyright 1991 Elsevier Sequoia SA.[38]

Finally, the features in the cyclic voltammogram could be explained if the structure of the adlayer

was resolved. In the beginning, the first Cu adatoms are randomly deposited on the electrode surface, together with some (bi)sulfate anions. It means that Cu adatoms are quite mobile on the electrode surface. This part of the process corresponds to the broad shoulder prior to the first UPD peak. At a sulfate coverage on the surface, the adlayer undergoes a first-order phase transition to form a honeycomb structure due to the first UPD peak. Eventually, the adlayer transforms to a Cu structure with (bi)sulfate adsorbed on top of the copper adlayer.

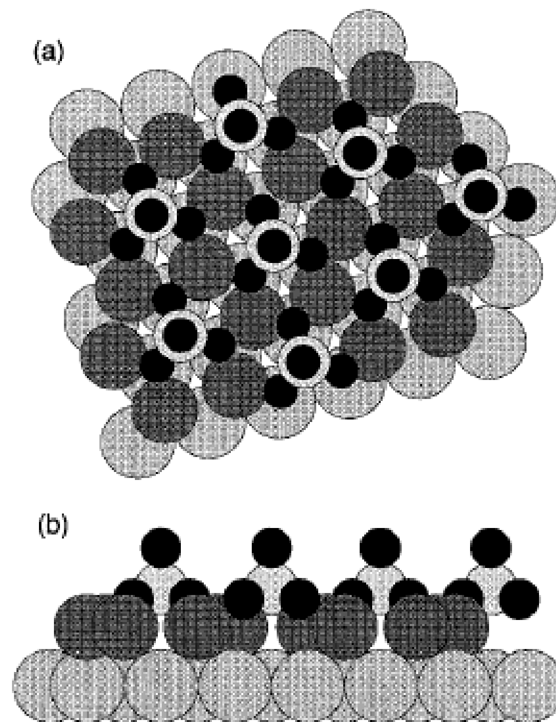

Figure 32 Interfacial structure of the Cu UPD on Au(111) after the first UPD peak: (a) top view; (b) side view. Copyright 1995 The American Physical Society.[38]

3.2.2 Influence of Anions

Copper UPD on Au (111) in chloride-containing solutions exemplify the effects of anions in UPD processes. STM measurements in sulfuric acid media indicate how small amounts of chloride

induced the transformation of the Copper structure. The observed transformation took place even when the bisulfate concentration was much higher than the chloride concentration, meaning the high affinity of that chloride anions has for copper. This behavior is reflected in the voltammetric profile in the presence of chloride as shown in Figure 33. The voltammogram shows two pairs of peaks, as in the case of sulfuric acid, but the pair at high underpotentials is reversible and appears at potentials that are more positive than in sulfuric acid. The second pair of peaks almost overlaps with bulk Cu deposition.

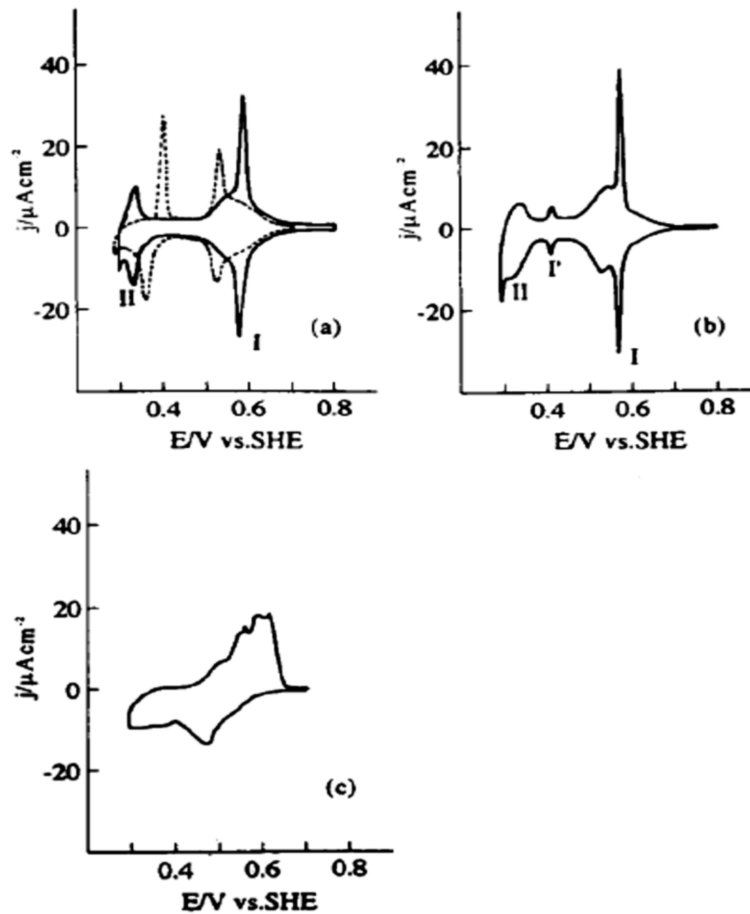

Figure 33 Voltammetric profiles of Cu UPD on Au(111): (a) 0.05 M H_2SO_4 + 1 mM $CuSO_4$ + 0.1 mM KCl; (b) 0.05 MH_2SO_4 + 1 mM $CuSO_4$ + 0.1 mM KBr; (c) 0.05 M H_2SO_4 + 1 mM $CuSO_4$ + 0.1 mM KI. The broken curve on (a) is for 0.05 M H_2SO_4 + 1 mM $CuSO_4$, given for comparison. Scan rate: 5 mV/s. © 1994 Elsevier Science SA.[38]

After the first deposition peak, STM measurements showed the deformation of a Copper structure. However, this structure can be another one which was in transition phase by careful measurements as shown in Figure 34. Ex-situ LEED analysis also indicated the presence of a distorted structure. Nonetheless, when the potential was scanned in the negative direction, there were more unstable structures. Chronocoulometric results indicated that the ratio of copper to chloride in the adlayer for these structures was equal to 1.24. Therefore, a bilayer structure was proposed in which chloride is adsorbed on the copper and where the Cu and the chloride coverage are equal to 0.62. SEXAFS measurements indicated that the copper adatoms are packed in registry with the top layer of chloride ions as shown in Figure 35. The distances in the proposed structure are quite similar to those found in solid CuCl.

As the potentials reached the second peak, the structure is still showing, and STM images represented a long-range corrugation. It has been proposed that chloride anions are desorbed at these potentials. However, chronocoulometry indicated that the chloride surface concentration remained stable over the entire potential range of Cu UPD for chloride concentrations above 10^{-4} M.

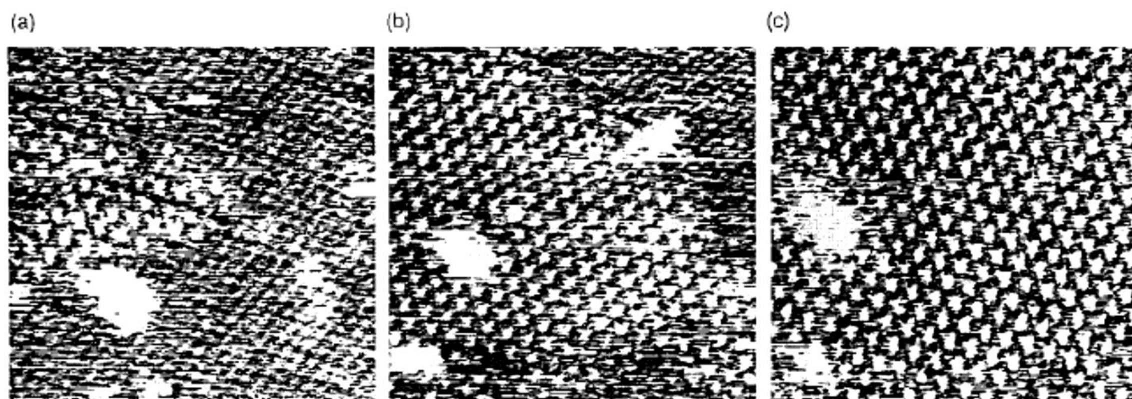

Figure 34 Series of three STM images of Cu UPD on Au (111) in 0.1 M $HClO_4$ + 0.01 M Cu $(ClO_4)_2$ solution containing trace amounts of Cl^- ions recorded over the same area at time intervals of 25 s. Upon a change of the potential from +0.3 to +0.13 V vs. SCE at the beginning of image (a) the transformation of the one structure into the other structure via an island growth of the phase is observed. Copyright 1995 Elsevier Science BV.[38]

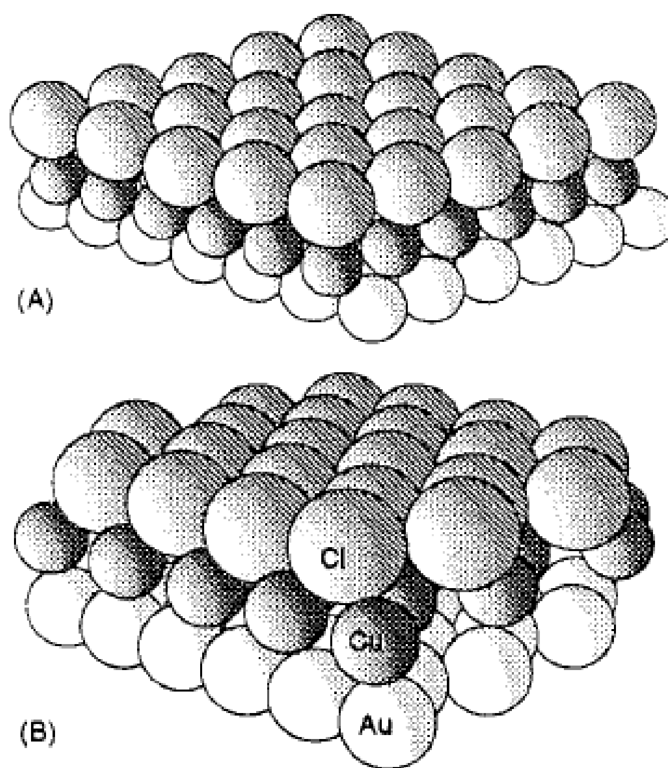

Figure 35 Model for the bilayer structure formed by the copper and chloride ions at the Au (111) surface: (A) copper adsorbed in registry with the Au (111) substrate; (B) copper adsorbed in registry with the top layer of chloride ions. Reproduced. Copyright 1995 Elsevier Science Ltd.[38]

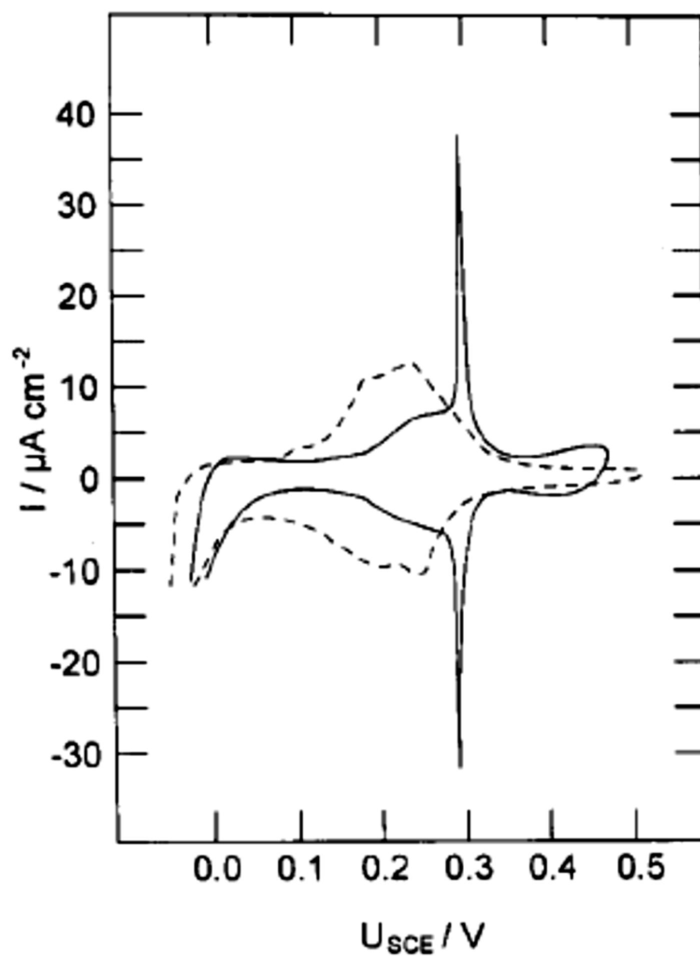

Figure 36 Cyclic voltammogram for a Au (100) electrode in 0.01 M H_2SO_4 + 1 mM $CuSO_4$ without (dashed line) and with the addition of 0.1 mM HCl. Scan rate: 2 mV/s. Copyright 1995 The American Physical Society.[38]

Once the chloride concentrations below 10^{-5}M, a structure is observed at potentials below +0.14 V vs. SCE as shown in Figure 36. In the cyclic voltammogram, an additional peak at this potential also observed. For this structure, the Cu coverage is 0.75, and the chloride concentration is 0.25, again in agreement with the chronocoulometric results. On the other side, in perchloric acid media, the situation is quite similar to that found at low chloride concentrations in acid media due to perchlorate solutions almost always have a residual chloride concentration around 10^{-6} M. Thus, two structures are observed: a structure at high underpotentials and the structure at

potentials lower than +0.14 V vs SCE.

When bromide or iodide involved, the behavior is very close to that found in the presence of chloride with a bilayer structure predicted. For bromide solutions, STM measurements identified two different structures at high and low underpotentials. However, these results are not consistent with chronocoulometric results and with recent X-ray scattering studies. In these studies, an ordered hexagonal bromide adlayer is formed at the onset of copper deposition and undergoes a phase transition to form a corresponding structure at the peak at +0.32 V vs. Ag/AgCl. This bromide adlayer remains stable until the bulk deposition of copper begins. Copper is deposited between the gold surface and the bromide layer. With the addition of iodide, the surface structure is another one. Generally, the trend for all the Cu-halide systems, the structures of these adlayers is governed by the halide-halide and the Cu-halide interactions in contrast to the Cu-(bi)sulfate adlayers in which the Cu-Au interaction is dominant. However, clearly, all interactions contribute to the UPD processes.

3.2.3 Cu UPD on different single-crystalline Au electrodes

Cu UPD occurs in a relatively broad peak on Au (100) electrodes and in sulfuric acid media. At low bisulfate concentrations (<1 mM), the deposition peak splits into two. The result from STM and AFM demonstrated that the surface structure, after the deposition peak, is a pseudomorphic structure in which the Cu atoms occupy the 4-fold hollow sites which is the same with XSW. However, SEXAFS measurements suggested a different picture of the adlayer at full coverage. In the model proposed from experimental data, the Cu-Cu distance is shorter than the Au-Au

distance in the unreconstructed Au(100) surface, and the Cu adatoms occupy top sites, implying that the gold layer is rearranged or reconstructed. As on Au(111) electrodes, the Cu oxidation state is close to 1.

The existence of intermediate coverage structures in sulfuric acid is doubtful. The quasi-hexagonal structures identified by STM were probably caused by chloride contamination from the reference electrode. Another structure has been found at potentials within the broad peak and is quite similar to that found in chloride media. Meanwhile, the voltammetric profile for Cu UPD on Au(100) in sulfuric acid is different from those previously reported and was similar to the condition for the presence of chloride.

Previously, the presence of chloride in the solution changes the behavior of the Cu UPD system. The voltammetric profile shows a pair of sharp peaks followed by a broad shoulder. After the sharp peak, the Cu adopts a structure, which is a distorted hexagonal structure and the Cu-Cu distance in the adlayer ranges between 3.6 and 4.1Å close to the distance found in Au(111) electrodes. This result indicates that an adlayer structure is determined mainly by Cu-Cl interactions, and a bilayer is also probably formed.

As for Au(110) electrodes, two different structures have been found in sulfuric acid media and an in chloride media. The model for the structure is based on a CuCl(111) bilayer, in which, as in the previous cases, the adlayer structure is mainly determined by the Cu-Cl interactions. In addition, a possible Cu-Au alloy formation was also discovered.

The electrodeposition of metals onto organothiol-coated electrodes has been the subject of study by various groups. It has been found that alkanethiol self-assembled monolayers (SAMs) prepared

on predeposited Ag monolayers on the gold substrate were more stable to thermal desorption. Also, other people examined Cu and Ag underpotential deposition (UPD) on Au (111)-propanethiol and concluded that the metal layer was deposited between the Au substrate and the SAM. More recently, it reported a more extensive range of metal UPD. For alkyl chains shorter than eight carbons, UPD was found to occur; octane thiol films were found to allow Ag UPD in the form of islands on which the SAM molecules adsorbed, but longer chains inhibited the UPD process. In many cases, the SAM was more stable to reductive desorption on the UPD metal layer than the Au (111) substrate surface. More analytical directed studies of metal deposition at SAMs have been reported by Heineman and co-workers. They were interested in the development of SAMs for stripping voltammetry applications. Copper deposition at SAMs has been studied by various methods including voltammetry and scanning tunneling microscopy. Using Cu deposition on ethanethiol-coated Au(111) as a model system, Kolb and coworkers studied both bulk deposition and UPD. Cu deposition at the SAM-Au interface was the conclusion from their work. Charged monolayer systems have been of interest in recent years, and have been the subject of various characterizations as well as for the provision of electrode selectivity or biomacromolecule immobilization.

3.2.4 Cu UPD on polycrystalline Au surface

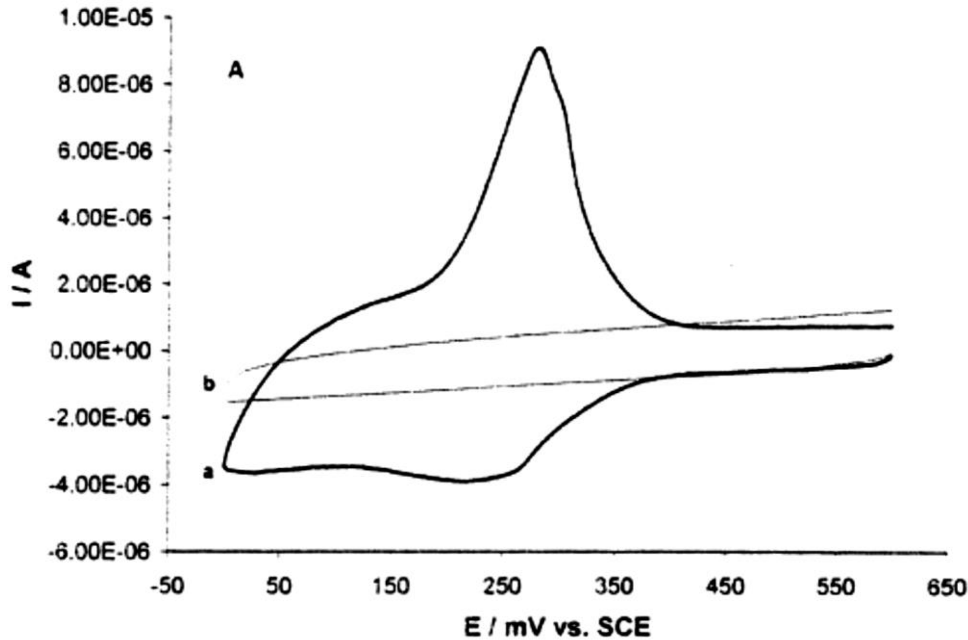

Figure 37 Underpotential CV in the presence (a) and absence (b) of Cu^{2+} (1mM) in H_2SO_4 (0.1 M) at bare gold. Sweep rate: 100mV/s.[63]

The CV of CU^{2+} at a clean polycrystalline gold electrode in 0.1M H_2SO_4 in the UPD region is shown in Figure 37. This experiment restricted investigations into the potential region >ca.0.00V (vs. SCE) as this was positive of the Nernst potential for bulk copper deposition. The behavior observed was typical for that observed at polycrystalline gold. Broad reduction and oxidation peaks were observed for the deposition and stripping of the Cu monolayer. The charge densities associated with these peaks were $3.16610*10^{-4}Ccm^{-2}$ (cathodic) and $3.19610*10^{-4}Ccm^{-2}$ (anodic) which in both cases was approximately $1.6610*10^{-9}$ mol cm^{-2} surface coverage. This corresponded to a submonolayer of the copper metal ($2.61*10-^{9}$ mol cm^{-2} is the monolayer coverage for a metal layer).

3.3 Copper UPD Experiment processing

In order to investigate the Phase-Sensitive Interferometry (PSI) has the ability to determine the monolayer measurement, CV becomes the best method to test this method. UPD of Cu on the Au electrode has been proved to form a monolayer on the surface. Therefore, we combine the advanced optical instrument, PSI with the traditional electrochemical cell to examine UPD of Cu on polycrystalline Au surface. This section will be focused on the instrumentation and the analyzation of the phase result, pointing out the monolayer detection is possibly achieved by the PSI.

3.3.1 Equipment set up and experimental procedure

We conducted in situ optical monitoring of the UPD of Cu on a transparent gold-coated coverslips glass in sulfate-containing electrolytes. Underpotential deposition of copper was performed inside a typical three-electrode electrodeposition cell using Cyclic voltammetry technique, which provides the current peaks and measures the total charge transferred during the adsorption/desorption processes.

The working electrode is a 10 nm Au layer with 5 nm Cr adhesion layer on mica, quartz or glass coverslip substrate. Metal films were deposited using a thermal evaporator. The counter electrode is a platinum mesh, and the reference electrode is Ag/AgCl (Sat KCl) electrode with a potential of 0.197 V versus N.H.E. All potentials are reported vs. the Ag/AgCl reference electrode.

Copper UPD was carried out in aqueous solutions of 1 mM $CuSO_4$ in 0.1 M H_2SO_4. The electrolyte was deaerated with nitrogen gas for 30 minutes before use. During the experiment the solution

is unstirred. The working electrode is rinsed with purified water and then glued directly to the cell by epoxy followed by 5 minutes curing. Cyclic voltammograms were obtained using a potentiostat.

In CV, the potential was scanned from 0.60V to 0.15V. The cyclic voltammogram shows two distinct peaks corresponding to adsorption and desorption processes. This result demonstrates that gold-coated glass substrate can be adopted as the working electrode for studying a monolayer formation of copper using cyclic voltammetry.

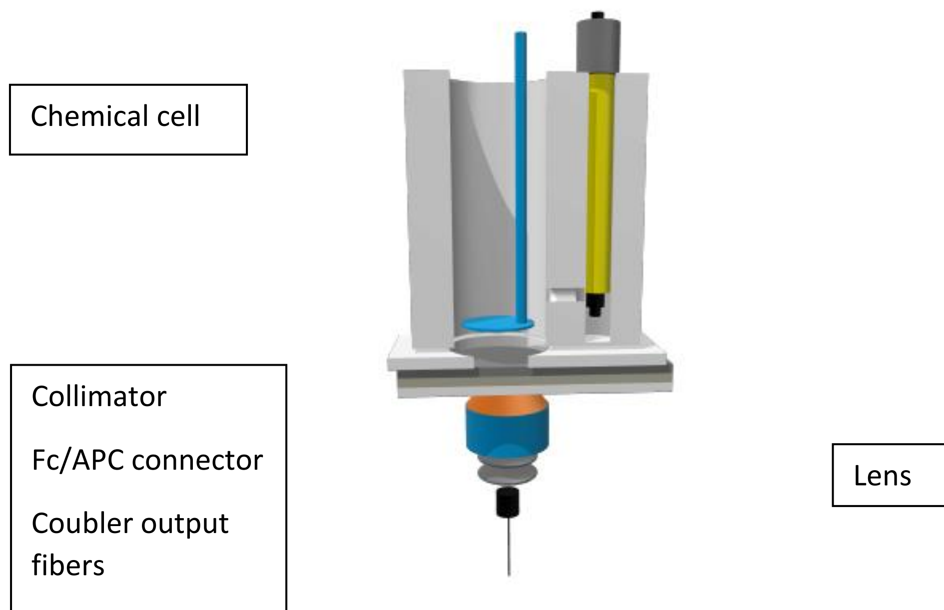

Figure 38 Setup for electrochemical study for interferometry

3.3. UPD CV on Different Substrates 2

In the setup for combining electrochemical cell with interferometer, light passes through working electrode, and the light reflected from bottom (substrate/air interface) and top (substrate/electrolyte) surfaces constructs interference fringe pattern, which varies slightly when

the substrate/electrolyte interface (the top surface) experience any change (deposition, electrolyte change, etc.) Interference through a transparent substrate with a thickness of about 200 µm generates about 16 fringes with the light of a wavelength of ~800nm, which provides an optimal fringe pattern for Fourier analysis. For UPD of Cu, the working electrode must be an Au surface, and at the same time, such Au should not completely block the light (light needs to reach to the deposited Cu and electrolyte interface). So, the working electrode would be a thin layer of Au on a transparent substrate, and the thickness of the Au layer should be thin enough to allow light to pass through.

Ultra-thin film Au working electrode possesses different electrochemical properties compared to traditional Au electrode which usually is composed of a thick (> 100nm) Au film, and UPD of Cu on ultra-thin film Au has not been reported. Therefore, the first task we faced was to achieve UPD of Cu on ultra-thin film Au. It is also known as the microstructure (grain size and texture) of Au thin film, especially for ultra-thin films, and in turn, their electrochemical properties, are heavily influenced by the underlying substrate. Since CV experiments are the easiest way to tell if UPD has happened, we conducted CV experiments on different substrates coated a 10-nm layer of Au with an adhesive layer of 5-nm Cr: Si, mica, quartz, and glass. The results are shown in Figure 39. Si wafer (single crystal) substrate provides more evident redox reaction peaks. But surprisingly, CV on glass (amorphous) substrate is closer to the CV curve on Si than single crystal mica and quartz substrates. We speculate that such similarity comes from native silicon oxide on the Si wafer surface, and it seems that such amorphous underlying substrate favorably affects the microstructure of Au film for Cu UPD.

In this project, we choose #2 glass coverslip, which is ~200 µm thick, as the underlying substrate. 10 nm of Au film with 5-nm Cr film was deposited to such coverslips using thermal evaporation.

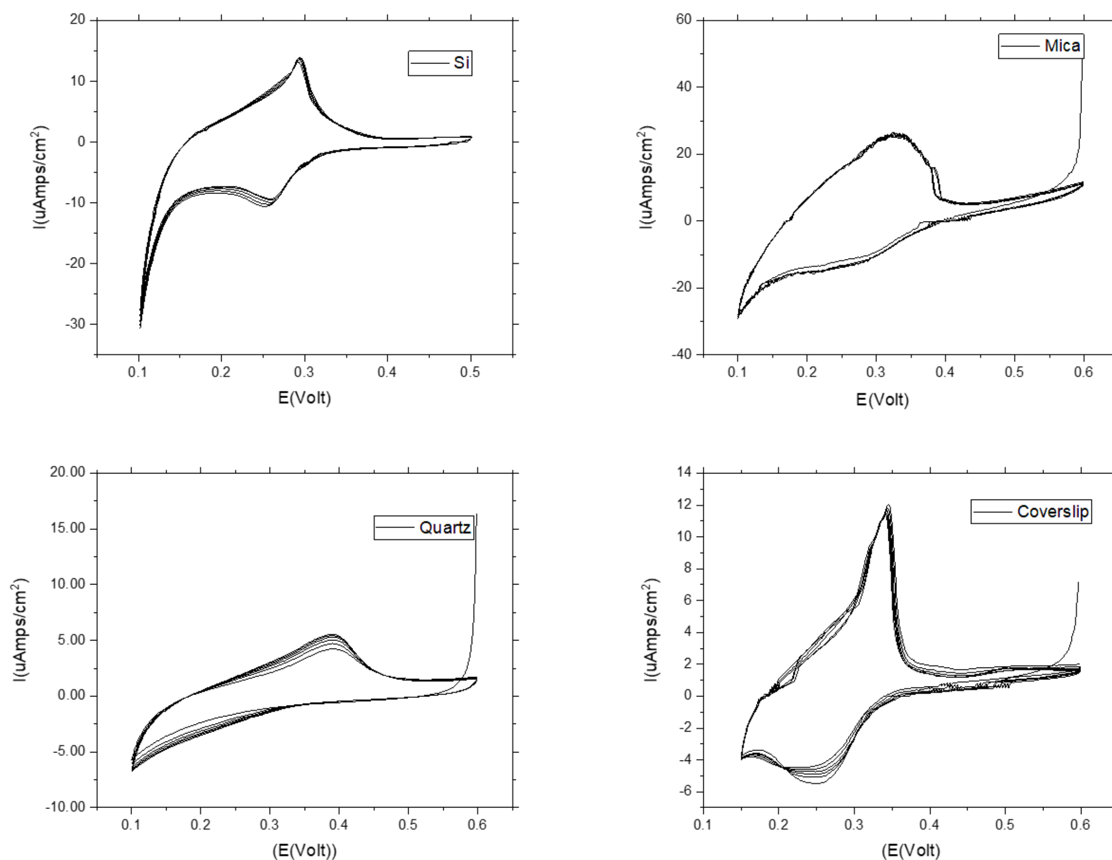

Figure 39 Different Substrate for Copper UPD process.

3.3.3 Real-time Probing CV of Cu UPD

The CV curves show that the current peaks corresponding to the deposition and stripping processes exhibit a marked sweep rate dependence. as shown in Figure 40, the current density of cyclic voltammetry increased with the sweep rate.

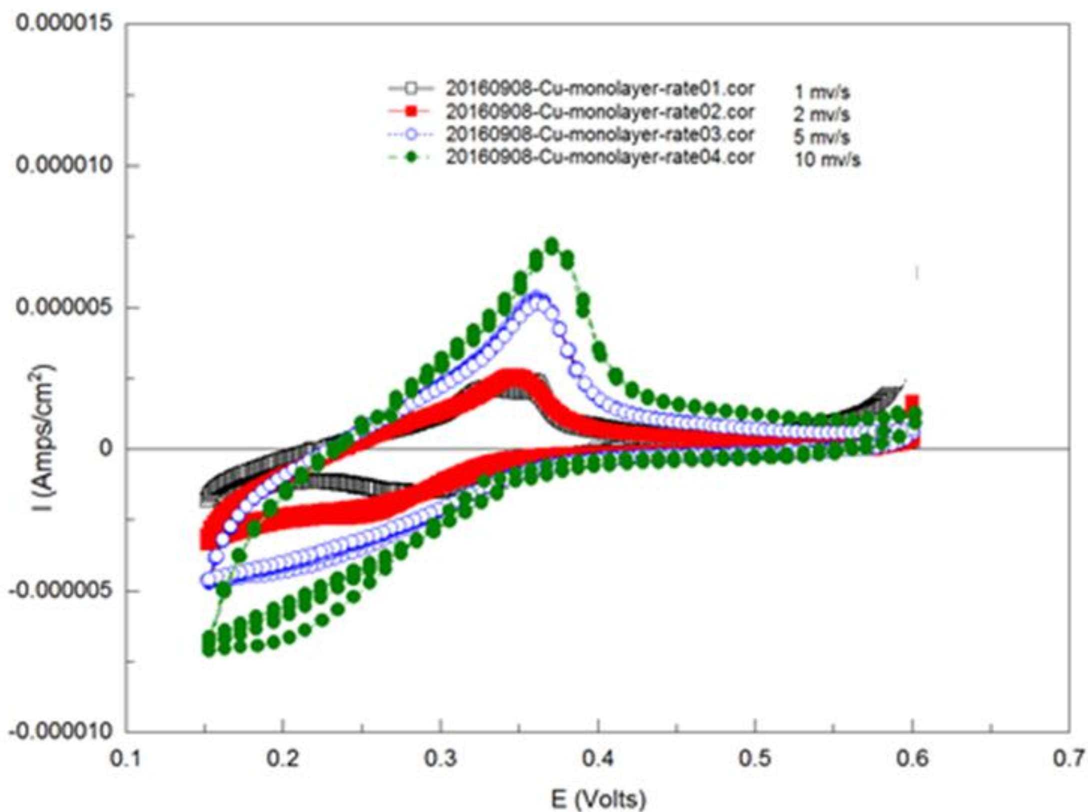

Figure 40 Experimental cyclic voltammetry current densities for a gold-coated electrode in 1mM CuSO4 + 0.1mM H2SO4 at 1, 2 , 5, and 10 mV/s, respectively

This is a typical cyclic voltammogram (CV) of UPD on polycrystalline Au electrodes taken in 1 mM CuSO4/ 0.1M H_2SO_4. We have limited investigations into the potential region >0.15 V (vs. Ag/AgCl) as this was positive of the Nernst equation for bulk copper deposition. It is apparent that the total current increases with increasing scan rate. The result can be rationalized by considering the size of the diffusion layer and the time taken to record the scan. The linear sweep voltammogram will take longer to record as the scan rate is decreased. As a result, the size of the diffusion layer above the electrode surface will be different depending upon the voltage scan rate used. In a slow scan, the diffusion layer will grow much further from the electrode compared to a fast scan. Consequently, the flux to the electrode surface is considerably smaller at slow scan rates than it

is at faster rates. Because the current is proportional to the flux towards the electrode, the magnitude of the current will be lower at slow scan rates and higher at high rates. This emphasizes a critical point when examining LSV or cyclic voltammograms, even if there is no time axis on the graph, the voltage scan rate do strongly affect the behavior. Besides, a final point to note from the Figure is the position of the current maximum; it is clear that the peak occurs at the same voltage and this is a characteristic of electrode reactions which have rapid electron transfer kinetics. These rapid processes are often referred to as reversible electron transfer reactions. Cyclic voltammograms can be understood as a process composed of two LSV. When the scan is reversed, we merely move back through the equilibrium positions gradually converting electrolysis product. The current flow is now from the solution species back to the electrode and so occurs in the opposite sense to the forward step, but otherwise, the behavior can be explained identically.

Ideally, the deposition thickness can be calculated from the equation

$$\delta = \frac{W}{\rho A} = \frac{M}{nF\rho A}\int Idt$$

Where ρ is the density of metal (g/cm^3), F is Faraday constant $9.65*10^4$ $Cmol^{-1}$, Idt is the total charge applied, n is number of electrons transferred, and A is the area of the deposition Here, we put the value to do simulation for Cu deposition of ρ is 8.96 g/cm^3, A is 1.776 cm^2, M_w is 63.54. From the equation, we can deduce the amount of charge needed to form a monolayer on the gold substrate. If the radius of Cu atom is taken as 0.128nm, and the monolayer thickness as 0.256nm, the charge to form Cu monolayer is calculated as 1.237×10^{-3} C. From the CV curve, the charge calculated by integration is 1.2612×10^{-3} C for 5mv/s, and 1.21×10^{-3} C for 2mv/s close to

the monolayer charge given as shown F inigure 41.

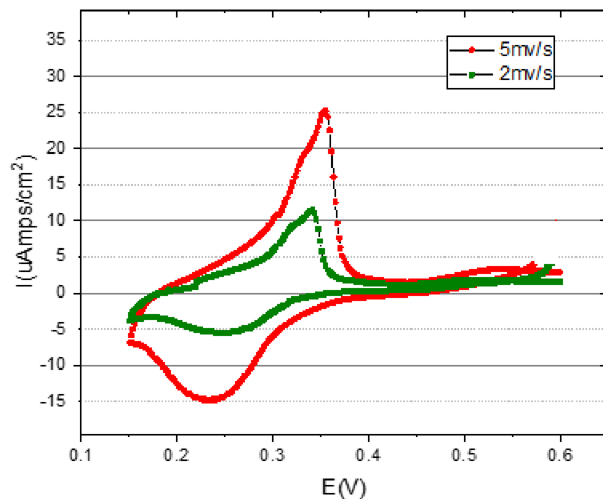

Figure 41 Underpotential CV in the Cu^{2+}(1mM) in H_2SO_4 (0.1M) at bare gold electrodes. Sweep rate:5mVs^{-1} and 2mVs^{-1}

Also, the cathodic process at potentials larger than 0.1 V is attributed to a Cu UPD process since in the absence of Cu $^{2+}$ in solutions; a charging current is acquired. The peak in the oxidation process shifts to more negative value compared to 5mv scan speed. The overall current for the reduction process is diminished. Also, it can be noted that the current density value increase as the scan rate is enhancing.

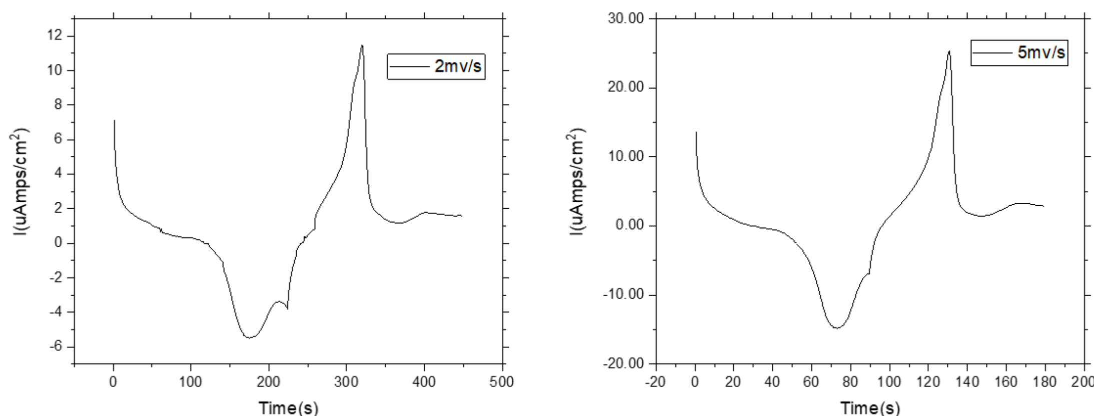

Figure 42 Different unit in the Cu2+(1mM) in H2SO4 (0.1M) at bare gold electrodes. Sweep rate:5mVs-1 and 2mVs^{-1}

Another method to affirm monolayer formation on the gold electrode is counting the atoms arranged on top of it. Ideally, the number of atoms should be 3.45×10^{15} atoms closed packed sit on the surface in the area of 1.776 cm^2. Theoretically, a 1 C charge can generate 6.24×10^{18} Cu metal atoms with one Cu ion taking 2 electrons to get reduced on the surface. Then, according to the calculated charge from the integration of CV curves, the amount of atoms number is 3.98×10^{15} and 3.78×10^{15} on 5mv/s and 2mv/s, respectively. Both of the value suggests the number of atoms is enough to form a monolayer on the gold electrode surface.

For interferometer measurements, the spectral modulation frequency is proportional to the thickness of the substrate and the deposited layer. As shown in Figure 43, the light will reflect back onto the interferometer from the interface 1, interface 2, and interface 3. Interference will occur because of multiple reflections of light from the various interfaces, and the modulation frequency will be a multiple of the primary modulation frequency. Each interference signal occurs at a fixed spatial frequency band that is proportional to the optical thickness of the interfaces

involved and can be measured by Fourier transformation of the recorded spectral interference.

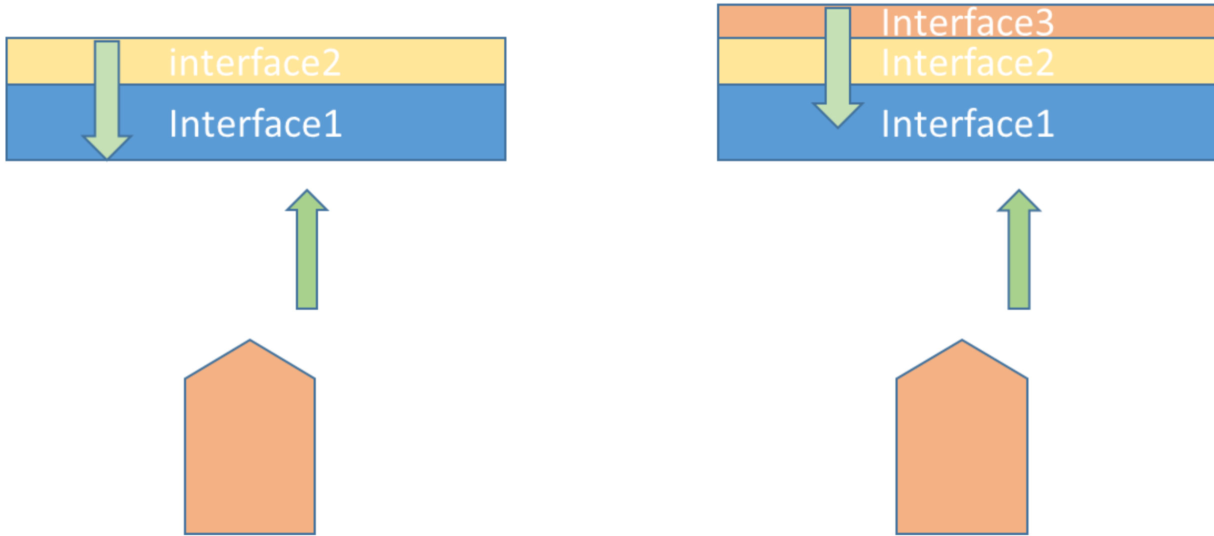

Figure 43 the optical configuration of the formation of Cu monolayer.

In the case of monolayer formation study, interface 1 and interface 2 do not change during UPD CV measurements, but interface 3 changes when Cu layer deposits on the Au surface. Such change will cause a shift in phase of the multiplexed interference signal, i.e., the interference patterns will exhibit a phase shift, and it reveals monolayer formation kinetics.

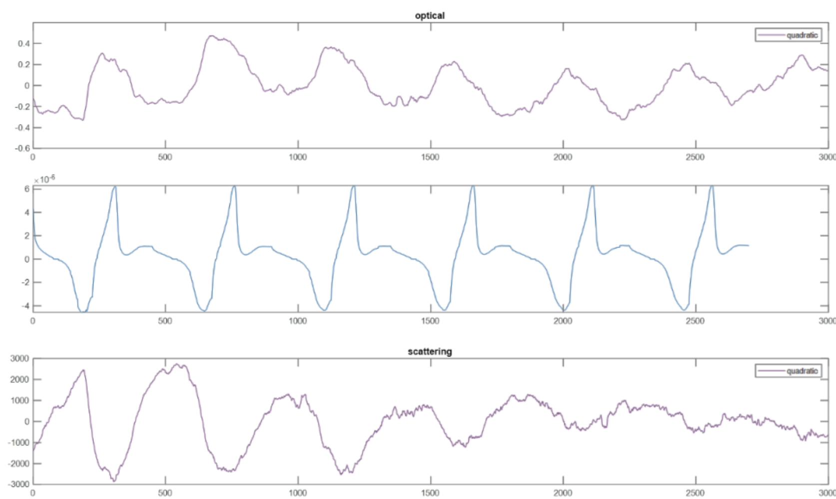

Figure 44 Phase result corresponding Current at CV proceeding experiment.

Figure 44 shows the typical recorded optical length change during CV measurement.

From the Equation

$$\Delta\varphi = tan^{-1}\left\{\frac{Im\ F(S(k))}{Re\ F(S(k))}\right\} = \frac{4\pi\Delta p}{\lambda_0}$$

The change of phase is due to the variation in the optical path length, leading to the natural increase in thickness caused by a monolayer of the copper formation. Each up and down cycle in optical path length change is corresponding to the cycle in CV result (potential versus time), clearly indicating the ability of PSI to detect monolayer Cu deposition and stripping.

We conducted the experiments with different scan rates and repeated the experiments with the same conditions many times. Figures are shown in Appendix A. These results show that SDPSI is a reliable tool to detect monolayer formation in UPD electrodeposition.

3.3.4 Optical properties of monolayer Cu UPD deposited on Au surface

The interference signal not only provides direct evidence about the monolayer formation but also provides a measure of optical properties of monolayer Cu. The optical path length change, OPL, due to UPD of Cu, is about 0.5 nm. We know that OPL= n × 2 × d, where n is the refractive index, and d is the thickness. Because light goes through the film twice (incident and reflected from the top interface), there is a factor of 2 in this equation.

When we take Cu thickness as the diameter of Cu atom, which is 0.256 nm, n calculated from above equation will be close to 1, which is far away from the measured bulk Cu refractive index (for light with 800 nm wavelength), 0.26. For ultra-thin films (<20 nm), values of n have a thickness dependence, and usually, increase as thicknesses decrease. Above 20 nm, refractive index

reaches to the bulk value. (See optical properties of Cu and AU in Appendix). However, such substantial increase, about 5 times larger than the bulk material, cannot be explained by this mechanism.

This significant discrepancy results from several reasons. It has been shown that bisulfate ions bind to Cu atoms, but not to Au atoms. So, during UPD of Cu, the Au/electrolyte interface is changing to Cu/bisulfate ions/electrolyte. The optical path length change includes the additional difference between the refractive index change between the bisulfate ion layer and electrolyte. This is also shown in reflection data from the interferometer, whereas OPL increases, reflection substantially decreases. Reflection is the direct measure of the top interface. Since Cu has a similar refractive index for 800 nm light to Au, when a monolayer of Cu deposited on Au surface, the top interface should not change much. i.e., if considering only the effect of a monolayer of Cu on the interface, such massive change of reflection are not expected. Therefore, this substantial change of reflection can only be explained by considering bisulfate ion accumulation on the interface. Considering the above-mentioned argument, the results we got become reasonable.

4. Atomic processes in the pre-deposition and early deposition stage of general electrodeposition processes

With the success of probing monolayer electrodeposition using SDSPI, we further explore using SDSPI to re-examine Cu electrodeposition processes, particularly at the very beginning of electrodeposition. Cu electrodeposition was conducted in pure acidic copper sulfate solutions with different Cu ion concentrations and applied potentials.

4.1 Background information

4.1.1 Copper water chemistry

Possible species in the copper-water system were first examined by constructing the equilibrium $E_{Cu/Cu^{2+}}$-pH diagram of copper in water, as given in Figure. 45 (a) for room temperature. According to the $E_{Cu/Cu^{2+}}$-pH diagram, the cupric ion predominance area is confined to a narrow region between pH 0 and 4.2 and above the solution potential of -20 mV. The solubility-pH diagram, Figure 45(b), was constructed to determine the equilibrium concentration of cupric ions in the

entire pH range.

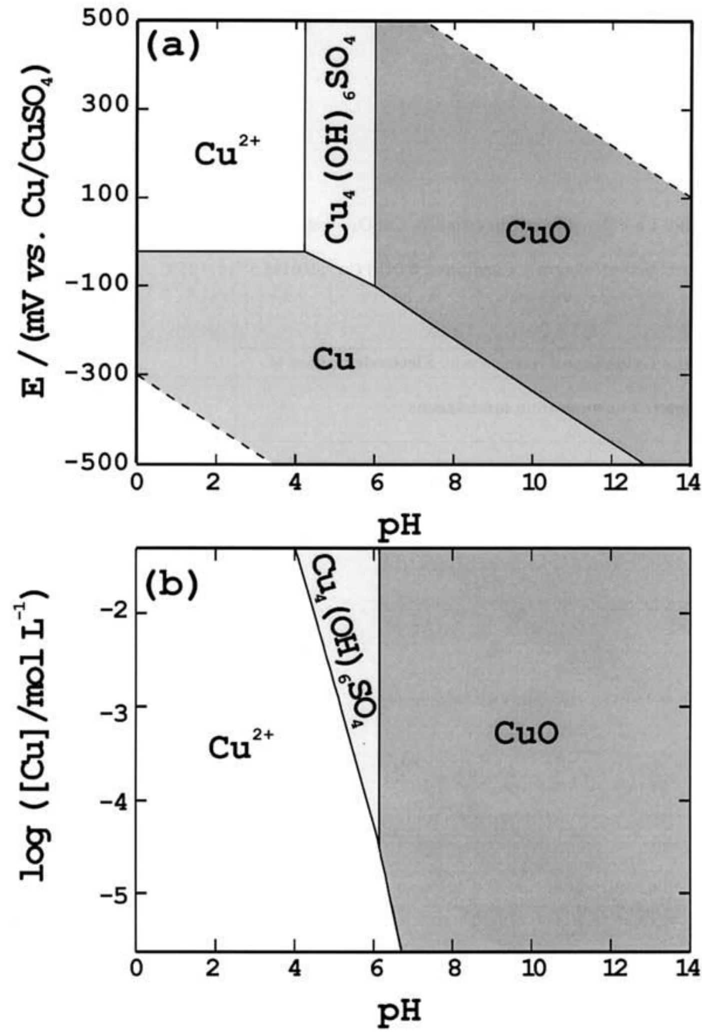

Figure 45 Equilibrium diagrams for CuSO4/water system: (a) $E_{Cu/Cu2+}$/ pH diagram, (b) distribution pH diagram. Conditions: 0.01 M Cu^{2+},0.01M S^{6+}, room temperature.[64]

Accordingly, soluble copper concentration rapidly decreases by two orders of magnitude for a unit increase of pH, yielding to the copper hydroxy sulfate. Consequently, the experiments in this investigation were limited to pH region in which copper was soluble.

4.1.2 Nucleation modeling

Chronoamperometry was used as an electrochemical method for copper deposition as a

technique suitable for electrochemical nucleation mechanisms studies. In chronoamperometry experiments, the potential was stepped from the open-circuit potential to the potential at which the deposition of copper would occur. Under these conditions, the system made a transition from no reaction to the steady-state reaction, controlled by the rate of mass transfer of cupric ions toward the electrode surface. Such transition is always followed by the current transient until the steady-state is achieved, as described by the Cottrell equation,

$$\mathrm{i} = \frac{nFD^{1/2}C_0}{\pi^{1/2}t^{1/2}}$$

where, i current density; n, number of electrons involved; F, Faraday constant; D, diffusion coefficient; $\mathrm{C_0}$, the concentration of species in the bulk and t , time. In the case of heterogeneous systems under diffusion control, nuclei formed on the surface contribute to the active surface area available for reaction. The initial current increase for heterogeneous systems is due to the increase of surface area whenever the nucleation is involved. As nucleation progresses, the nuclei will begin overlapping. Each nucleus will define its own diffusion zone through which copper has to diffuse, representing the mass- supplying mechanism for continuation of growth. Since the diffusion zones are much larger than the underlying nuclei, the overlapping zones would eventually include the entire electrode area. Further reaction is strictly controlled by the rate of mass transfer through the control area of the diffusion zone, i.e., the system is under steady state conditions. Within the diffusion zone, the growth of already-established copper nuclei can continue, or additional nucleation can be initiated on various sites, both governed by the steady-state conditions, as described by the Cottrell equation.

Chronoamperometry is an analytical, diagnostic electrochemical technique because it provides the current transients. These were effectively used by Scharifker and Hills to derive the mathematical models that describe the nucleation mechanisms. According to the models, there are two limiting nucleation mechanisms, the instantaneous and the progressive. Instantaneous nucleation corresponds to slow growth of nuclei on a small number of active sites; all activated at the same time. Progressive nucleation corresponds to the fast growth of nuclei on many active sites; all activated during the course of electr-reduction.

The models for instantaneous and progressive nucleation are given by equations, respectively

$$\frac{i^2}{{i_m}^2} = \frac{1.9542}{\frac{t}{t_m}}\left\{1 - exp\left[-1.2564\left(\frac{t}{t_m}\right)\right]\right\}^2$$

$$\frac{i^2}{{i_m}^2} = \frac{1.2254}{\frac{t}{t_m}}\left\{1 - exp\left[-2.3367\left(\frac{t}{t_m}\right)\right]\right\}^2$$

where i_m and t_m are current and time coordinates of the peak, respectively.

4.2 Effect of Cu ion concentration on the early stage of electrodeposition

Effect of Cu concentration was studied using CuSO4 electrolyte at pH 3.5 for 4 different Cu ion concentrations, 10mM, 50mM, 100mM, 1M. All experiments were performed at an applied potential of -100 mV vs. Ag/AgCl. The results are presented in Fig 46.

The OPL data show two distinct features: an increase at the very beginning, and a significant drop after a short period of time, showing a peak in OPL curve. The peak width increases with the decrease of Cu ion concentration. This optical observation can be well explained, and it reveals

the dynamics of the beginning of electrodeposition.

The OPL increase is caused by the deposition of thin film of Cu, which is thin enough to allow light to reach to Cu/electrolyte interface, the new top interface (before deposition, it is an Au/electrolyte interface). This Cu/electrolyte is growing with more deposition, and as the thickness of Cu increase, light cannot pass through the Cu layer, so this top interface disappears. Then, the interference pattern is only from the bottom interface (glass/air interface) and glass/Cr interface. The interference pattern will reflect the OPL change due to the disappearance of the top interface; an OPL decrease corresponding to the disappearance of the light from the top interface. The peak width is the measure of time to reach to the thickness which would block the light. In an electrolyte with a low concentration of Cu ion, it requires a longer time to deposit Cu to reach to the same thickness. For OPL curve, this means that the peak width will be larger, which is indeed the results we obtained. The reflection measurements re-verified this mechanism. When the Cu layer grows thicker, more light is reflected. When the Cu layer completely blocks the light, the reflection saturates the detector, reaching to the maximum.

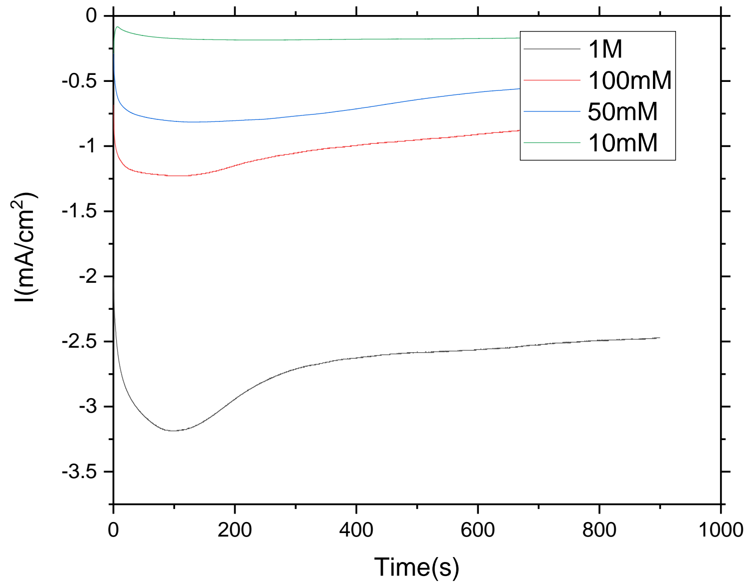

Figure 46 Current density versus time as copper concentration increasing.

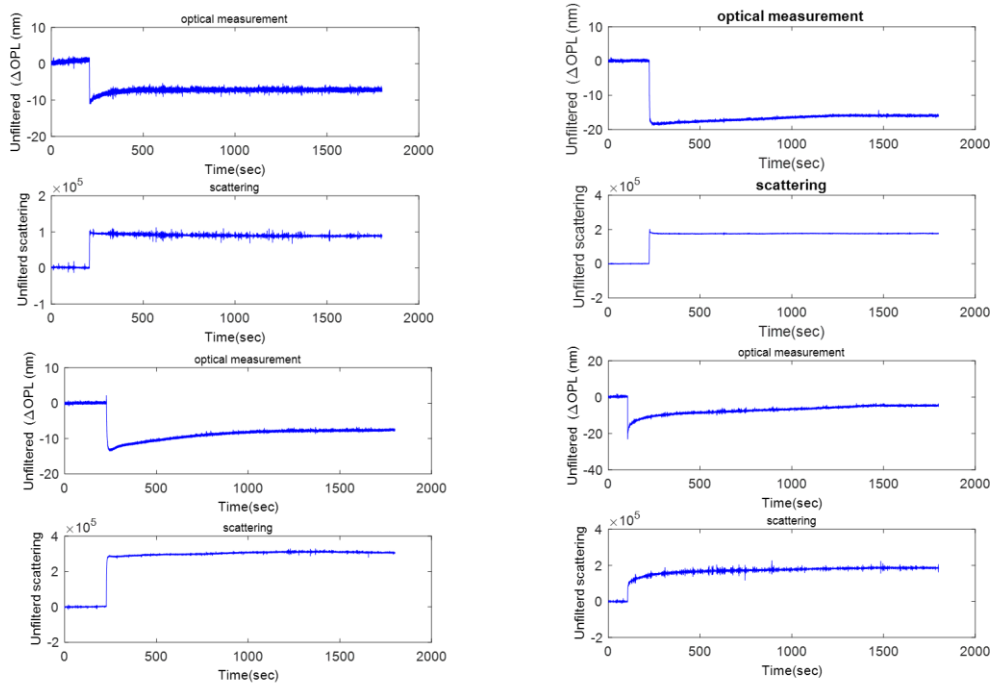

Figure 47 Phase and scattering result for 1M $CuSO_4$ deposition on the Au surface.

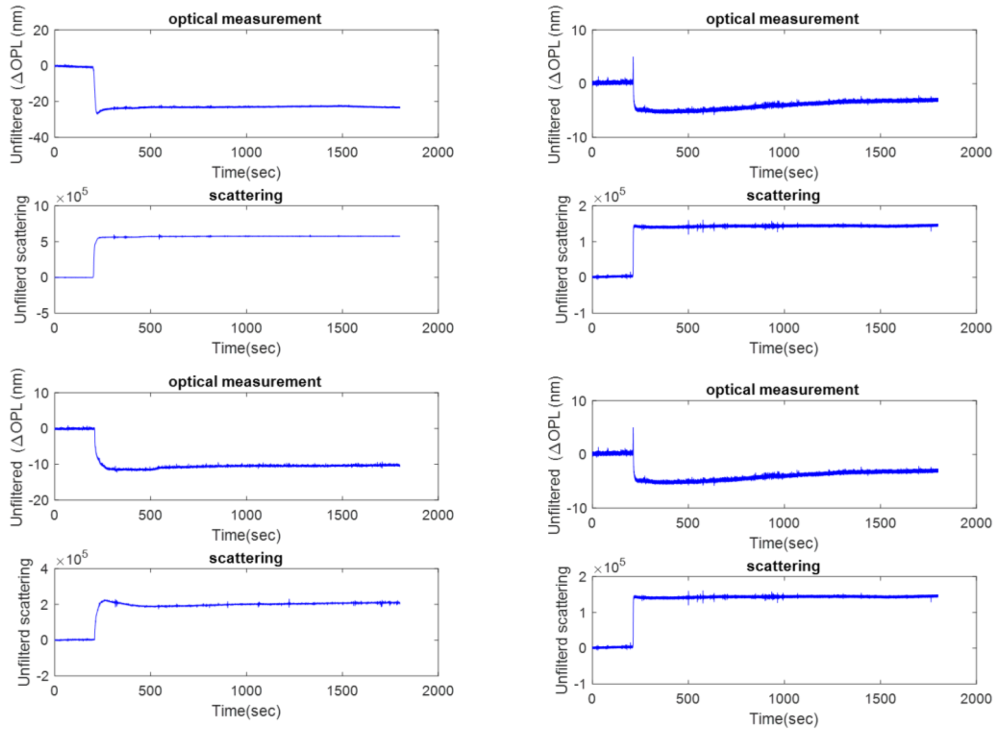

Figure 48 Phase and scattering result for 0.1M $CuSO_4$ deposition.

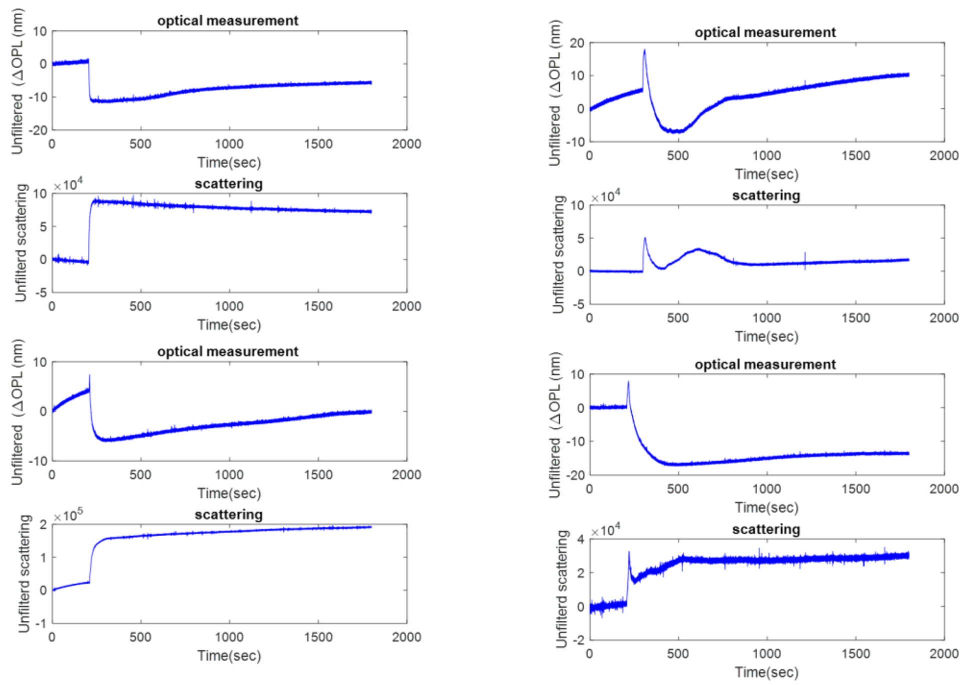

Figure 49 Phase and scattering result for 0.05M $CuSO_4$ deposition.

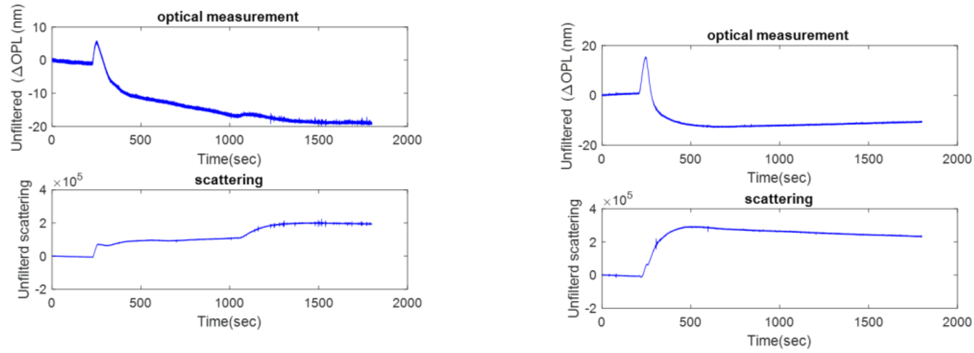

Figure 50 Phase and scattering result for 0.01M $CuSO_4$ deposition.

4.3 Effect of Applied Potential

We studied the effect of applied potential on Cu electrodeposition process. All experiments were conducted using a 100 mM CuSO4 electrolyte at pH 3.5. The reported applied potential is vs. Ag/AgCl. We first used pulse potential, starting and stopping electrodeposition several times in one experiment

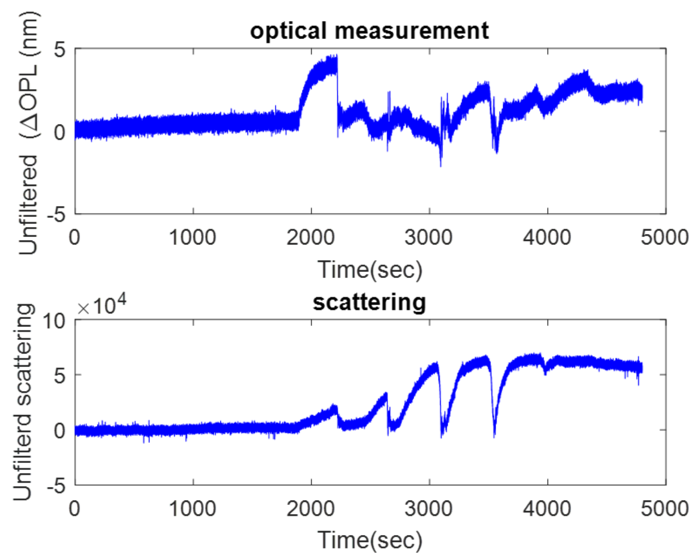

Figure 51 potential varied from +0.1V to minus -0.1V at 100mM $CuSO_4$.

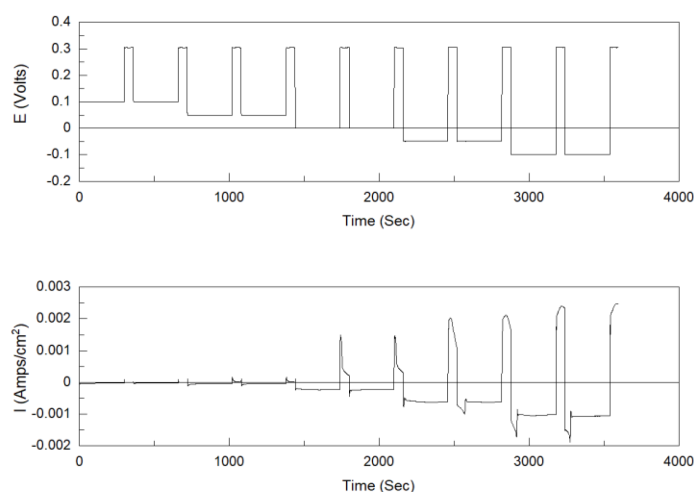

Figure 52 Current density and potential versus time from +0.1V to minus -0.1V at 100mM $CuSO_4$.

Fig 51 represents the OPL result for a potential change, and the corresponding current density curve is shown in Fig 52. Applied potential change from 0.1V to -0.1V, with a step of 0.05 V. Each potential was applied for two pulses. For each pulse, the potential was applied for 6 mins, then opened the circuit for 1 min. Optical data showed that at potential more negative than 0 V, OPL changed accordingly.

Then we conducted experiments doing electrodeposition at four specific potentials, 0.1 V, -0.0 V, -0.1 V and -0.2 V. The optical and the current density result was shown From Figure 53 to Fig 56. The SEM images and EDX mapping result are shown in Fig 57to Fig 60.

At 0.1 V, OPL did not change, and from SEM and EDX, no Cu was detected. This suggests that deposition was not started. At 0.0 V, OPL clearly changed with an applied potential, but from SEM and EDX, no Cu was detected. Substantial change (~10 nm) of OPL can come only from the accumulation of ions on the top interface. However, at -0.1 V and -0.2 V, there is a smaller

change of OPL (~5 nm), and thick Cu film was clearly seen on the substrates (from SEM and EDX). There are two possible reasons for this change: i) Temperature increase due to the relatively large current causing thermal expansion of the substrate, which can cause OPL change. ii) The Kerr effect changes the refractive index of metal layers, i.e., refractive index changes under specific electric field. The real mechanism of this phenomenon requires more study. But from these experiments, we can conclude that a small current cannot cause any change in optical measurements. This firmly confirm the optical observation for UPD of Cu does indeed come from the deposition and removal of a monolayer of Cu

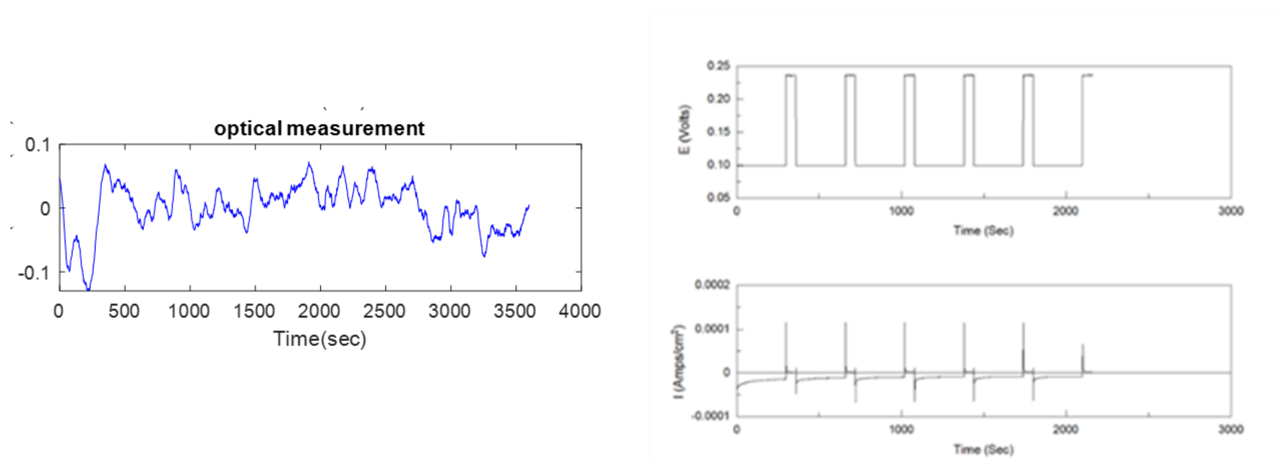

Figure 53 Phase result corresponding Current and potential versus time for potential applied -0.1V.

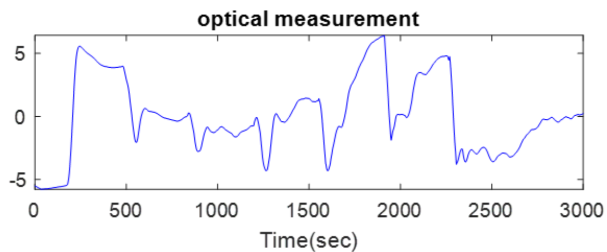

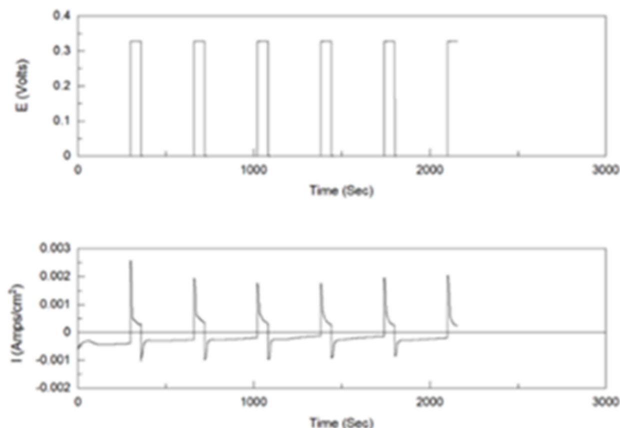

Figure 54 Phase result corresponding Current and potential versus time for potential applied 0V.

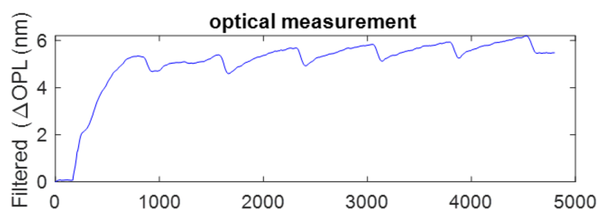

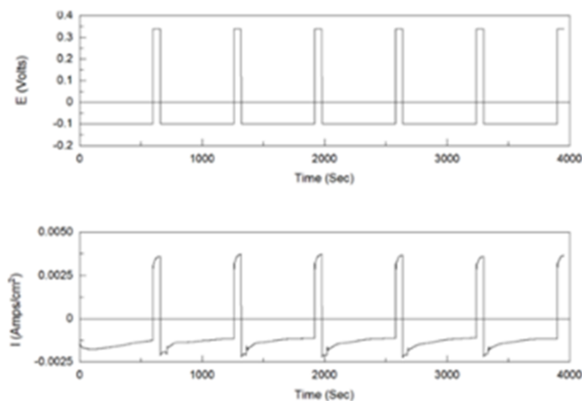

Figure 55 Phase result corresponding Current and potential versus time for potential applied -0.1V.

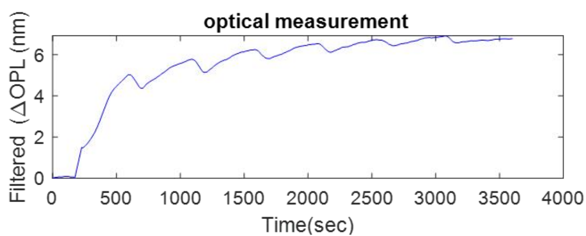

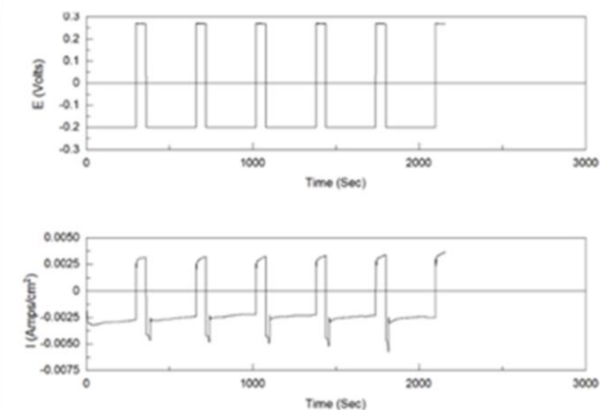

Figure 56. Phase result corresponding Current and potential versus time for potential applied -0.2V.

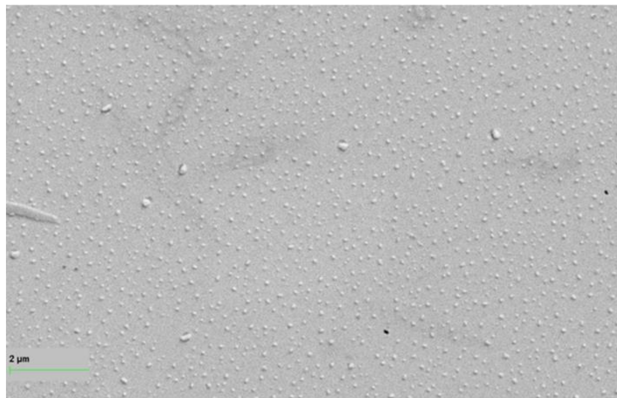

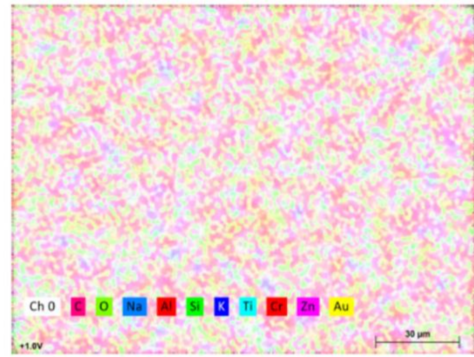

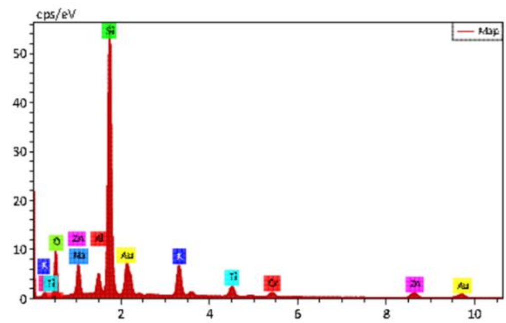

Figure 57 SEM and EDX image for 0.1V pulse experiment at 100mM CuSO4.

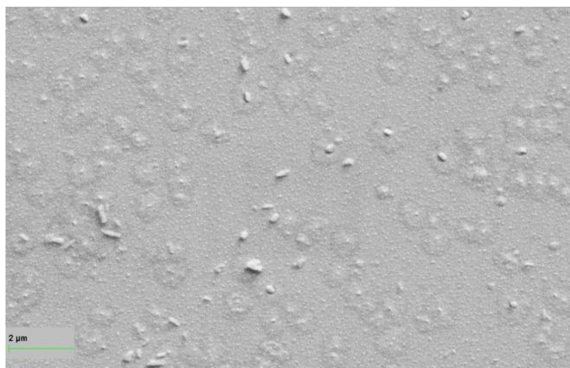

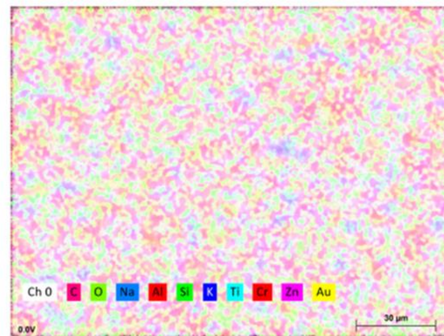

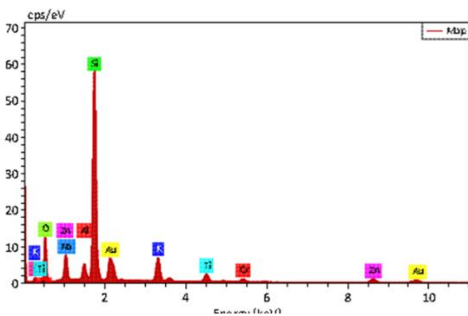

Figure 58 SEM and EDX image for 0V pulse experiment at 100mM CuSO4

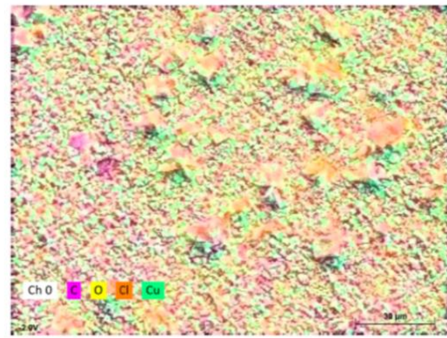

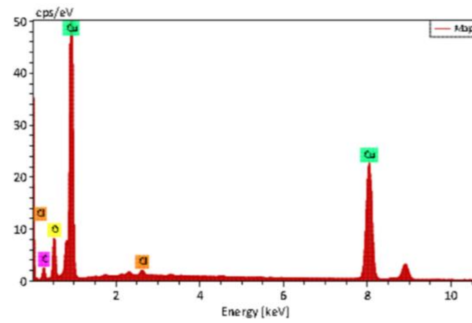

Figure 59 SEM and EDX image for-0.1V pulse experiment at 100mM $CuSO_4$.

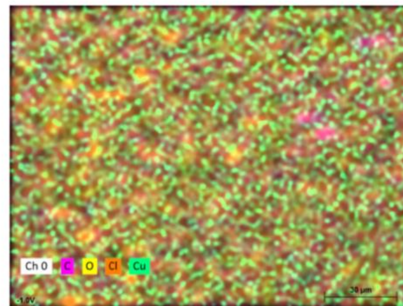

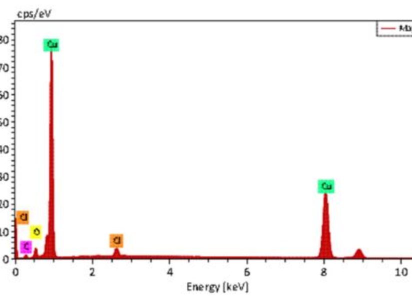

Figure 60 SEM and EDX image for -0.2V pulse experiment at 100mM $CuSO_4$.

5. Conclusions and Future study

We used SDPSI to study the cyclic voltammetry (CV) of underpotential deposition (UPD) of Cu on Au surface. We demonstrated that SDPSI could detect the monolayer film formation in real time, allowing us to “see” the atomic processes at the substrate surface during CV measurements. We proved that SDPSI could be used as a real-time monitor with a sub-monolayer resolution for electrodeposition.

Also, we used SDPSI to study the atomic processes in the pre-deposition and initial deposition stage of general electrodeposition processes. We found that SDPSI can detection accumulation on the substrate surface before the deposition takes place, and accurately predict the initial deposition potential. Also, it has been found that such initial deposition potential has a dependence on the substrate thickness for ultra-thin film working electrodes.

We clearly demonstrated that SDSPI is a reliable new tool for real-time probing electrodeposition processes. It can be used as a thickness monitor for electrodeposition, a long-awaited scientific breakthrough.

Future study

Atomic layer study is also a favorite topic; the technique can apply to the investigation of building

monolayer on the different surface. Atomic layer deposition (ALD), in which atomic layer control and conformal growth are achieved through sequential, self-limiting surface reactions. For one the application of ALD, it deposits ultrathin layers of expensive metals such as Pt that is used, for example, as the catalyst in proton-exchange membrane fuel cells. Another one needs to be mentioned, the economic method to grow ultrathin film which can extensively apply in the property modification of catalytic, electronic, or magnetic materials.

Although ALD processes are usually conducted in the vapor phase, it was reported in 2012 that two-dimensional Pt film could be deposited layer by layer using electrodeposit by merely pulsing the applied electrochemical potential in a single plating bath as shown in Figure 61. This process is easily achieved and is inexpensive and rapid. Because each layer is produced by cycling the potential rather than by exchange of reactants, electrochemical ALD could be orders of magnitude faster than vapor-phase ALD.

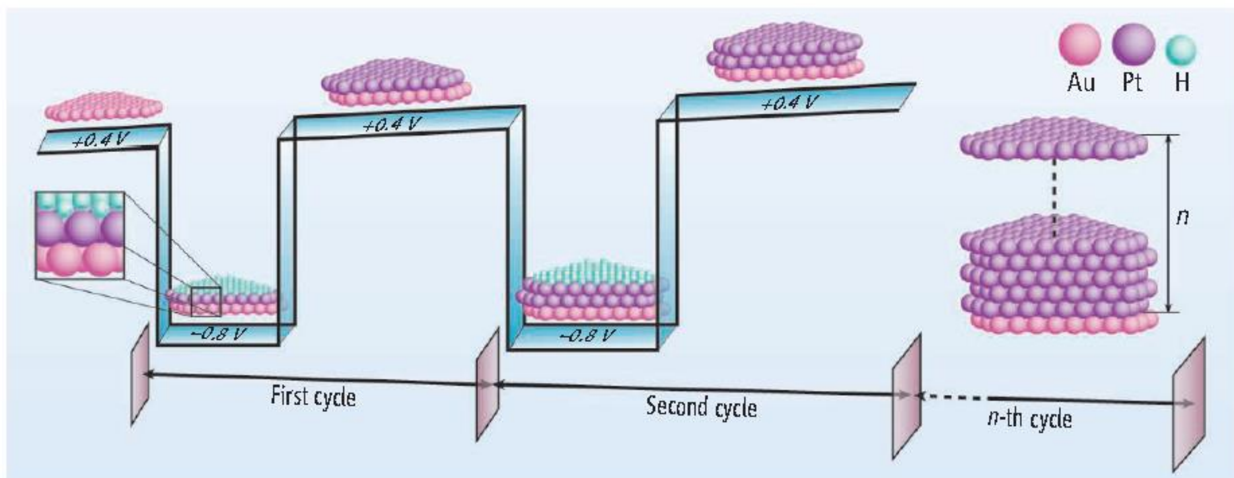

Figure 61 One step at a time. Electrochemical atomic layer deposition of ultrathin Pt films deposited one monolayer at a time by merely pulsing the electrode potential between +0.4 and –0.8 V. A capping layer of hydrogen is produced at –0.8 V that blocks

the deposition of more than one monolayer of Pt. When the potential is stepped to +0.4 V, the hydrogen layer is desorbed, and the cycle can begin again. The self-limiting processing method is fast because it is performed in a single plating bath, so it is not necessary to exchange reactants. The ultrathin Pt films could lower the costs of the Pt catalyst in fuel cells and provide a platform to study how the catalytic, electronic, and magnetic properties of ultrathin films evolve with film thickness.[6]

However, even though the significance of using such method for ALD is apparent, people have not seen much research activities in this field. The main reason is the lack of in-situ monitoring tool which can tell if indeed a monolayer forms. Here, we can provide an in-situ monitoring tool with monolayer resolution for electrodeposition. We believe that with this tool many systems can try to produce monolayer metal films or metal films layer by layer. This will be the next step in continuing this research.

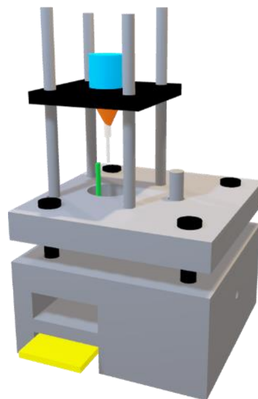

Figure 62 New cell set up for the top light source.

Reference

1. Attard, G.S., et al., *Mesoporous Platinum Films from Lyotropic Liquid Crystalline Phases.* Science, 1997. **278**(5339): p. 838.
2. Harniman, R.L., et al., *Real-time tracking of metal nucleation via local perturbation of hydration layers.* Nature Communications, 2017. **8**(1): p. 971.
3. Kim, J., J.E. Dick, and A.J. Bard, *Advanced Electrochemistry of Individual Metal Clusters Electrodeposited Atom by Atom to Nanometer by Nanometer.* Accounts of Chemical Research, 2016. **49**(11): p. 2587-2595.
4. Lam, B., et al., the *Programmable definition of nanogap electronic devices using self-inhibited reagent depletion.* Nat Commun, 2015. **6**: p. 6940.
5. Liu, Y., et al., *Self-Terminating Growth of Platinum Films by Electrochemical Deposition.* Science, 2012. **338**(6112): p. 1327.
6. Switzer, J.A., *Atomic Layer Electrodeposition.* Science, 2012. **338**(6112): p. 1300.
7. Zach, M.P., K.H. Ng, and R.M. Penner, *Molybdenum Nanowires by Electrodeposition.* Science, 2000. **290**(5499): p. 2120.
8. Heerman, L. and A. Tarallo, *Theory of the chronoamperometric transient for electrochemical nucleation with diffusion-controlled growth.* Journal of Electroanalytical Chemistry, 1999. **470**(1): p. 70-76.
9. Scharifker, B. and G. Hills, *Theoretical and experimental studies of multiple nucleations.* Electrochimica Acta, 1983. **28**(7): p. 879-889.
10. Hyde, M.E., R. Jacobs, and R.G. Compton, *In Situ AFM Studies of Metal Deposition.* The Journal of Physical Chemistry B, 2002. **106**(43): p. 11075-11080.
11. Jiang, Y., et al., *In situ Study of Oxidative Etching of Palladium Nanocrystals by Liquid Cell Electron Microscopy.* Nano Letters, 2014. **14**(7): p. 3761-3765.
12. Radisic, A., et al., *Quantifying Electrochemical Nucleation and Growth of Nanoscale Clusters Using Real-Time Kinetic Data.* Nano Letters, 2006. **6**(2): p. 238-242.
13. Ustarroz, J., et al., *The Role of Nanocluster Aggregation, Coalescence, and Recrystallization in the Electrochemical Deposition of Platinum Nanostructures.* Chemistry of Materials, 2014. **26**(7): p. 2396-2406.
14. Ustarroz, J., et al., *A Generalized Electrochemical Aggregative Growth Mechanism.* Journal of the American Chemical Society, 2013. **135**(31): p. 11550-11561.
15. Ustarroz, J., et al., *New Insights into the Early Stages of Nanoparticle Electrodeposition.*

The Journal of Physical Chemistry C, 2012. **116**(3): p. 2322-2329.

16. White, E.R., et al., *In Situ Transmission Electron Microscopy of Lead Dendrites and Lead Ions in Aqueous Solution.* ACS Nano, 2012. **6**(7): p. 6308-6317.

17. Zeng, Z., et al., *Visualization of Electrode-Electrolyte Interfaces in LiPF6/EC/DEC Electrolyte for Lithium-Ion Batteries via in Situ TEM.* Nano Letters, 2014. **14**(4): p. 1745-1750.

18. Dietterle, M., T. Will, and D.M. Kolb, *The initial stages of Cu electrodeposition on Ag(100): an in situ STM study.* Surface Science, 1998. **396**(1): p. 189-197.

19. Manne, S., et al., *Atomic-Resolution Electrochemistry with the Atomic Force Microscope: Copper Deposition on Gold.* Science, 1991. **251**(4990): p. 183.

20. Matsushima, H., et al., *In situ video-STM studies of the mechanisms and dynamics of electrochemical bismuth nanostructure formation on Au.* Faraday Discussions, 2016. **193**(0): p. 171-185.

21. Momotenko, D., et al., *High-Speed Electrochemical Imaging.* ACS Nano, 2015. **9**(9): p. 8942-8952.

22. Perry, D., et al., *Simultaneous Nanoscale Surface Charge and Topographical Mapping.* ACS Nano, 2015. **9**(7): p. 7266-7276.

23. Poloni, L.N., et al., *Best Practices for Real-Time in Situ Atomic Force and Chemical Force Microscopy of Crystals.* Chemistry of Materials, 2017. **29**(1): p. 331-345.

24. Pötzschke, R.T., et al., *Nanoscale studies of Ag electrodeposition on HOPG (0001).* Electrochimica Acta, 1995. **40**(10): p. 1469-1474.

25. Radisic, A., F.M. Ross, and P.C. Searson, *In Situ Study of the Growth Kinetics of Individual Island Electrodeposition of Copper.* The Journal of Physical Chemistry B, 2006. **110**(15): p. 7862-7868.

26. Simm, A.O., et al., *AFM Studies of Metal Deposition: Instantaneous Nucleation and the Growth of Cobalt Nanoparticles on Boron-Doped Diamond Electrodes.* ChemPhysChem, 2006. **7**(3): p. 704-709.

27. Tansel, T., A. Tarkovsky, and O.M. Magnussen, *In Situ Video-STM Studies of Adsorbate Dynamics at Electrochemical Interfaces.* ChemPhysChem, 2010. **11**(7): p. 1438-1445.

28. Velmurugan, J., J.-M. Noël, and M.V. Mirkin, *Nucleation and growth of mercury on Pt nanoelectrodes at different overpotentials.* Chemical Science, 2014. **5**(1): p. 189-194.

29. Wang, Y., X. Shan, and N. Tao, *Emerging tools for studying single entity electrochemistry.* Faraday Discussions, 2016. **193**(0): p. 9-39.

30. Williamson, M.J., et al., *Dynamic microscopy of nanoscale cluster growth at the solid-liquid interface.* Nature Materials, 2003. **2**: p. 532.

31. Wintterlin, J., et al., *Real-time STM observations of atomic equilibrium fluctuations in an adsorbate system: O/Ru(0001).* Surface Science, 1997. **394**(1): p. 159-169.

32. Zoval, J.V., et al., *Electrochemical Deposition of Silver Nanocrystallites on the Atomically*

Smooth Graphite Basal Plane. The Journal of Physical Chemistry, 1996. **100**(2): p. 837-844.

33. Kissinger, P.T. and W.R. Heineman, *Cyclic voltammetry.* Journal of Chemical Education, 1983. **60**(9): p. 702.

34. Schultze, J.W. and D. Dickertmann, *Potentiodynamic desorption spectra of metallic monolayers of Cu, Bi, Pb, Tl, and Sb adsorbed at (111), (100), and (110) planes of gold electrodes.* Surface Science, 1976. **54**(2): p. 489-505.

35. Omar, I.H., H.J. Pauling, and K. Jüttner, *Underpotential Deposition of Copper on Au(III) Single-Crystal Surfaces: A Voltammetric and Rotating Ring Disk Electrode Study.* Journal of The Electrochemical Society, 1993. **140**(8): p. 2187-2192.

36. Cappadocia, M., et al., *Anion effects on the cyclic voltammetry of copper underpotential deposition on Au(100).* Journal of Electroanalytical Chemistry, 1996. **405**(1): p. 227-232.

37. Grégoire, H., and A.D.W. M., *Underpotential Deposition and Stripping of Lead at Disorganized Monolayer-Modified Gold Electrodes.* Electroanalysis, 2005. **17**(20): p. 1816-1821.

38. Herrero, E., L.J. Buller, and H.D. Abruña, *Underpotential Deposition at Single Crystal Surfaces of Au, Pt, Ag and Other Materials.* Chemical Reviews, 2001. **101**(7): p. 1897-1930.

39. Aitchison, H., et al., *Underpotential deposition of Cu on Au(111) from neutral chloride-containing the electrolyte.* Physical Chemistry Chemical Physics, 2017. **19**(35): p. 24146-24153.

40. Zhang, J., et al., *Underpotential deposition of Cu on Au(111) in sulfate-containing electrolytes: A theoretical and experimental study.* The Journal of Chemical Physics, 1996. **104**(14): p. 5699-5712.

41. Sudha, V. and M.V. Sangaranarayanan, *Underpotential deposition of metals – Progress and prospects in modeling.* Journal of Chemical Sciences, 2005. **117**(3): p. 207-218.

42. Vélez, P., et al., *The underpotential deposition that should not be: Cu(1 × 1) on Au(111).* Electrochemistry Communications, 2012. **25**: p. 54-57.

43. Tadjeddine, A., et al., *Electronic and structural characterization of underpotentially deposited submonolayers and a monolayer of copper on gold (111) studied by in situ x-ray-absorption spectroscopy.* Physical Review Letters, 1991. **66**(17): p. 2235-2238.

44. Tourillon, G., D. Guay, and A. Tadjeddine, *In-plane structural and electronic characteristics of underpotentially deposited copper on gold (100) probed by in-situ X-ray absorption spectroscopy.* Journal of Electroanalytical Chemistry and Interfacial Electrochemistry, 1990. **289**(1): p. 263-278.

45. Blum, L., et al., *Study of underpotentially deposited copper on gold by fluorescence detected surface EXAFS.* The Journal of Chemical Physics, 1986. **85**(11): p. 6732-6738.

46. Tadjeddine, A., A. Lahrichi, and G. Tourillon, *In-situ X-ray absorption near-edge structure: a probe of the oxidation state of underpotentially adsorbed metals.* Journal of Electroanalytical Chemistry, 1993. **360**(1): p. 261-270.

47. Magnussen, O.M., et al., *Atomic structure of Cu adlayers on Au(100) and Au(111) electrodes observed by in situ scanning tunneling microscopy.* Physical Review Letters, 1990. **64**(24): p. 2929-2932.

48. Yang, Y.-C., K. Hecker, and O.M. Magnussen, *In situ video-scanning tunneling microscopy studies of the structure and dynamics of Cl adlayers on Au(1 0 0) electrodes.* Electrochimica Acta, 2013. **112**: p. 881-886.

49. Carnal, D., et al., *In-situ STM investigation of Tl and Pb underpotential deposition on chemically polished Ag(111) electrodes.* Electrochimica Acta, 1995. **40**(10): p. 1223-1235.

50. Schlaup, C. and K. Wandelt, *In-situ STM study of sulfide adsorption on Au(100) in alkaline solution.* Surface Science, 2015. **631**: p. 165-172.

51. Lecadre, F., et al., *Ni electrochemical epitaxy on unreconstructed Au(111): An in-situ STM study.* Surface Science, 2015. **631**: p. 135-140.

52. Phan, T.H., T. Kosmala, and K. Wandelt, *Potential dependence of self-assembled porphyrin layers on a Cu(111) electrode surface: In-situ STM study.* Surface Science, 2015. **631**: p. 207-212.

53. Stuhlmann, C., et al., *An ex-situ study of Cd underpotential deposition on Cu(111).* Electrochimica Acta, 1998. **44**(6): p. 993-998.

54. S., Z.M., et al., *The influence of anions on the structure of underpotentially deposited Cu on Au(111): A LEED, RHEED, and AES study.* Berichte der Bunsengesellschaft für Physikalische Chemie, 1987. **91**(4): p. 349-353.

55. Abruña, H.D., et al., *X-Ray standing wave study of copper underpotentially deposited on Au(100).* Journal of Electroanalytical Chemistry, 1993. **360**(1): p. 315-323.

56. Al-Shakran, M., L.A. Kibler, and T. Jacob, *Homoepitaxial electrodeposition on reconstructed and unreconstructed Au(100): An in-situ STM study.* Surface Science, 2015. **631**: p. 130-134.

57. Meiners, F., et al., *Impact of temperature and electrical potentials on the stability and structure of collagen adsorbed on the gold electrode.* Surface Science, 2015. **631**: p. 220-228.

58. Hölzle, M.H., V. Zwing, and D.M. Kolb, *The influence of steps on the deposition of Cu onto Au(111).* Electrochimica Acta, 1995. **40**(10): p. 1237-1247.

59. Villegas, I., X. Gao, and M.J. Weaver, *Local structure and phase transitions within ordered electrochemical adlayers: Some new insights from in situ scanning tunneling microscopy.* Electrochimica Acta, 1995. **40**(10): p. 1267-1275.

60. Schlaup, C., S. Horch, and I. Chorkendorff, *On the stability of copper overlayers on Au(1 1 1) and Au(1 0 0) electrodes under low potential conditions and in the presence of CO and CO2.* Surface Science, 2015. **631**: p. 155-164.

61. Oyamatsu, D., et al., *Underpotential Deposition of Silver onto Gold Substrates Covered with Self-Assembled Monolayers of Alkanethiols To Induce Intervention of the Silver

between the Monolayer and the Gold Substrate. Langmuir, 1998. **14**(12): p. 3298-3302.

62. Vakhtin, A.B., et al., *Common-path interferometer for frequency-domain optical coherence tomography.* Applied Optics, 2003. **42**(34): p. 6953-6958.

63. M., A.D.W., I. Tabassum, and P.M. J., *Underpotential Deposition of Copper at Mercaptoalkane Sulfonate-Coated Polycrystalline Gold.* Electroanalysis, 2001. **13**(8-9): p. 751-754.

64. Johnson, P.B. and R.W. Christy, *Optical Constants of the Noble Metals.* Physical Review B, 1972. **6**(12): p. 4370-4379.

Appendix

A.Raw data of phase result including fitting

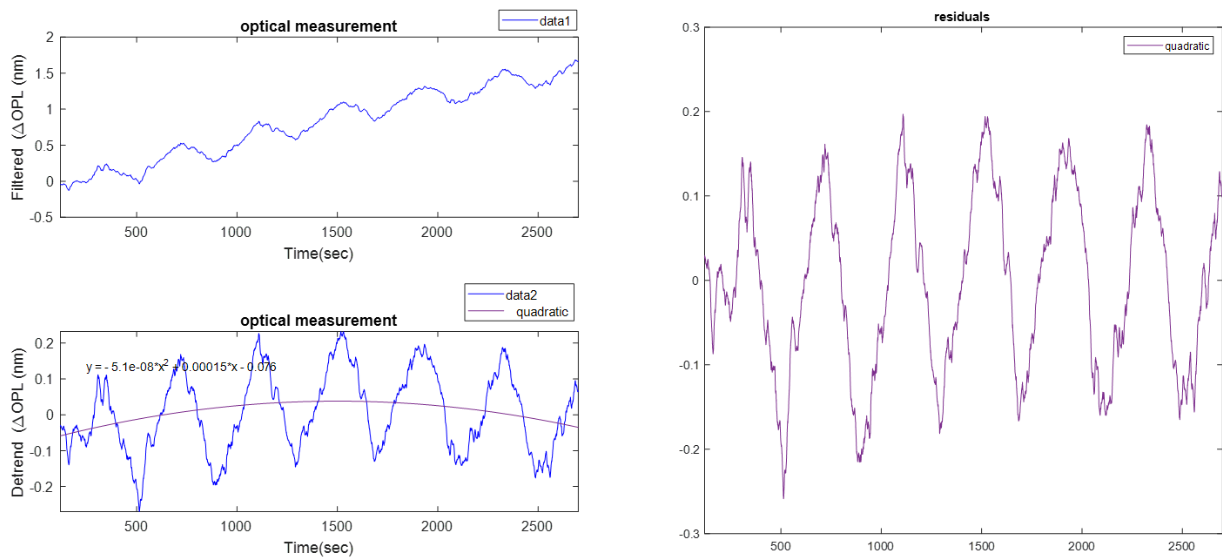

Figure 63 Optical result for Copper UPD CV experiment proceeding at the 2mvs^{-1}and Fitting figure.

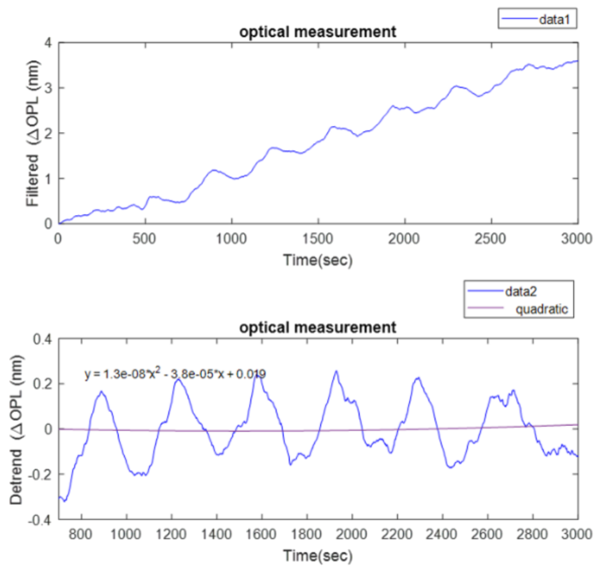

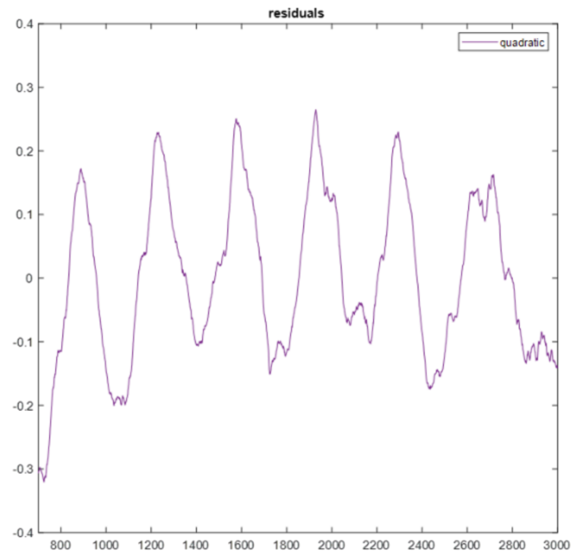

Figure 64 Optical result for Copper UPD CV experiment proceeding at 2mvs^{-1} and Fitting figure.

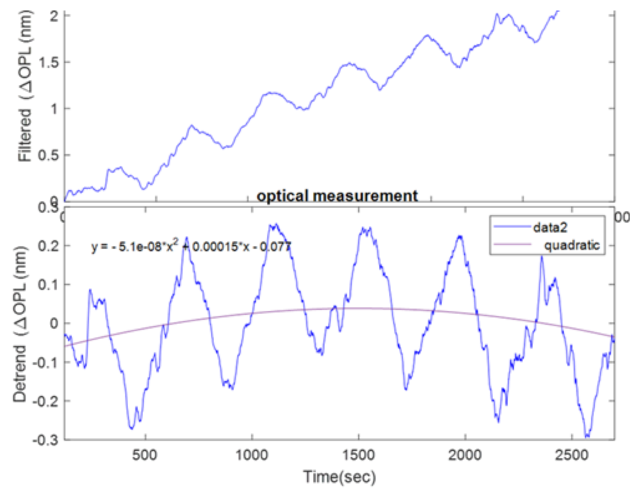

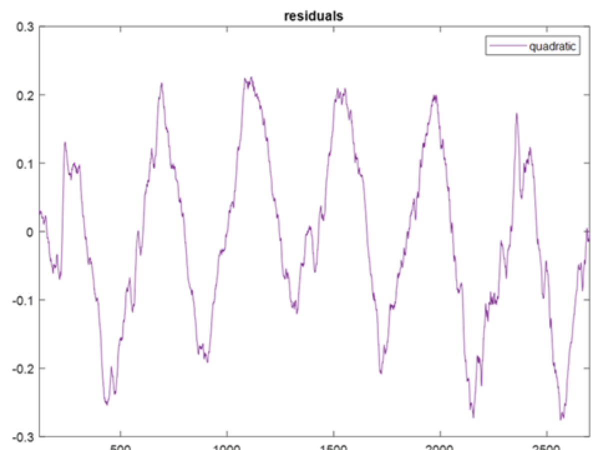

Figure 65 Optical result for Copper UPD CV experiment proceeding at 5mvs^{-1} and Fitting figure.

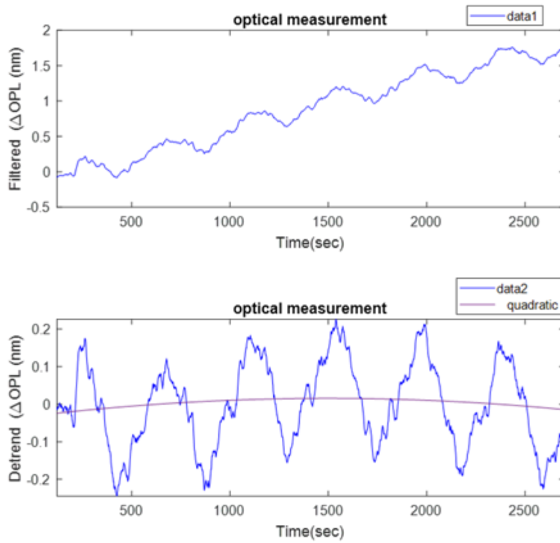

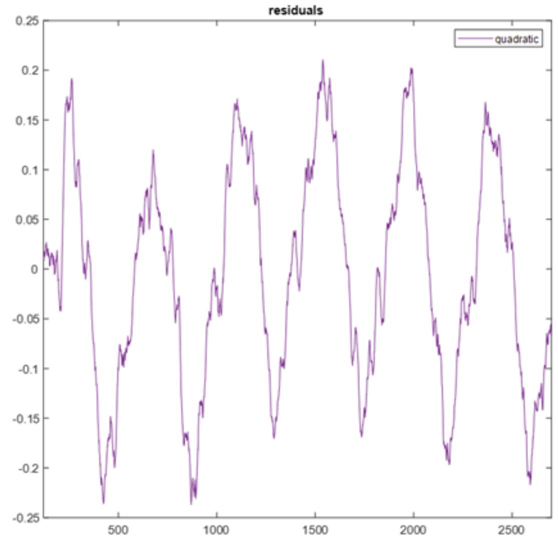

Figure 66 Optical result for Copper UPD CV experiment proceeding at 5mvs^{-1} and Fitting figure.

B.Optical properties Cu and Au

The interference signal not only provides direct evidence about the monolayer formation but also provides a measure of optical properties of monolayer Cu. The optical path length change, OPL, due to UPD of Cu, is about 0.5 nm. We know that OPL= n × 2 × d, where n is the refractive index, and d is the thickness. Because light goes through the film twice (incident and reflected from the top interface), there is a factor of 2 in this equation.

When we take Cu thickness as the diameter of Cu atom, which is 0.256 nm, n calculated from above equation will be close to 1, which is far away from the measured bulk Cu refractive index (for light with 800 nm wavelength), 0.26.

This massive discrepancy results from several reasons. First, it has been shown that bisulfate ions bind to Cu atoms, but not to Au atoms. So, during UPD of Cu, the Au/electrolyte interface is changing to Cu/bisulfate ions/electrolyte. The optical path length change includes the additional difference between the refractive index change between the bisulfate ion layer and electrolyte. We can see that with this consideration the results we got are reasonable.

The optical constants of the noble metals have been measured since the time of Drude, with continuing attempts to increase the experimental accuracy, for the purpose of comparison with theory. From the earliest results that Drude's free-electron theory failed in the visible and near-ultraviolet regions. After the quantum theory, it was recognized' that the absorption in the visible and ultraviolet probably was due to transitions from the filled d bands into the sp conduction bands.

With more accurate measurements of the optical constants and detailed band-structure calculations, one could separate the free electron contribution from the effect of interband transitions, and try to identify the photon energies at which structure occurs in the measured interband absorption with energy gaps in the theoretical band structure. This work provides the crucial role of transitions from the d band and is supported by observations on the effects of stress and alloying.

For copper and gold, measurements have been finished to compare with quantitative calculations

of the interband optical constants based on refined band-structure calculations, considering the joint density of states and the transition-probability matrix elements throughout the Brillouin zone. In the experimental measurements, the result has been reasonably in a good agreement on the wavelengths at which structure occurs. However, the actual number of the optical constants, differ as reported by different investigators, even in the most recent and careful experiments. Since the actual value of the optical constants is now yielding to theoretical calculation, it is crucial to pin down the experimental values with accurate measurements including estimates of error.

Drude's polarimetric method has the advantage that explicit expressions for the optical constants n, k can be derived in terms of measured quantities, but the results obtained depend very sensitively on the surface preparation of the sample. The advent of sophisticated computing techniques encourages the use of other experimental methods which depend less sensitively on surface conditions, but which require numerical inversion of the equations for the optical constants. These include Kramers-Kronig analysis of normal incidence reflection measurements, reflection measurements at different incident angles, and transmission measurements through thin films. Each of methods has its own pros and cons.

Several investigations of copper, silver, and gold have used the Kramers-Kronig technique applied to normal-incidence reflection measurements. However, there is a problem with this method induced by the necessity of extrapolating the reflectance to the frequencies over the measured

range. For extrapolation, it has a significant effect on the magnitude of the optical constants, although the photon energies at which various structural features occur are insensitive to it. Other studies have used two reflection or transmission measurements. At different angles of incidence or with different polarizations, two reflection measurements from opaque samples yield values only over a relatively small range of the spectrum. The profile of reflection in the n-k plane may be nearly parallel and thus provided indefinite values of n and k. On the other side, a strategy using standard incidence transmission and reflection measurements on thin films can also encounter this problem and may have additional trouble with accurate measurement of the thickness of the film. To utilize three measurements on thin films, it can circumvent the above problems. Measurements of reflection and transmission at normal incidence can obtain accurate values for the two optical constants as well as accurately determining the film thickness. This technique is particularly convenient when a spectrophotometer is available, and one is dealing with such easily evaporated materials as the noble metals.

To determine the precise value , sample preparation becomes a crucial factor. Bulk samples are usually polished mechanically, chemically, or electrolytically, and then they may be annealed. Mechanical polishing may leave the surface structure distorted, and annealing may reduce surface smoothness. Thin films prepared by vacuum evaporation require no polishing. Rapidly evaporated films will reproduce the surface smoothness of the substrate and form a smooth, homogeneous surface. Films formed at slower evaporation rates can have a discontinuous agglomerated structure. **The optical properties of evaporated thin films have been found to be the same as for bulk materials, provided the thickness of the films is higher than 200-300 A.**

The optical constants n and k, as well as the thickness d of thin metal films, were determined

by inverting the normal-incidence reflection and transmission functions,R_0 and T_0. Compared to other thin-film techniques, A fitting method called three parameter fit has been described in detail for which is the excellent accuracy with the film thickness. **The accuracy of interferometric thickness measurements usually is about 30 Å, but if three optical measurements are inverted in an appropriate spectral range, then the thickness can usually be obtained to within 2 Å. The appropriate range is one in which the measured reflection and transmission values lie on contours which intersect steeply enough in the n-k plane.**

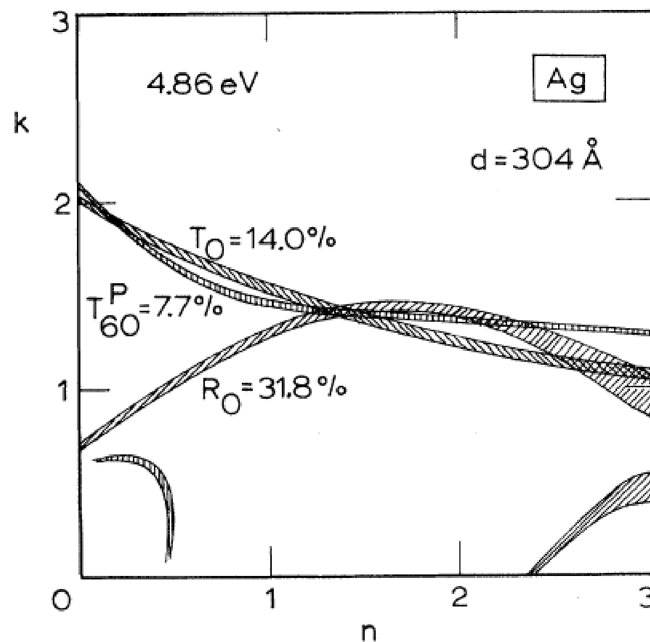

Figure 67 Example of the intersection in the n-k plane of normal-incidence R and T contours with the p-polarized T contour for 60' incident angle. The width of the contours, which represents the estimated experimental error, is exaggerated by a factor of 5 for the normal incidence contours.[64]

Figure 67 shows how the three contours intersect for a suitable wavelength. The width of the

contours represents the error in the measurements. n or k takes on values larger than 2 depending on the wavelength. However, the contours of the two transmissions are often nearly parallel. Once the actual film thickness has been determined from the average of the values in the appropriate spectral range, it can be used along with any two of three optical measurements in order to determine n and k over our entire spectral range. The normal-incidence reflection and transmission functions were usually used for this calculation.

Also, the computer methods have been suggested previously for inverting the complex reflection or transmission functions, with application to the inversion of two measurements to determine n and k. The three-parameter method used is based on an approximate Newton-Raphson technique of finding the intersections of the contours. Other methods of inverting three measurements have been mentioned, but they do not seem to have been widely used.

For using three measurements, it has another advantage on that they automatically determine the Physical solution. It is known that the reflection and transmission contours intersect at several points in the n-k plane, and an example of multiple intersections can be seen in Figure.67. The problem of determining which is the physical solution may be complicated, and at times the wrong intersections have been reported. A rule of thumb that the solution with the lowest value of n should be chosen seems to give the correct solution for the noble metals.

All of the data analysis was done in terms of the complex index of refraction n =n+ik. For average

values are shown in Table 3. Take $\epsilon=\epsilon_1+i\epsilon_2$ and $\epsilon=n^2$. The advantage of first considering n and k is that the intersections of reflection and transmission contours in the n-k plane are magnified in the interesting region near the origin. On the other hand, the dielectric constants ϵ_1, and ϵ_2 are closely related to the electronic structure of the solids and are more directly comparable with theory.

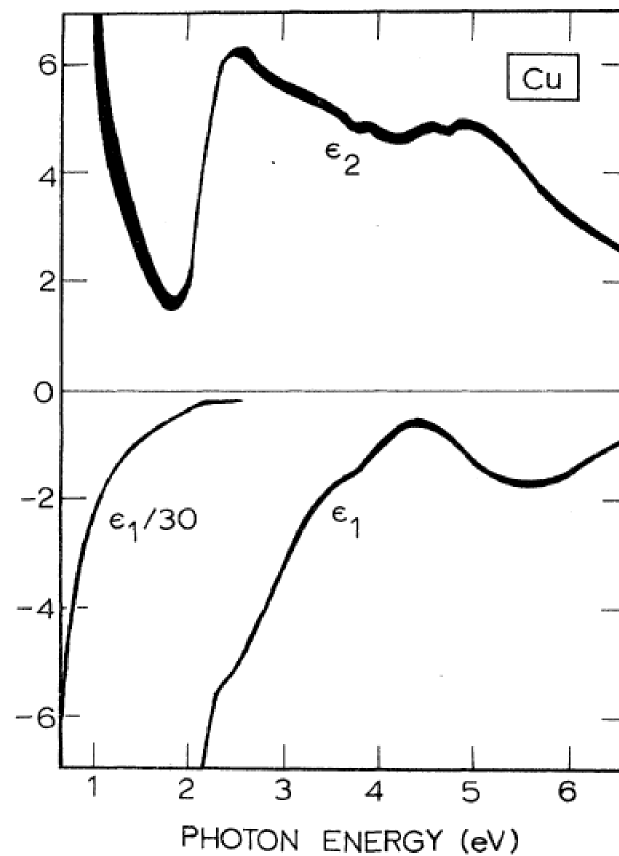

Figure 68 Dielectric constants for copper as a function of photon energy. The width of the curves is representative of the instrumenta1 error.[64]

A. Copper

Dielectric constants for copper are presented in Figure.68. The curves represent the average of values from the two films of thicknesses 297 and 305 Å, respectively. Below a certain critical film

thickness, the number varies somewhat with the material. Therefore the inferred dielectric constants depend on thickness. To verify ϵ1 and ϵ2 can be independent of thickness, there is another experiment on a 486-Å-thick copper film. These results agree with the error with the values obtained from the thinner films. The thinner film values are more accurate since the transmission of the thick film was less than 1% at long wavelengths.

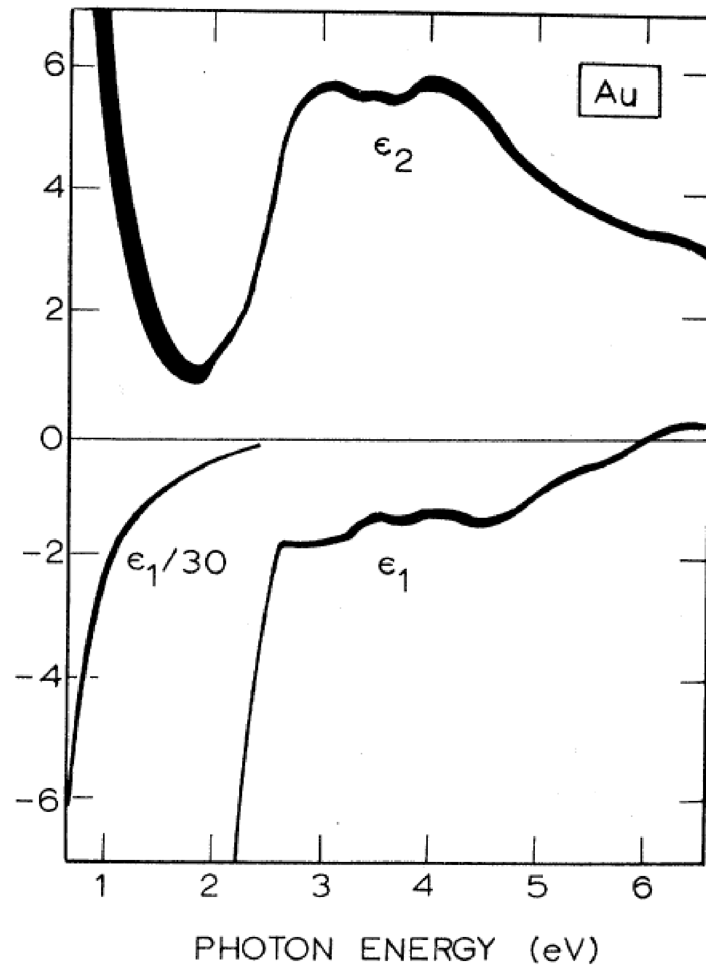

Figure 69 Dielectric constants for gold as a function of photon energy. The width of the curves is representative of the instrumental error.[64]

B. Gold

Figure.69. represent the average of two experiments on films of thickness 343 and 456 A. Again,the agreement between the two experiments was within the experimental-error estimates, demonstrating that in this range there is no thickness dependence of the inferred values of ϵ_1 and ϵ_2. The gold is selected for annealing due to the least affected by oxidation in the noble metal option. A complete set of reflection and transmission measurements was made on the 343 A gold film before annealing. The sample was then annealed in a nitrogen atmosphere at 150 C for 9 h. When the optical measurements were repeated after the annealing, the preannealing results were almost precisely reproduced. Previously it has been noted that the inferred dielectric constants are independent of film thickness only above a certain critical thickness, which for gold is about 250 Å. In order to check this limit, a thinner gold film of I86 Å thickness. The initial optical measurements on this film as evaporated failed to converge to any values of n and k in the visible or ultraviolet. The observed reflection and transmission contours did not intersect in the n-k plane, presumably because the film was not homogeneous and continuous. After annealing this film for 12 h at 150 C, the structure changed enough to give convergent solutions for n and k. The values for ϵ_2 (and n) were well outside of the error estimates for thicker films. Although the annealing apparently improved the uniformity of the 186 A film, inferred values of the dielectric constants are not representative of bulk gold. Thus, bulk values for ϵ_1 and ϵ_2 can only be obtained from films whose thickness is about 300 Å or more.

Table 3 Optical constants for copper, silver, and gold as well as the relative errors in n and k.

	Copper		Silver		Gold		Error	
eV	n	k	n	k	n	k	Δn	Δk
0.64	1.09	13.43	0.24	14.08	0.92	13.78	±0.18	±0.65
0.77	0.76	11.12	0.15	11.85	0.56	11.21	±0.08	±0.30
0.89	0.60	9.439	0.13	10.10	0.43	9.519	±0.06	±0.17
1.02	0.48	8.245	0.09	8.828	0.35	8.145	±0.04	±0.10
1.14	0.36	7.217	0.04	7.795	0.27	7.150	±0.03	±0.07
1.26	0.32	6.421	0.04	6.992	0.22	6.350	±0.02	±0.05
1.39	0.30	5.768	0.04	6.312	0.17	5.663	±0.02	±0.03
1.51	0.26	5.180	0.04	5.727	0.16	5.083	±0.02	±0.025
1.64	0.24	4.665	0.03	5.242	0.14	4.542	±0.02	±0.015
1.76	0.21	4.205	0.04	4.838	0.13	4.103	±0.02	±0.010
1.88	0.22	3.747	0.05	4.483	0.14	3.697	±0.02	±0.007
2.01	0.30	3.205	0.06	4.152	0.21	3.272	±0.02	±0.007
2.13	0.70	2.704	0.05	3.858	0.29	2.863	±0.02	±0.007
2.26	1.02	2.577	0.06	3.586	0.43	2.455	±0.02	±0.007
2.38	1.18	2.608	0.05	3.324	0.62	2.081	±0.02	±0.007
2.50	1.22	2.564	0.05	3.093	1.04	1.833	±0.02	±0.007
2.63	1.25	2.483	0.05	2.869	1.31	1.849	±0.02	±0.007
2.75	1.24	2.397	0.04	2.657	1.38	1.914	±0.02	±0.007
2.88	1.25	2.305	0.04	2.462	1.45	1.948	±0.02	±0.007
3.00	1.28	2.207	0.05	2.275	1.46	1.958	±0.02	±0.007
3.12	1.32	2.116	0.05	2.070	1.47	1.952	±0.02	±0.007
3.25	1.33	2.045	0.05	1.864	1.46	1.933	±0.02	±0.007
3.37	1.36	1.975	0.07	1.657	1.48	1.895	±0.02	±0.007
3.50	1.37	1.916	0.10	1.419	1.50	1.866	±0.02	±0.007
3.62	1.36	1.864	0.14	1.142	1.48	1.871	±0.02	±0.007
3.74	1.34	1.821	0.17	0.829	1.48	1.883	±0.02	±0.007
3.87	1.38	1.783	0.81	0.392	1.54	1.898	±0.02	±0.007
3.99	1.38	1.729	1.13	0.616	1.53	1.893	±0.02	±0.007
4.12	1.40	1.679	1.34	0.964	1.53	1.889	±0.02	±0.007
4.24	1.42	1.633	1.39	1.161	1.49	1.878	±0.02	±0.007
4.36	1.45	1.633	1.41	1.264	1.47	1.869	±0.02	±0.007
4.49	1.46	1.646	1.41	1.331	1.43	1.847	±0.02	±0.007
4.61	1.45	1.668	1.38	1.372	1.38	1.803	±0.02	±0.007
4.74	1.41	1.691	1.35	1.387	1.35	1.749	±0.02	±0.007
4.86	1.41	1.741	1.33	1.393	1.33	1.688	±0.02	±0.007
4.98	1.37	1.783	1.31	1.389	1.33	1.631	±0.02	±0.007
5.11	1.34	1.799	1.30	1.378	1.32	1.577	±0.02	±0.007
5.23	1.28	1.802	1.28	1.367	1.32	1.536	±0.02	±0.007
5.36	1.23	1.792	1.28	1.357	1.30	1.497	±0.02	±0.007
5.48	1.18	1.768	1.26	1.344	1.31	1.460	±0.02	±0.007
5.60	1.13	1.737	1.25	1.342	1.30	1.427	±0.02	±0.007
5.73	1.08	1.699	1.22	1.336	1.30	1.387	±0.02	±0.007
5.85	1.04	1.651	1.20	1.325	1.30	1.350	±0.02	±0.007
5.98	1.01	1.599	1.18	1.312	1.30	1.304	±0.02	±0.007
6.10	0.99	1.550	1.15	1.296	1.33	1.277	±0.02	±0.007
6.22	0.98	1.493	1.14	1.277	1.33	1.251	±0.02	±0.007
6.35	0.97	1.440	1.12	1.255	1.34	1.226	±0.02	±0.007
6.47	0.95	1.388	1.10	1.232	1.32	1.203	±0.02	±0.007
6.60	0.94	1.337	1.07	1.212	1.28	1.188	±0.02	±0.007

Free electron Region

The electronic transitions in a solid are more directly related to the complex dielectric constant $\epsilon=\epsilon 1+\epsilon 2$, instead of the complex index of refraction n=n+ik. These are connected by $\epsilon = n^2$, so that $\epsilon_1 = n^2 - k^2$ and $\epsilon_2 = 2nk$. The dielectric constant is determined by the relaxation time (or dc

conductivity) and the optical mass of the electrons according to the Drude free-electron theory,

$$\epsilon^f(\omega) = 1 - \frac{{\omega_p}^2}{\omega(\omega + i/\tau)}$$

$$\omega_p = \frac{4\pi N e^2}{m_0}$$

Here N is the density of the conduction electrons, $m_0$is their effective optical mass, and τ is the relaxation time. Separating e into its real and imaginary parts, we get

$$\epsilon^f{}_1 = 1 - \frac{{\omega_p}^2\tau^2}{1 + \omega^2\tau^2}$$

$$\epsilon^f{}_2 = 1 - \frac{{\omega_p}^2\tau}{\omega(1 + \omega^2\tau^2)}$$

For metals at near-infrared frequencies, one finds ω» 1/τ Therefore

$$\epsilon_1^f = 1 - \frac{\omega_p^2}{\omega^2} = 1 - \frac{\lambda^2}{\lambda_p^2}$$

And

$$\epsilon_2^f = 1 - \frac{\omega_p^2}{\omega^3\tau} = \frac{\lambda^3}{\lambda_p^2}\tau'$$

Where $\lambda_p^2 = Ne^2/\pi m_0 c^2$ and $\tau' = 2\pi c\tau$. We observe that the optical mass can be determined from the experimental results for ϵ_1^f, and τ can then be found from the results for ϵ_2^f. The free-electron

expression of ϵ is useful only for photon energies below the threshold energy for the onset of interband transitions. Above this threshold energy the form of the ϵ_2 curve, in particular, depends on the specific band structure of the material. Using $\epsilon_1^f=1-\lambda^2/\lambda_p^2$ we can determine m_0 for each of the noble metals from the slope of a plot of $-\epsilon_1$ vs. λ^2 in the infrared. Such plots for copper, silver, and gold are seen in Figure.70.

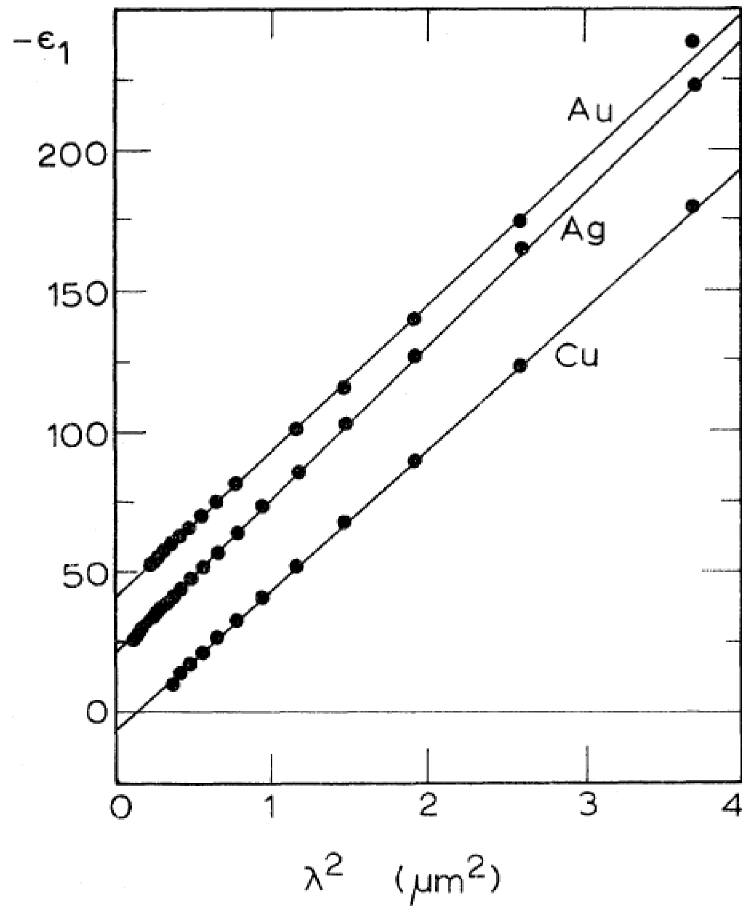

Figure 70 Negative of the real part of the dielectric constants for copper, silver, and gold vs. the square of the wavelength. The zeros in -ϵ_1 for silver and gold are offset by 25 and 50,,respectively.[64]

It is assumed that all the noble metals have one conduction electron per atom, corresponding to a full d band with one free electron. The results for copper, silver, and gold are shown in Table 4.

Table 4 Optical masses and the relaxation times for copper, silver, and gold.

	m_0 (electron masses)	τ (sec)
Copper	1.49 ± 0.06	$(6.9 \pm 0.7) \times 10^{-15}$
Silver	0.96 ± 0.04	$(31 \pm 12) \times 10^{-15}$
Gold	0.99 ± 0.04	$(9.3 \pm 0.9) \times 10^{-15}$

These results are relatively accurate since in the infrared k» n and so $-\epsilon_1 = k^2$. The percentage error in k is small compared with that in n. Next, using the expression $\epsilon_2^f = \lambda^3/\lambda_p^2\tau'$ and plotting ϵ_2/λ vs. λ^2, we can determine τ from the slope of the graph in the infrared. The result for copper, silver, and gold are shown in Figure.71.

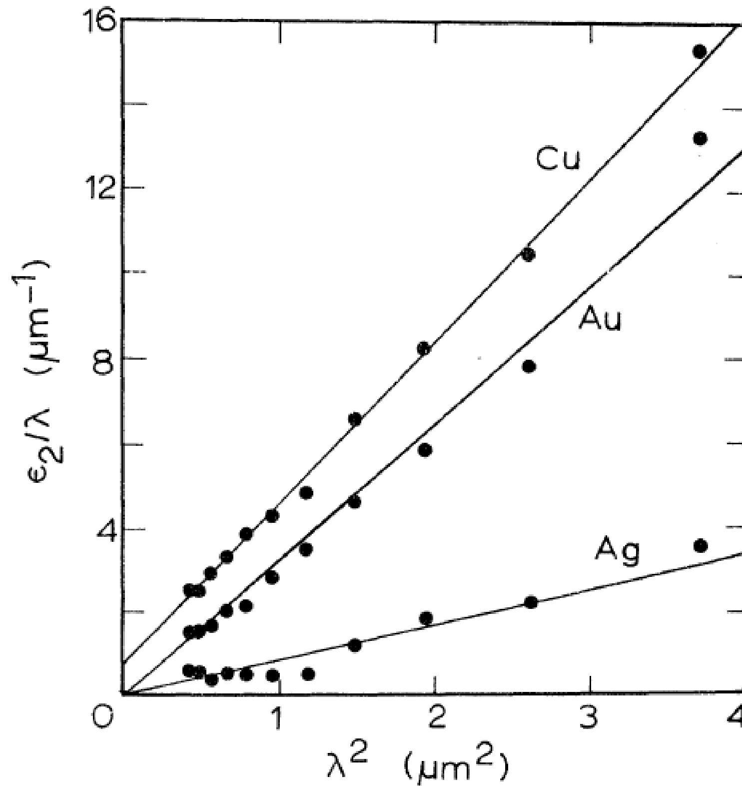

Figure 71 Imaginary part of the dielectric constants for copper, silver, and gold, divided by wavelength vs. the square of the wavelength.[64]

The results for τ are also shown in Table 4. The error in these measurements is moresignificant,since the percentage error in our value of n is large in the infrared. Results for silver are the least accurate, with the uncertainty of about + 40% in n of its value.